Thesis For The Degree Of Doctor Of Philosophy

Efficiency Analysis of Drive-train for an Electrified Vehicle

Ali Rabiei

Division of Electric Power Engineering
Department of Energy and Environment
Chalmers University of Technology
Gothenburg, Sweden 2015

Efficiency Analysis of Drive-train for an Electrified Vehicle
Ali Rabiei
ISBN 978-91-7597-275-6

Doktorsavhandlingar vid Chalmers tekniska hgskola
Ny serie nr 3956
ISSN 0346-718X

Division of Electric Power Engineering
Department of Energy and Environment
SE-412 96 Gothenburg
Sweden
Telephone + 46 (0)31-772 1000

Printed by Chalmers Reproservice,
Göteborg, Sweden 2015.

To my family and friends

Abstract

In this PhD thesis, various solutions to improve the energy efficiency in the electrical drive-train of an electrified vehicle such as modifications of the propulsion inverter or control of the electric machine, are proposed and their benefits are quantified from an energy efficiency point of view. The efficiency analysis is based on modeling of a power electronics inverter, an electric machine and a battery in various drive cycles for an electrified vehicle.

Several solutions are studied for the propulsion inverter. It is shown that by replacing a Silicon pn freewheeling diode in the propulsion inverter with a Silicon Carbide (SiC) diode, an average of up to 1.5 % improvement in the drive cycle efficiency can be expected. Furthermore, by replacing the Silicon IGBTs in the inverter with SiC MOSFETs, the drive cycle efficiency in NEDC can be increased between 2 to 5 percent.

Several solutions to improve the efficiency in a PMSM (Permanent Magnet Synchronous Machine) are investigated. An improved MTPA (Maximum Torque per Ampere) is implemented accounting for the variable nature of the machine parameters due to saturation and temperature. Moreover, the iron losses are accounted for in the derivations of an appropriate maximum torque per ampere angle. It is shown that the low-speed and standstill torque characteristics of a selected PMSM with high current density can be improved by 7 % when using a proposed MTPA algorithm instead of an ordinary MTPA algorithm where the equivalent circuit parameters of the PMSM are updated online outside the optimization algorithm. Furthermore, the efficiency can also be improved up to 5 % at the low-speed and high-torque operating region. However, the overall energy efficiency improvement for a certain drive cycle is not significant and can be up to 0.2 %.

Finally a controllable dc-link voltage for the propulsion inverter is investigated in order to quantify the energy efficiency gain for the inverter and the motor. Their drive cycle energy efficiency improvement is up to one percent when using a SiC based inverter and up to 4 percent for an IGBT based inverter.

Keywords

Energy efficiency, Loss calculation, Vehicle applications, Power electronics, Electric machines, Silicon carbide, Drive cycles, Current vector control

Acknowledgment

The financial support from the Swedish Energy Agency and Swedish Hybrid Vehicle Centre is gratefully appreciated.

I would like to thank my supervisor and examiner Prof. Torbjörn Thiringer. His continuous support and emphasis on educating a researcher is very appreciated. I would also like to thank my co-supervisor Dr. Mikael Alatalo for his great technical contributions and useful discussions.

I would also like to thank all my fellow colleagues in the division of Electric Power Engineering in Chalmers University of Technology who have created a memorable working environment for the past 5 years particularly my office colleagues, Emma Grundtiz, Christian Dubar and Andreas Andersson.

Special thanks to all my Master's thesis students, William Collings, Admas Yeshigeta, Ibrahim Aljanabi, Hamed Raee and Orianne Guinard who helped to improve my skills on several levels.

I would also like to thank my colleagues in NTNU in Trondheim, Subhadra Tiwari, Prof. Ole-Morten Midtgård and Prof. Tore M. Undeland for their interesting discussions and hospitality during my visit to Trondheim. The financial support from the Chalmers Area of Advance (Energy) for this visit is highly appreciated.

Finally, I would like to thank my parents who have always trusted and supported me for wherever I have chosen to be and whatever I have chosen to do.

Ali Rabiei
Göteborg, 2015

List of Publications

[I] Rabiei, A., "Energy Efficiency of an Electric Vehicle Propulsion Inverter Using Various Semiconductor Technologies"
Licentiate Thesis 2013, Chalmers University of Technology, Gothenburg, Sweden

[II] Rabiei, A. ; Thiringer, T. ; Lindberg, J. , "Maximizing the energy efficiency of a PMSM for vehicular applications using an iron loss accounting optimization based on nonlinear programming"
XXth International Conference on Electrical Machines, ICEM 2012, Marseille, France, 2-5 Sept. 2012
Contribution: implementing the developed algorithm, analysis and writing of the article

[III] Tiwari, S ; Rabiei, A. ; Shrestha, P ; Midtgård, O.-M. ; Undeland, T. M. ; Lund, R. Design Considerations and Laboratory Testing of Power Circuits for Parallel Operation of Silicon Carbide MOSFETs *17th Conference on Power Electronics and Applications, EPE-ECCE Europe, Geneva, Switzerland, 8-10 Sept. 2015*
Contribution: jointly designing the test circuit and performing the laboratory measurement as well as writing the article with the main author

[IV] Haghbin, S ; Rabiei, A. ; Thiringer, T. , "High-frequency modelling of a three-phase pulse width modulation inverter towards the dc bus considering line and controller harmonic"
The Journal of Engineering (IET) 2014
Contribution: participating in the design and measurement of the test circuit and jointly writing the article with the main author

[V] Raee, H. ; Rabiei, A. ; Thiringer, T. , "Analytical prediction of switching losses in MOSFETs for variable drain-source voltage and current applications"
IEEE Conference on Industrial Electronics and Applications, ICIEA 2013,

Melbourne, Australia, 1921 June 2013
Contribution: supervising the design of the circuit, the test measurement and writing of the article

[VI] Haghbin, S ; Rabiei, A. ; Grunditz, E. , "Switched Reluctance Motor in Electric or Hybrid Vehicle Applications: A Status Review"
IEEE Conference on Industrial Electronics and Applications, ICIEA 2013, Melbourne, Australia, 1921 June 2013
Contribution: Collaboration around the data collection and writing of the article

[VII] Vindel, D. ; Haghbin, S. ; Rabiei, A. ; Carlson, O. ; Ghorbani, R. , "Field-Oriented Control of a PMSM Drive System Using the dSPACE Controller"
IEEE International Electric Vehicle Conference, IEVC 2012, Greenville, SC, 4-8 March 2012
Contribution: Collaboration in supervising the test measurement and writing of the article

[VIII] Bahmani, M. A. ; Thiringer, T. ; Rabiei, A. ; Abdulahovic, T. , "Comparative Study of a Multi-MW High Power Density DC Transformer with an Optimized High Frequency Magnetics in All-DC Offshore Wind Farm"
Accepted in IEEE Transactions on Power Delivery
Contribution: Collaboration in switching component loss evaluation and writing of the article

[IX] Rabiei, A. ; Thiringer, T. ; Alatalo, M. ; Grunditz, E., "Improved Maximum Torque Per Ampere Algorithm Accounting for Core Saturation, Cross Coupling Effect and Temperature for a PMSM intended for Vehicular Applications,"
Submitted to Electrified Vehicles and Transportation Systems
Contribution: implementing the developed algorithm and writing of the article

List of Acronyms and Nomenclatures

Acronyms

Artemis	Assessment and reliability of transport emission models and inventory systems
BJT	Bipolar Junction Transistor
BNC	Bayonet NeillConcelman
d-q	direct-quadrature
EMF	Electro-Magnetic Force
EMI	Electro-Magnetic Interference
FEA	Finite Element Analysis
GaN	Gallium Nitride
JFET	Junction Gate Field Effect Transistor
MOSFET	Metal Oxide Semiconductor Field Effect Transistor
MTPA	Maximum Torque Per Ampere
NEDC	New European Driving Cycle
NPT	Non-Punch-Through
OCV	Open Circuit Voltage
pn	p-typ n-type
PMSM	Permanent Magnet Synchronous Machines
PWM	Pulse Width Modulation
PT	Punch-Through
RPM	Rounds Per Minute
SiC	Silicon Carbide

Nomenclatures

Symbol	Description
a	Vehicle acceleration
A_f	Frontal area of the vehicle
a_i	Coefficients of the polynomial approximation of L_d
A_N	Linear equality matrix in a non-linear optimization
b_i	Coefficients of the polynomial approximation of L_q
B_m	Amplitude of the AC flux component
B_N	Value of the linear equality matrix in a non-linear optimization
C_d	Air drag coefficient
C_{ds}	Equivalent drain-source capacitance of the MOSFET
C_{gd}	Equivalent gate-drain capacitance of the MOSFET
C_{gs}	Equivalent gate-source capacitance of the MOSFET
c_i	Coefficients of the polynomial approximation of Ψ_m
C_{iss}	Equivalent input capacitance of the MOSFET
c_L	The value of the equality function in the Lagrangian multiplier method
C_N	Linear non-equality matrix in a non-linear optimization
C_{oss}	Equivalent output capacitance of the MOSFET
C_{rss}	Equivalent reverse transfer capacitance of the MOSFET
C_r	Rolling resistance coefficient
D_N	Value of linear non-equality matrix in a non-linear optimization
E_N	Non-linear non-equality matrix in a non-linear optimization
$E_{on,pn\ diode}$	Turn-on switching energy loss when using a pn freewheeling diode
$E_{on,SiC\ diode}$	Turn-on switching energy loss when using a SiC freewheeling diode
E_{on}	Turn-on switching energy loss of a MOSFET or an IGBT
E_{off}	Turn-off switching energy loss of a MOSFET or an IGBT
E_{rr}	Switching loss of a diode
F	Total force on the vehicle
f_B	Frequency of the flux density

f_L	Target function in the Lagrangian multiplier method
F_N	Value of the non-linear non-equality matrix in a non-linear optimization
f_N	Target function of a non-linear optimization
g	Standard acceleration due to gravity
g_L	Equality function in the Lagrangian multiplier method
g_m	MOSFET forward transconductance
i_a	Stator current magnitude vector in d-q system
I_{ce}	Collect-emitter current in an IGBT
$I_{dc-link}$	dc-link current
i_{dq}	Stator current in direct-quadrature axes
i_{ds}	Drain-source current of a MOSFET
$I_{ds,ref}$	The drain-source current where the switching loss is provided
i_{gs}	Gate-source current of a MOSFET
I_m	Peak value for the fundamental of the phase current
I_{max}	Maximum allowed peak stator voltage in the machine
I_o	Load current
I_{rr}	Peak of the reverse recovery or the discharging current of the diode
i_{sd}	Stator current in direct-axis
i_{sq}	Stator current in quadrature-axis
k	Battery constant
K_c	Eddy current loss coefficient
K_e	Extra loss coefficient
K_h	Hysteresis loss coefficient
$k_{I,off}$	Current coefficient of the turn-off switching energy loss
$k_{I,on}$	Current coefficient of the turn-on switching energy loss
$k_{I,rr}$	Current coefficient of the diode switching energy loss
$k_{V,off}$	Voltage coefficient of the turn-off switching energy loss
$k_{V,on}$	Voltage coefficient of the turn-on switching energy loss
$k_{V,rr}$	Voltage coefficient of the diode switching energy loss
L_d	Equivalent inductance in direct-axis
L_{d1}	Parasitic inductance of the drain leg for MOSFET 1
L_{d2}	Parasitic inductance of the drain leg for MOSFET 2
$L_{dc-link}$	Parasitic inductance of the dc-link
L_q	Equivalent inductance in quadrature-axis
L_{s1}	Parasitic inductance of the source leg for MOSFET 1
L_{s2}	Parasitic inductance of the source leg for MOSFET 2

L_{stray}	Lumped stray inductance of the circuit
L_{σ}	Lumped parasitic inductance
m	Vehicle mass
m_a	Modulation index
m_{a3}	Amplitude of the third harmonic
p	Number of pair-poles of the electric machine
P_c	Eddy current losses
$P_{Conduction,Diode}$	Conduction loss for one diode in a PWM operation
$P_{Conduction,Diode\ (3rd\ h)}$	Conduction loss for one diode in a PWM operation with third harmonic injection
$P_{Conduction,Switch}$	Conduction loss for one switch in a PWM operation
$P_{Conduction,Switch\ (3rd\ h)}$	Conduction loss for one switch in a PWM operation with third harmonic injection
P_{cu}	Ohmic Power loss
P_e	Extra losses
P_{fe}	Iron loss
P_{fe0}	Iron loss constant coefficient in the polynomial approximation
P_{fe01}	Iron loss i_{sq} coefficient in the polynomial approximation
P_{fe02}	Iron loss i_{sq}^2 coefficient in the polynomial approximation
P_{fe10}	Iron loss i_{sd} coefficient in the polynomial approximation
P_{fe11}	Iron loss $i_{sd} \cdot i_{sq}$ coefficient in the polynomial approximation
P_{fe20}	Iron loss i_{sd}^2 coefficient in the polynomial approximation
P_h	Hysteresis losses
P_{loss}	Total power losses
Q_{rated}	Rated charge capacity
Q_{rr}	Reverse recovery or switching energy energy of the freewheeling diode
R_{bat}	Battery internal resistance
R_{body}	Equivalent resistor of the body diode in a MOSFET
$R_{ds,on}$	Equivalent resistor of MOSFET's forward characteristics
r_{ew}	Stator end winding resistance
$R_{f,on}$	Equivalent resistor of forward characteristics in a a diode
$R_{g,in}$	Internal gate resistance of the MOSFET
R_g	Gate resistance
$R_{g,in}$	Internal gate resistance

R_{on}	Equivalent resistor of forward characteristics in a MOSFET or IGBT
R_s	Stator winding resistance including the end winding
r_w	Stator winding resistance
T	Temperature
t	Time
T_c	Case temperature of a semiconductor device
t_d	Delay time
T_e	Torque of the electric machine
t_{fi}	Fall-time of the drain-source current during the turn-off
T_j	Junction temperature of a semiconductor device
T_{motor}	Drive cycle demanded torque from the electric motor
T_{ref}	Reference torque value
t_{ri}	Rise-time of the drain-source current during the turn-on
U_{max}	Maximum allowed peak stator current in the machine
u_{sd}	Stator voltage in direct-axis
u_{sq}	Stator voltage in quadrature-axis
V_{bat}	Battery output voltage
$V_{body,0}$	Constant voltage drop of the body diode in MOSFET
V_{ce}	Collect-emitter voltage in an IGBT
V_{dc}	DC-link voltage
$V_{drive\ cycle}$	Velocity reference in km/h of the drive cycle
v_{ds}	Drain-source voltage of a MOSFET
$V_{ds,0}$	Constant voltage drop in forward characteristics of a MOSFET
$V_{ds,ref}$	The drain-source voltage where the switching loss is provided
$V_{f,0}$	Constant voltage drop in forward characteristics of a diode
v_{gd}	Gate-drain voltage of the MOSFET
V_{gg}	Applied to the gate-source
v_{gs}	Gate-source voltage of a MOSFET
$V_{gs,th}$	Gate-source voltage at threshold value
V_{gs,I_o}	Gate-source voltage at load current value
V_{motor}	Drive cycle demanded velocity from the electric motor
V_R	Reverse blocking voltage of a diode
V_{th}	Threshold voltage

X_N	States of the target function of in a non-linear optimization
α	Road inclination angle
β	Angle of stator current magnitude vector toward the d-axis
ΔP_{Loss}	Total power loss difference
$\Delta\eta$	Efficiency difference
η	Efficiency
λ	Lagrange multiplier
Λ	Lagrangian function
ρ	Air density
τ	Time constant
ϕ	Power factor angle
Ψ_d	Flux linkage in direct-axis
Ψ_q	Flux linkage in quadrature-axis
Ψ_m	Permanent magnet flux linkage constant
ω_{el}	Angular electrical rotor frequency

Contents

Chapter 1

Introduction

Electric motors and power electronic devices such as inverters are inherent parts of any electrified vehicle. Through the use of new materials, new topologies and new control strategies, it is possible to improve the efficiency of the electric machine and the power electronic components located in the electric vehicle. Since both the electric motor and power electronic devices have already relatively high efficiency, any efficiency improvement solution will not be very high. The electricity used by these components is stored in the battery and batteries in general are the most expensive electric components in the electric vehicles. This means that the electric energy available in the car is highly valuable and should be used with utmost care.

1.1 Background and previous work

All electric vehicles should have at least one electric propulsion machine. Regarding its control strategies, an efficient control strategy for an electric machine should apart from having high dynamic performance, also minimize the losses in the machine.

In a Permanent Magnet Synchronous Machines (PMSM) with saliency, a certain output torque can be obtained by an infinite combination of current vector references in the direct-quadrature (d-q) system. A good current vector reference should for instance either provide the maximum possible torque for a given magnitude of the current or it should minimize the total losses in the electric machine. The combination of d-q currents which gives the lowest current magnitude for a given torque or the one with the least total loss, is the most favorable one. These objectives can be achieved by using an appropriate control strategy with Maximum Torque Per Ampere (MTPA) as a widely used

algorithm.

A traditional approach is to use the equivalent circuit of the PMSM in the d-q system, based on constant parameters of the machine. The parameters are typically the inductances in d and q-axes (L_d and L_q), as well as the permanent magnet flux linkage constant (Ψ_m). An optimization equation is then used to minimize the torque equation with respect to the magnitude of the current [1].

In [2, 3] a model of a PMSM including the iron loss is used to derive an analytical equation for the calculation of the current vectors. In [4, 5] the same model of a PMSM is used and a weighting factor is proposed to get the current vectors which produce even lower losses. A fully optimized model based current vector control and quantification of how much energy that could be gained by using an energy optimized control instead of a MTPA strategy for various drive cycles, is demonstrated in [6].

However, the equivalent circuit parameters (L_d, L_q and Ψ_m) are not constant and can sometimes vary significantly over a wide operating range of the machine [7]. An improvement of the MTPA-point derivation as suggested in [8,9] is that these parameters are updated online depending on the operating condition of the machine before each MTPA operating point is calculated.

Another group of solutions are based on obtaining the current vector trajectory taking into account the variable nature of these parameters. In these solutions, a Lagrangian multiplier method is used to minimize the torque equation with respect to the current magnitude [10]. Various levels of parameter dependencies are considered in these solutions. In [11], the temperature dependency of Ψ_m is considered in the derivation of the MTPA trajectory and in [12] the temperature dependencies of both Ψ_m and the stator winding resistance (R_s) are considered.

In other proposed solutions, the temperature is ignored and the dependencies of the equivalent circuit parameters (L_d and L_q) are considered either as a function of just the amplitude of the d-q current such as in [13] or d- and q-currents separately as in [14] and [15]. In these papers, the parameters are obtained from the Finite Element Analysis (FEA) of the PMSM with different levels of approximation and simplification. Missing in available literature is an algorithm that accounts for variations in L_d, L_q and Ψ_m as function of operating points, the quantification of the impact that these methods have on the MTPA angle, the resulting torque ability for various current levels as well as the drive cycle energy efficiency consequence.

Thus, it would be of high value to investigate the impact of an improved Maximum Torque Per Ampere (MTPA) algorithm accounting for core saturation and cross coupling d- and q-axes magnetic flux for a PMSM. The

improved MTPA algorithm should takes into account the variable nature of the equivalent circuit d- and q-axes parameters such as L_d, L_q and Ψ_m directly in the optimization algorithm rather than updating these parameters outside the optimization algorithm, which is often proposed in such control strategies.

The previously mentioned algorithms provide the maximum torque per ampere, however, it would be of interest to obtain the current trajectory which provides the maximum torque per power loss unit rather than the ampere unit. In this case, the iron losses must be modelled and be included in the optimization process. The iron losses are generally modelled as a parallel resistance in the equivalent circuit as in [2, 4, 16]. An improved model suggested in [6] includes the speed dependency of the iron losses. However, the assumption of using a resistance representative of the iron losses have some limitations, such as not accounting for the change in harmonic composition of flux density in various operating point of the machine. Therefore, using a FEA iron loss calculation in order to account for this effect would be of interest, particularly, for obtaining the loss minimization control algorithm.

Design consideration of the power electronic components used in a propulsion inverter in an electric vehicle is an area with substantial research interest. In [17] for instance, different topologies, switching frequencies, voltage levels are investigated for the propulsion inverter. New switching devices based on wide band gap materials such as SiC (Silicon Carbide), GaN (Gallium Nitride) have emerged and are suggested for vehicular applications [18,19]. As a result, it is crucial to further investigate the possibility of new technologies and solutions to improve the efficiency and to lower the costs. Since SiC components have different properties compared to Silicon devices, such as higher band gap and thermal conductivity and the possibility for a faster switching, it is important to carefully characterize these devices. In [20] a SiC Schottky, in [21–23] SiC MOSFETs, JFETs and BJTs and in [24] a combinations of both Silicon and SiC devices are characterized.

Out of several advantages of SiC MOSFETs over Silicon IGBTs, one is the absence of the pn junction in the drain-source (main current path) of the device. Thus, paralleling of these devices will decrease the conduction losses more effectively compared to pn junction containing components. In a study conducted in [25], it has been shown that even with a five times higher switching frequency, the SiC solution is able to achieve a maximum efficiency of 99.3 % at 100 kHz. However, a very fast switching may result in EMI (Electro-Magnetic Interferences) issues. Therefore, a trade-off between the switching losses and the EMI generation may be necessary for an optimum design [26]. On the other hand, paralleling of two or more similar switches may cause other

challenges, such as random mismatch of the on-state resistance ($R_{ds,on}$) and the threshold voltage (V_{th}) in two similar switches [27], or a mismatch in the circuit layout leading to two different stray inductances for the paralleled switches. This leads to an unproportionate dynamic behaviour during the switching of parallel MOSFETs [28]. These differences, however, may not hinder the use of paralleling, as in [29, 30] several different SiC switches in parallel are demonstrated, and in [31] a Silicon device in parallel with a SiC MOSFET is proposed in order to maintain the advantages of both SiC and Silicon devices at different operating conditions.

In order to utilize the fast switching behaviour of SiC devices and to minimize the switching losses, a good knowledge of its performance under different operating conditions is necessary. In this thesis some measurement techniques that can affect the measurement results such as load inductor and voltage probes are also explained. Furthermore, switching loss influence due to paralleling of two discrete SiC MOSFETs is quantified and explained for various load currents and dc-link voltages for two different SiC MOSFETs.

In [32], the total losses for two different JFET SiC based inverters are evaluated, however, the results are not put in a vehicular content. In [18] the impact of using SiC devices for propulsion inverters used in hybrid vehicles is investigated using a comprehensive vehicle model from the drive cycle to the battery, however, the switching losses are assumed to be solely dependant on the current. In this thesis a wider loss model is presented which includes the diode reverse recovery and switching dependency on the applied voltage and load current.

With respect to new topology solutions, a DC-DC converter can be used between the battery and the inverter. Depending on the configuration, this converter adds an extra flexibility to the electric system. It will be possible to connect a low voltage battery to a high voltage drive system including an inverter and a motor. It will also make it possible to control the input dc-link of the inverter regardless of the battery voltage to ensure higher efficiency in the inverter, or higher performance of the drive system. Several DC-DC converter topologies are designed and proposed in [33–36]. In this thesis the energy efficiency consequence of using a controllable dc-link voltage, which can be achieved by a DC-DC converter, is studied for the propulsion inverter and the electric machine.

1.2 Purpose of the thesis and contributions of the PhD work

The main objective of the work reported in this thesis is to present methods through which the energy efficiency in an electric drive system of an electrified vehicle can be evaluated and then accordingly enable the quantification of the energy efficiency consequence of a certain change in the electric drive system components. The target is to improve the ideal current angle derivation in the PMSM and prediction of the switching losses in a SiC MOSFET-based propulsion inverters.

The main contributions in this PhD work are listed below.

- Quantified energy efficiency differences of various semiconductor technologies for a propulsion inverter of a vehicle.
- A Maximum Torque Per Ampere method providing an ideal MTPA as well as a comparison with other approaches (Papers IX)
- Established the energy efficiency improvement in an electric drive system by deriving the current reference vectors using a optimized loss minimizing method which accounts for iron losses.
- Established the energy efficiency and performance consequences of using a variable dc-link voltage in a propulsion inverter in an electric drive system.
- Quantified the switching losses of a SiC phase leg and verified these with an appropriate experimental setup (Paper III).
- Established the consequence on the switching losses, when using a double versus a single MOSFET configuration (Paper III).
- Demonstrated the importance of using a well designed load inductor and voltage probe when performing switching loss measurements (Paper III).
- Quantified the usability of an approximate switching loss model (Paper V).
- An analysis of the DC-link current ripple of an inverter over a wide frequency range, modulations and load power factors which are analytically derived and verified in Paper IV.*

- The switching and conduction loss approach used in this thesis is applied to Paper VIII.*

*These contributions are presented in the respective articles only.

1.3 Thesis outline

In Chapter 2, an electric machine is first modelled using Finite Element Analysis (FEA) and then an analytical model suitable for energy efficiency evaluation is extracted. In Chapter 3, the required model for energy loss of a converter using switching devices is presented based on experimental results. In Chapter 4, three new machine control strategies are developed and compared with each other. In Chapter 5, the energy efficiency is evaluated for the entire vehicle model using various inverter solutions.

Chapter 2

Modelling of the Permanent Magnet Synchronous Machine for energy efficiency investigations

In this chapter, the permanent magnet synchronous machine is selected and modelled for energy efficiency analyses. First a representative PMSM for vehicular applications is implemented in a FEA programme (Maxwell). Then an equivalent analytical model of the machine is proposed for the purpose of energy efficiency evaluations in various control algorithms in Chapter 4. The model is also used for the studies dealing with the comparison of various semiconductor technologies in Chapter 5.

2.1 Modelling of the machine in the Finite Element Analysis programme (Maxwell)

A two-dimensional cross section of the selected PMSM simulated in Maxwell is illustrated in Fig. 2.1. The machine is inspired from the Toyota Prius machine, with the exception that the stator yoke thickness has been reduced in order to make it more similar to a propulsion electric motor for a Plug-in hybrid vehicle [37, 38]. The physical dimensions and parameters in the machine are presented in Table 2.1.

For further studies in this thesis, a machine with a higher voltage rating is also required. However, the output power, torque and performance need to

be identical. Therefore, the same machine is rewound in two configurations to achieve the required ratings. In the first configuration (Machine I), the stator has 6 conductors per winding leading to a maximum allowed peak current rating of 565 A with the specified maximum allowed conductor current density and in the second configuration (Machine II) the stator has 12 conductors per winding leading to a maximum allowed peak current of 282.5 A.

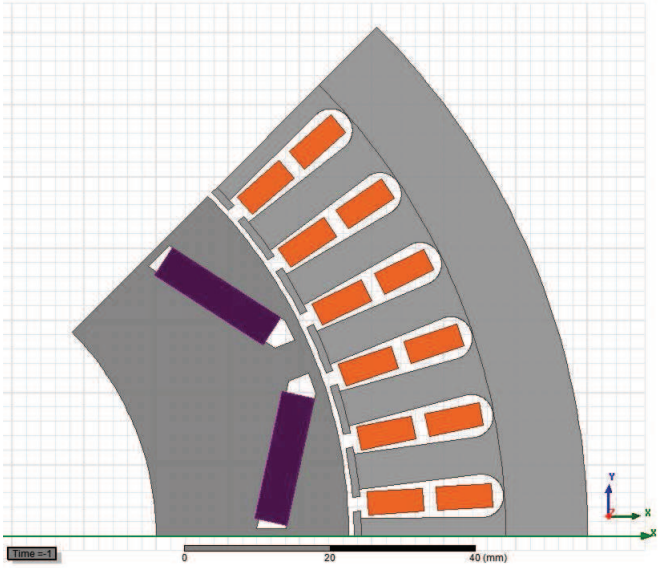

Figure 2.1: A two-dimensional picture of the selected PMSM modeled in Maxwell, where the copper is shown in orange, the iron in gray and the magnets are shown in violet colour.

With an assumption of using a Pulse Width Modulation (PWM) pattern with third harmonic injection, the required dc-link voltage becomes 400 V and 800 V for Machine I and II respectively.

The electric machine which is modelled in a FEA programme (Maxwell), is excited with three-phase currents of various magnitudes, phase shifts and rotational speeds in the range from 1000 up to 12000 RPM. The FEA programme then calculates the flux density in the whole machine as well as the three-phase flux linkages for each of the windings. Furthermore, the three-phase voltages for the windings as well as the torque produced by the machine will be generated by FEA calculations for the given current excitation.

The three phase alternating currents (AC), flux linkages and voltages in the machine can, with the help of the rotor position and mathematic equations be transformed to a rotating reference system called direct-quadrature (d-q)

system where only two direct current (DC) variables are needed to represent the quantities in all three phase windings. The transformation procedure from a three phase system (AC) to a d-q system is thoroughly explained in [39]. Hereafter, only the transformed d-q values and parameters are identified for further analysis. Throughout the work, amplitude invariant transformations will be used, i.e. all currents, flux linkages, voltages in the d-q system has the same value as the peak phase values in the three-phase system.

Table 2.1: The machine parameters with two winding configurations. Machine I with 6 conductors per winding and Machine II with 12 conductors per winding.

Parameter	Value
Active length	150 mm
Stator gap diameter	135 mm
Stator yoke diameter	200 mm
Rotor gap diameter	133.5 mm
Number of poles	8
Magnet material	$NMX\ 37F$
Magnet thickness	4.55 mm
Magnet relative permeability	1.03
Magnet coercivity @20°C	-943·10^3A/m
Magnet coercivity @70°C	-904·10^3A/m
Magnet coercivity @120°C	-864·10^3A/m
Iron material	NO30
Iron mass density	7872 kg/m^3
Hysteresis loss coefficient K_h	443
Eddy current loss coefficient K_c	0.202
Excess loss coefficient K_h	0
Copper bulk conductivity @20°C	59.2·10^6 S/m
Copper mass density	8933 kg/m^3
Slot area	101.13 mm^2
Fill factor	0.45
Current density	26.34 A/mm^2
Number of parallel branches	4
DC-voltage of inverter (Machine I)	400 V
DC-voltage of inverter (Machine II)	800 V
Rotational speed limit	12000 [RPM]
Stator resistance incl. end winding @20°C	0.0143 Ω

The resulting torque obtained from the FEA for various d-q currents, and temperatures are shown in Fig. 2.2. These results are used as map data in this thesis wherever the actual electromagnetic is required for instance investigating a certain control algorithm in Chapter 4.

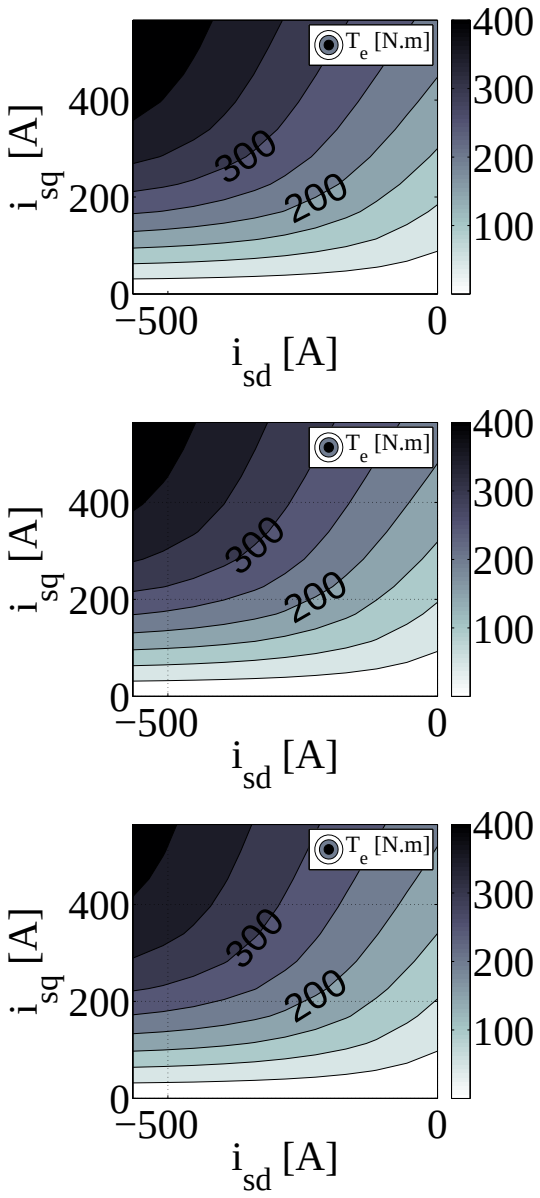

Figure 2.2: The resulting torque of the reference machine I in various i_{dq} for three different temperatures of 20°C , 70°C and 120°C from left to right

As it can be seen in Fig. 2.2 the resulting torque may not change enormously by the temperature except in the high current rating operating region of the machine. It can be seen that a higher maximum torque can be achieved with a lower operation temperature. Therefore, the temperature dependency is considered in this thesis.

2.2 Modelling of the machine parameters in the direct-quadrature system for analytical studies

Traditionally, in an electrically steady state operation of the machine, the relations between the voltage, flux and currents in the d-q system is modelled as [40]

$$u_{sd} = R_s i_{sd} - \omega_{el} \Psi_q \tag{2.1}$$

$$u_{sq} = R_s i_{sq} + \omega_{el} \Psi_d \tag{2.2}$$

where ω_{el} is the angular electrical rotor frequency, u_{sd} and u_{sq} are the stator voltages in the d-q axes, i_{sd} and i_{sq} are the stator currents in the d-q axes and Ψ_d and Ψ_q are the flux linkages in the d-q axes.

However, it has been shown that the flux linkages for a certain operating point depends on the currents in the d-q axes [13]. Moreover, the operating temperature of the machine influence both the flux linkages and the stator resistance [11, 12].

Therefore, a more extended version of the equations above with these variations included is

$$u_{sd}(i_{sd}, i_{sq}, T) = R_s(T) i_{sd} - \omega_{el} \Psi_q(i_{sd}, i_{sq}, T) \tag{2.3}$$

$$u_{sq}(i_{sd}, i_{sq}, T) = R_s(T) i_{sq} + \omega_{el} \Psi_d(i_{sd}, i_{sq}, T) \tag{2.4}$$

Consequently, the resulting torque formed from the flux linkages and currents is

$$T_e = \frac{3}{2} p \Big(\Psi_d(i_{sd}, i_{sq}, T) i_{sq} - \Psi_q(i_{sd}, i_{sq}, T) i_{sd} \Big) \tag{2.5}$$

In order to conveniently determine the performance of the machines, an equivalent circuit model can be created with the help of some machine parameters mainly known as L_d, L_q and Ψ_m in the d-q system. These parameters can

be obtained from $\Psi_d(i_{sd}, i_{sq})$, $\Psi_q(i_{sd}, i_{sq})$ which are obtained from the FEA porgramme (Maxwell). In an electrically steady state operation of the machine, these relations are

$$\Psi_d(i_{sd}, i_{sq}) = L_d(i_{sd}, i_{sq})i_{sd} + \Psi_m(T, i_{sd}, i_{sq}) \tag{2.6}$$

$$\Psi_q(i_{sd}, i_{sq}) = L_q(i_{sd}, i_{sq})i_{sq} \tag{2.7}$$

where L_d and L_q are the equivalent inductances in d-q axes and Ψ_m is the permanent magnet flux linkage constant. Therefore, the voltage and the torque equations(2.3-2.5) can be rewritten as

$$u_{sd} = R_s(T)i_{sd} - \omega_{el}L_q(i_{sd}, i_{sq})i_{sq} \tag{2.8}$$

$$u_{sq} = R_s(T)i_{sq} + \omega_{el}L_d(i_{sd}, i_{sq})i_{sd} + \omega_{el}\Psi_m(T, i_{sq}) \tag{2.9}$$

$$T_e = \frac{3}{2}p\Big(\Psi_m(T, i_{sq})i_{sq} + \big(L_d(i_{sd}, i_{sq}) - L_q(i_{sd}, i_{sq})\big)i_{sd}i_{sq}\Big) \tag{2.10}$$

The q-axis inductance (L_q) can be determined from the knowledge of the flux linkage which is obtained from the FEA and the current in the q-direction. However, in order to obtain L_q, first Ψ_m must be determined by the knowledge of the flux linkage (Ψ_d) at zero current which makes Ψ_m and Ψ_d equal. Then, by subtracting Ψ_m and Ψ_d and dividing the result by i_{sd}, L_d can be determined.

An initial approach for modelling a PMSM using the equivalent circuit model in the d-q system, is to use one set of constant values for the parameters L_d, L_q and Ψ_m. This, however, leads to a circuit based model that can only provide an accurate result at the operating point where L_d, L_q and Ψ_m were initially determined. The more detailed approach is to use look-up tables for all combinations of affected parameters. However, a drawback is that theses tables become very extensive since there are various variables affecting their values. Besides, the look-up tables cannot be directly used in an analytically derived control algorithm. Therefore, a polynomial surface fitting will be used to approximate the coefficients a_i, b_i, c_i, d_i $(i = 0, 1, 2, 3, 4)$.

$$L_d = a_0 + a_1 i_{sd} + a_2 i_{sq} + a_3 i_{sd} i_{sq} + a_4 i_{sq}^2 \tag{2.11}$$

$$L_q = b_0 + b_1 i_{sd} + b_2 i_{sq} + b_3 i_{sd} i_{sq} + b_4 i_{sd}^2 \tag{2.12}$$

$$\Psi_m = c_0 + c_1 i_{sq} + c_2 i_{sq}^2 + c_3 i_{sq}^3 \tag{2.13}$$

The goodness of fitting for each parameter is measured by the ratio of the sum of squares of the regression and the total sum of squares and is maintained

above 97 %. The actual results of the fitting for L_d, L_q and Ψ_m can be seen in Figs. 2.3 to 2.5. The actual coefficient values are provided in Table 2.2. However, some coefficients become very low and are therefore neglected.

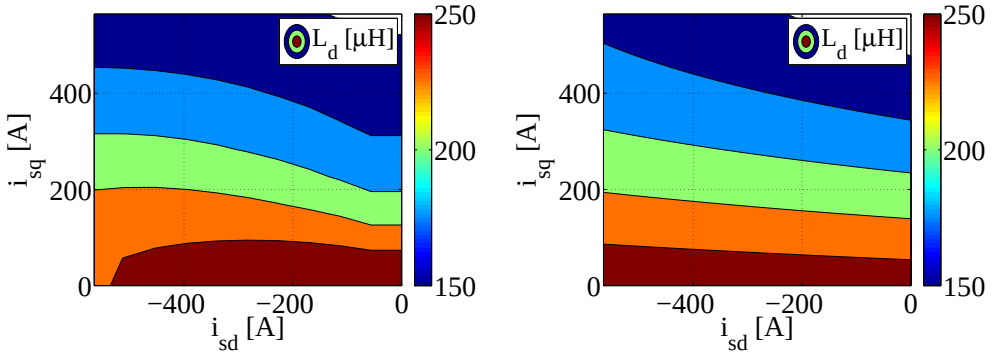

(a) Actual L_d (μH) from Maxwell (b) Approximated L_d (μH)

Figure 2.3: L_d obtained from the FEA and approximated by the polynomial function 2.11 for reference machine I

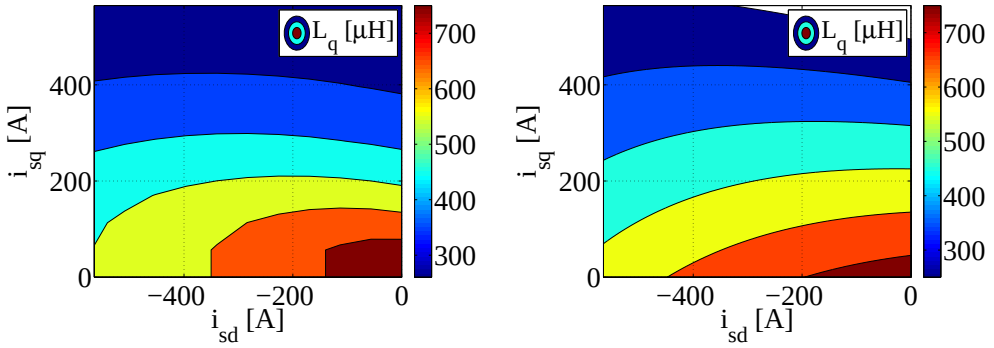

(a) Actual L_q (μH) from Maxwell (b) Approximated L_q (μH)

Figure 2.4: L_q obtained from the FEA and approximated by the polynomial function 2.12 for reference machine I

When the temperature varies, the magnetic flux linkage constant is reduced as seen in Fig. 2.5. This is very obvious when the two figures are compared, where more current is needed in case of higher temperatures to achieve the same torque level. Moreover, it can be noted that since the flux linkage constant goes down with an increasing temperature, more operating points can be achieved with the same available voltage from the viewpoint of the currents. In spite of this, the achievable torque is reduced as the temperature increases.

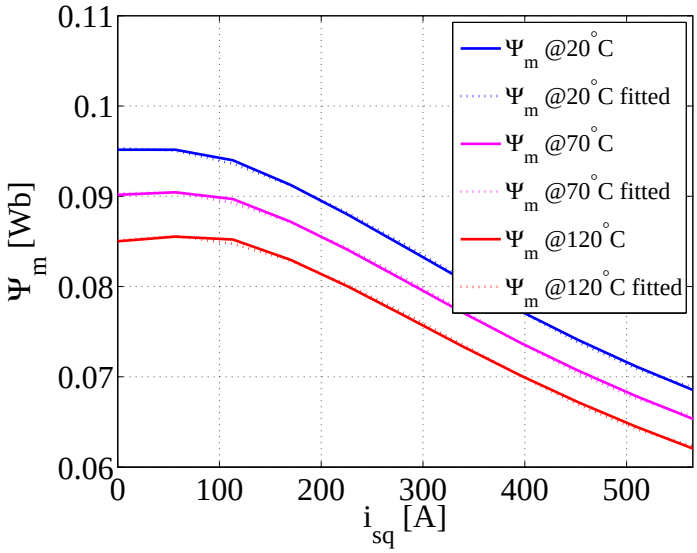

Figure 2.5: Approximated and actual Ψ_m obtained from the FEA for reference machine I

Table 2.2: Machine I parameters coefficient

a_i	i=0	i=1	i=2	i=3	i=4
L_d $[\mu H]$	267	-10·10^{-3}	-326·10^{-3}	-81·10^{-6}	$170 \cdot 10^{-6}$
L_q $[\mu H]$	800	197·10^{-3}	-1111·10^{-3}	-309·10^{-6}	-947·10^{-6}
$\Psi_m(20°C)$ $[Wb]$	0.095	6·10^{-6}	-22·10^{-8}	22·10^{-11}	0
$\Psi_m(70°C)$ $[Wb]$	0.090	14·10^{-6}	-23·10^{-8}	23·10^{-11}	0
$\Psi_m(120°C)$ $[Wb]$	0.085	21·10^{-6}	-24·10^{-8}	24·10^{-11}	0

2.3 Losses of the electric machine

There are copper (ohmic), iron (core), magnet and mechanical losses in a PMSM. The mechanical losses in an electric machine is electrically uncontrollable for a given torque and speed. In a PMSM with interior magnets, the magnet losses are as low as 0.2 % [41] and cannot be avoided. Therefore, both the mechanical and the magnets losses are neglected in this thesis.

The copper losses P_{cu} are proportional to the currents squared and can be calculated by

$$P_{cu} = \frac{3}{2} R_s (i_{sd}^2 + i_{sq}^2). \tag{2.14}$$

where R_s is this thesis includes and the resistance of the stator winding which includes the end windings.

The iron loss in a PMSM is composed of three elements; the hysteresis loss (P_h), the eddy current loss (P_c) and the excess loss (P_e) [42].

$$P_{fe} = P_h + P_c + P_e = K_h f_B (B_m)^2 + K_c (f_B B_m)^2 + K_e (f_B B_m)^{1.5} \tag{2.15}$$

where f_B is the frequency of the flux, B_m is the amplitude of the AC flux component and the coefficients K_h, K_c and K_e are extracted using curve fitting on the measured losses from the datasheet of the used steel. In the datasheet, the iron loss are given for a number of frequencies and magnetic field strength levels.

The iron losses in this work is obtained the FEA programme (Maxwell). The built-in function in Maxwell is utilized to extract the iron loss coefficients. The coefficients are related to the iron material found in Table 2.1.

The resulting iron losses end up as 4-dimensional maps that are function of the d-q currents, speed and temperature. The iron loss for various speeds of 3000, 6000, 9000 and 10000 RPM are depicted in Fig. 2.6 for all possible d-q current combinations. As it can be seen, the iron loss is increasing with both d- and q-currents.

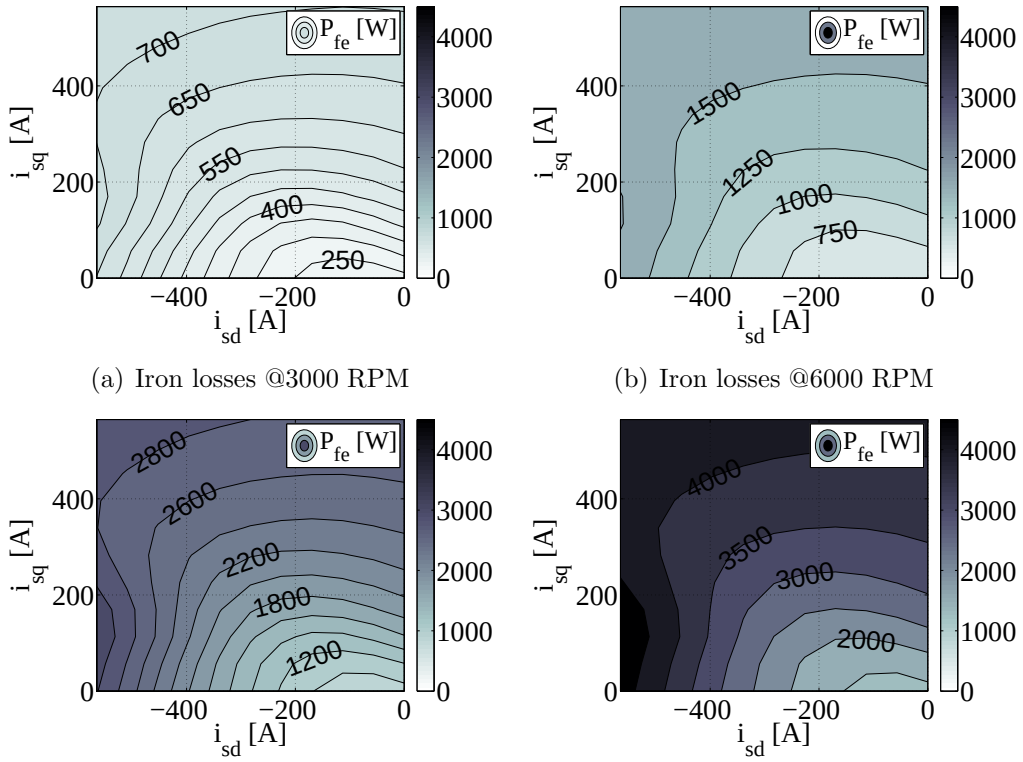

(a) Iron losses @3000 RPM

(b) Iron losses @6000 RPM

(c) Iron losses @9000 RPM

(d) Iron losses @12000 RPM

Figure 2.6: Total iron losses (P_{fe}) for different i_{dq} and speed values

In order to utilize the iron losses for the development of a control algorithm, an equation based modelling of irons losses is required. In literature, the iron loss is typically modelled as a parallel resistor in an equivalent circuit model. This modelling approach has been popular in previous works in order to obtain the equivalent circuits which is required for the extraction of various control algorithms [2, 4, 43, 44].

In Paper II, an improvement to this model is made by making the parallel resistor supply frequency dependant. However, as the FEA result presented in Fig. 2.6 shows, the above mentioned approach is still a rough approximation which does not include the effect of harmonics which lead to an increase of irons losses with an increasing d-axis current. Therefore, in this thesis by using the FEA, a more realistic iron loss determination is achieved, accounting for the impact of the load current in both d-q directions.

In order to utilize the iron losses for the development of the control algorithms in Chapter 4, the iron loss values obtained from the FEA are modelled

as several polynomial expressions in various rotational speeds. Each iron loss map is approximated by a second order polynomial equation as

$$P_{fe} = P_{fe0} + P_{fe10} i_{sd} + P_{fe01} i_{sq} + P_{fe20} i_{sd}^2 + P_{fe11} i_{sd} i_{sq} + P_{fe02} i_{sq}^2 \qquad (2.16)$$

The resulting approximation and the actual iron loss obtained from the Maxwell calculation are shown in Fig. 2.7 for a single speed. The results of the other speeds are provided numerically in Table 2.3.

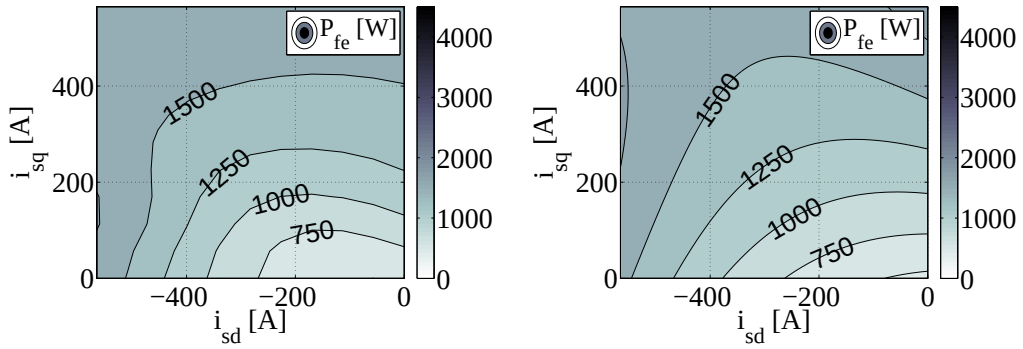

(a) Actual iron loss @6000 RPM from Maxwell

(b) Approximated iron loss @6000 RPM

Figure 2.7: Total iron losses obtained from Maxwell compared with an approximated model using a polynomial function

Table 2.3: Machine parameters coefficient

	P_{fe0}	P_{fe10}	P_{fe01}	P_{fe20}	P_{fe11}	P_{fe02}
$P_{fe\ @3000RPM}$	285	-39·10^{-2}	159·10^{-2}	5·10^{-4}	14·10^{-4}	-10·10^{-4}
$P_{fe\ @6000RPM}$	502	-34·10^{-2}	422·10^{-2}	20·10^{-4}	31·10^{-4}	-29·10^{-4}
$P_{fe\ @9000RPM}$	867	-14·10^{-2}	654·10^{-2}	32·10^{-4}	41·10^{-4}	-45·10^{-4}
$P_{fe\ @12000RPM}$	1164	72·10^{-2}	976·10^{-2}	54·10^{-4}	50·10^{-4}	-71·10^{-4}

2.4 Resulting torque from the Finite Element Analysis for the entire direct-quadrature current map including the current and voltage limit

The resulting torques for all combinations of i_{sd} and i_{sq} obtained from the FEA are given in Fig. 2.8 for a certain operating temperature of 120 °C.

The current limit is shown as a black line where any torque above that will exceed the maximum allowed peak current rating.

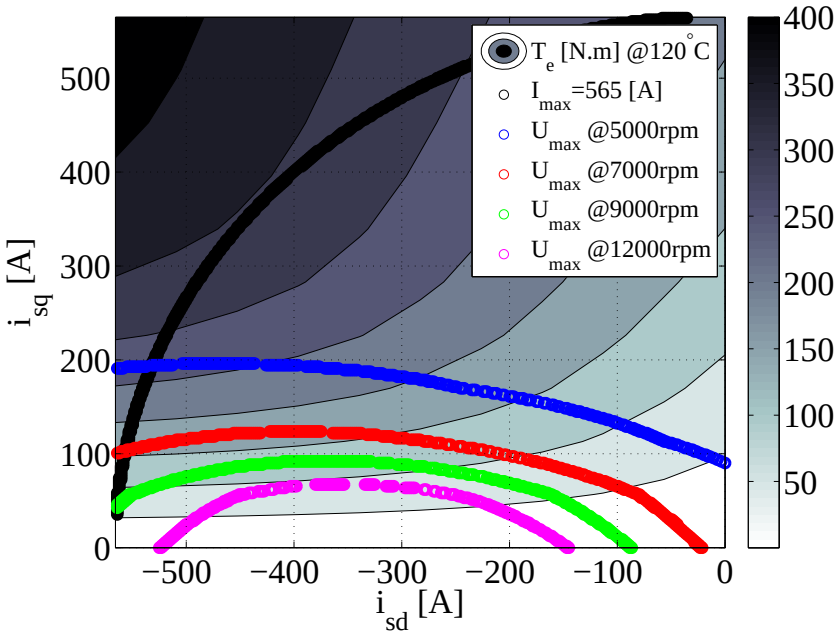

Figure 2.8: The resulting torque contours obtained from Maxwell in different d-q currents along with current and voltage limit lines

The maximum voltage limit is represented with several lines since it varies depending on the rotational speed. Each voltage limit line is shown with a unique colour in Fig. 2.8 and represents the operating points where the d-q currents above that line would lead to a terminal voltage beyond the maximum allowed limit at the given rotational speed. These limits originate from the maximum allowed dc-link voltage of the inverter. For any speed below 4000 RPM, the voltage will always be sufficient for any combination of d-q current.

However, as the speed increases above 4000 RPM, the back EMF (Electro-Magnetic Force) increases leading to an an increased d-q voltage which, affects the current references for the higher rotational speeds (field weakening).

Chapter 3

Modelling of the losses in converters for electric drive system investigations

Power electronics converters have the duty of transforming the electrical power from a certain voltage-current form into another. In a vehicle, a three phase propulsion inverter, converts the electric energy from the dc-link (battery or DC-DC converter) to the load which is the electric motor, or vice versa during the retardation. In Fig. 3.1 a conventional three phase inverter is shown.

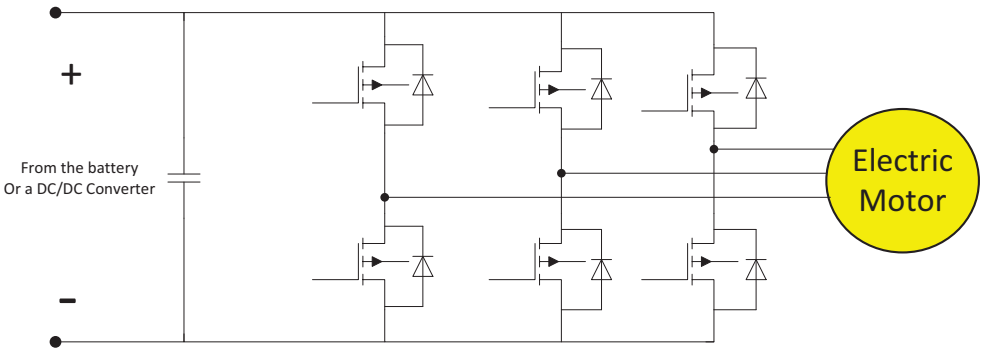

Figure 3.1: A conventional three phase inverter.

The resulting losses in the converters are mainly due to the semiconductors

making up a converter. The power loss in a semiconductor is essentially the product of the voltage over the device and the current through it. During the switching of the device, the value of this power loss can be relatively high (as high as the power rating of the component) while the time period when it occurs is relatively short (often less than a μ second). However, during the rest of the time when the switch is conducting, this power loss is relatively low (as low as a hundredth of the power rating) and the time period is relatively long (about 1/switching frequency minus the dead time). As a result, it is convenient to separate the power losses into two pieces for calculation of the energy losses where the latter is called conduction loss and the former is called switching loss.

Furthermore, the main influencing factors including the load current, dc-link voltage, modulation index and load power factors which are governed by the conditions outside the converter in the electric drive system, need to be related to the converter losses both for the switching losses and the conduction losses.

3.1 Conduction power losses in Pulse Width Modulated inverters

During the conduction, the time length is long enough so that the components can be modeled by their forward static voltage drop characteristics ($v_{ds} = f(i_{ds})$) and the dynamics of the switches can be neglected.

Therefore, the forward characteristic can be linearized and be modeled as a constant voltage drop ($V_{ds,0}$) and a resistor ($R_{ds,on}$) and still maintain a good representation of the forward characterization in the switch. The forward voltage drop can then be expressed as

$$v_{ds} = V_{ds,0} + R_{ds,on} i_{ds} \tag{3.1}$$

The inverter conduction losses of the whole inverter will, however, depend on the power factor (ϕ) as well as the modulation index (m_a) in the PWM modulator. The conduction loss for one switch and one freewheeling diode in an inverter shown in Fig. 3.1 is determined in [45] and can be expressed as

$$P_{Conduction,Switch} = V_{ds,0} I_m \left(\frac{1}{2\pi} + \frac{\pi}{8} m_a \cos\phi\right) + R_{ds,on} I_m^2 \left(\frac{1}{8} + \frac{m_a}{3\pi} \cos\phi\right) \tag{3.2}$$

where I_m is the peak value for the fundamental of the phase current. Similarly, the forward characteristics of the freewheeling diode which relates the diode

current (i_f) and voltage the voltage (v_f), can be modeled as

$$v_f = V_{f0} + R_{f,on} i_f \tag{3.3}$$

where V_{f0} is the constant voltage drop of the diode.

Finally the diode conduction losses can be calculated as

$$P_{Conduction,Diode} = V_{f,0} I_m (\frac{1}{2\pi} - \frac{\pi}{8} m_a \cos\phi) + R_{f,on} I_m^2 (\frac{1}{8} - \frac{m_a}{3\pi} \cos\phi) \tag{3.4}$$

To have a broader view of the conduction loss dependency on the modulation index, current magnitude and the power factor, the conduction losses are calculated for a three phase inverter using the MOSFET (SCT2080KE) [46] as the switching device. As it can be seen in Fig. 3.2, the conduction losses is mainly increasing with the current magnitude. Furthermore, it can be seen that an increasing modulation index intensifies the effect of the power factor.

In order to utilize more of the available dc-link voltage, in practice, third harmonic injection method is typically used [47]. This leads to a slightly different conduction losses [48].

$$\begin{aligned} P_{Conduction,Switch\ (3rd\ h)} =& V_{ds,0} I_m (\frac{1}{2\pi} + \frac{\pi}{8} m_a \cos\phi) + \\ & R_{ds,on} I_m^2 (\frac{1}{8} + \frac{m_a}{3\pi} \cos\phi - \frac{m_{a3}}{15} \cos 3\phi) \end{aligned} \tag{3.5}$$

$$\begin{aligned} P_{Conduction,Diode\ (3rd\ h)} =& V_{f,0} I_m (\frac{1}{2\pi} - \frac{\pi}{8} m_a \cos\phi) + \\ & R_{f,on} I_m^2 (\frac{1}{8} - \frac{m_a}{3\pi} \cos\phi + \frac{m_{a3}}{15} \cos 3\phi) \end{aligned} \tag{3.6}$$

where m_{a3} which is the amplitude of the third harmonic is chosen to 1/6 to maximize the utilization of the dc-link voltage [47, 49].

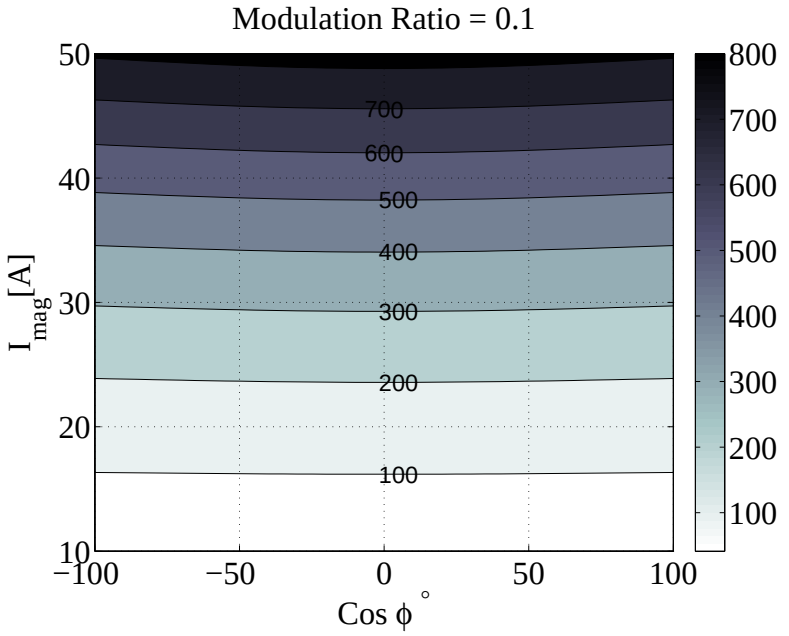

(a) Conduction power loss (W) - Modulation index=0.1

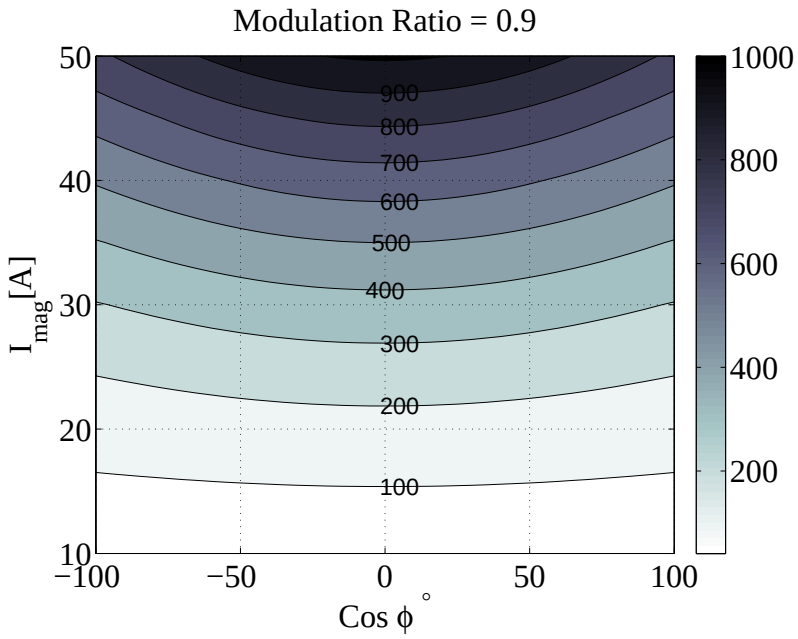

(b) Conduction power loss (W) - Modulation index=0.9

Figure 3.2: Conduction power loss for an inverter using the SiC MOSFET (SCT2080KE) as switching device for various current magnitudes and power factors in degrees

3.2 Switching power losses in Pulse Width Modulated inverters

In order to perform an efficiency analysis for an inverter, a good knowledge of the switching losses is required.

Switching power losses are simply the switching energy losses multiplied by the switching frequency. First, the switching energy losses (E_{on}, E_{off} and E_{rr}) for a MOSFET are obtained for a specific $V_{ds,ref}$ and $I_{ds,ref}$, either through the measurement or it can be approximated from the switching behaviour of the device. A basic approximation of switching losses is shown in Fig. 3.3. The switching device is used in a half bridge with highly inductive load where currents and voltage rise and fall linearly between zero and their rated values.

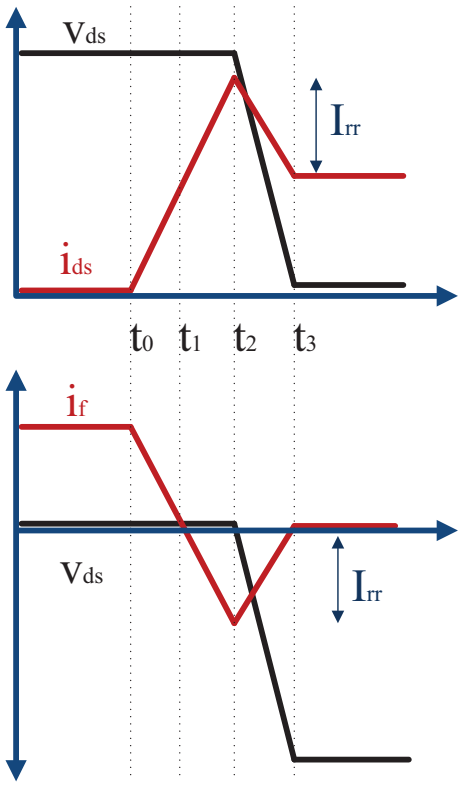

Figure 3.3: Approximate switching curves for the switching (top) device the freewheeling diode (bottom)

During the turn-off, it can be assumed that the switching current and the voltage change linearly from zero to their maximum values. However, the turn-on is affected by the reverse recovery current of the freewheeling diode. Therefore, as it can be seen in Fig. 3.3, the switching process during the turn-on is divided into three parts and the turn-on switching loss energy can be calculated in three steps for the three time intervals.

$$\begin{aligned} E_{on} &= \int_{t0}^{t1} v_{ds} i_{ds} = \int_{t1}^{t2} v_{ds} i_{ds} = \int_{t2}^{t3} v_{ds} i_{ds} \\ &= \frac{V_{ds} I_{ds} (t_1 - t_0)}{2} \\ &+ V_{ds} (I_{ds} + \frac{I_{rr}}{2})(t_2 - t_1) \\ &+ V_{ds} (\frac{I_{ds}}{2} + \frac{I_{rr}}{3})(t_3 - t_2) \end{aligned} \tag{3.7}$$

Switching loss occurs when there is a non-zero voltage and current over the component. As a result the reverse recovery energy loss in the diodes only occurs during the t_2 to t_3. The integration over this time interval leads to

$$\begin{aligned} E_{rr} &= \int_{t2}^{t3} v_f i_f \\ &= \frac{V_f I_f t_{rr}}{6}. \end{aligned} \tag{3.8}$$

The turn-off loss is similarly calculated by

$$E_{off} = \frac{V_{ds} I_{ds} t_{off}}{2}. \tag{3.9}$$

Now that the switching losses are available the reference values $(I_{ds,ref}, V_{ds,ref})$, the switching losses can be adjusted for other voltages v_{ds} and current i_{ds} using

$$E_{on} = E_{on,ref} \cdot (\frac{v_{ds}}{V_{ds,ref}})^{k_{V,on}} \cdot (\frac{i_{ds}}{I_{ds,ref}})^{k_{I,on}} \tag{3.10}$$

$$E_{rr} = E_{rr,ref} \cdot (\frac{v_{ds}}{V_{ds,ref}})^{k_{v,rr}} \cdot (\frac{i_{ds}}{I_{ds,ref}})^{k_{I,rr}} \tag{3.11}$$

$$E_{off} = E_{off,ref} \cdot (\frac{v_{ds}}{V_{ds,ref}})^{k_{v,off}} \cdot (\frac{i_{ds}}{I_{ds,ref}})^{k_{I,off}} \tag{3.12}$$

where $k_{V,on}$, $k_{V,off}$, $k_{V,rr}$, $k_{I,on}$, $k_{I,off}$ and $k_{I,rr}$ are coefficients that relate the losses calculated or measured in the reference current and voltage to other currents and voltages.

3.3 Simplified model of the switching transients in MOSFETs

In order to investigate the switching losses, understanding of the switching behaviour is necessary. In this section, the theory of the parameters that influence the switching process are provided. These parameters and their impact on the switching process are not necessary visible in simulations such as Spice/LTSpice.

The transient model of a MOSFET which is described in [50], is shown in Fig. 3.4. The model is a substantial simplification of a more complex object. Furthermore, L_{Stary} which is the lumped parasitic and stray inductances of the circuit is also included in the model. C_{ds}, C_{gs} and C_{gd} are internal capacitances of the MOSFET. The values of these capacitances can vary depending on the applied voltage and can be expressed in terms of the parameters C_{iss}, C_{oss}, and C_{rss} which are the parameters provided in datasheets by the manufacturer.

$$\begin{aligned} C_{gd} &= C_{rss} \\ C_{gs} &= C_{iss} - C_{rss} \\ C_{ds} &= C_{oss} - C_{rss} \end{aligned} \tag{3.13}$$

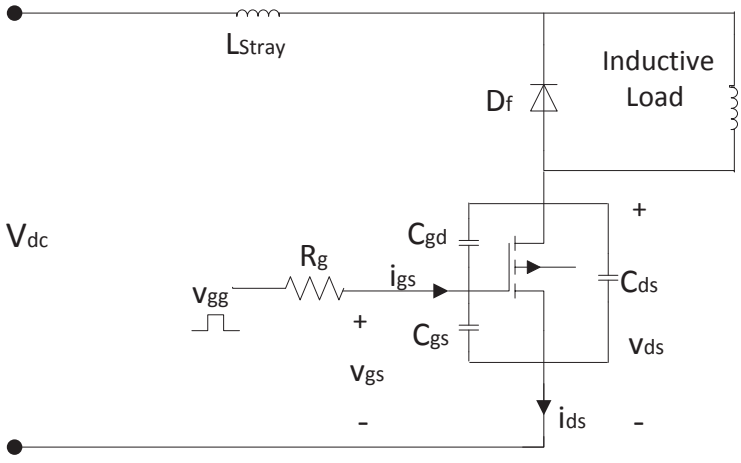

Figure 3.4: MOSFET transient modeling circuit

3.3.1 Turn-on process

The turn-on process waveforms based on the model illustrated in Fig. 3.4 is shown in Fig. 3.5.

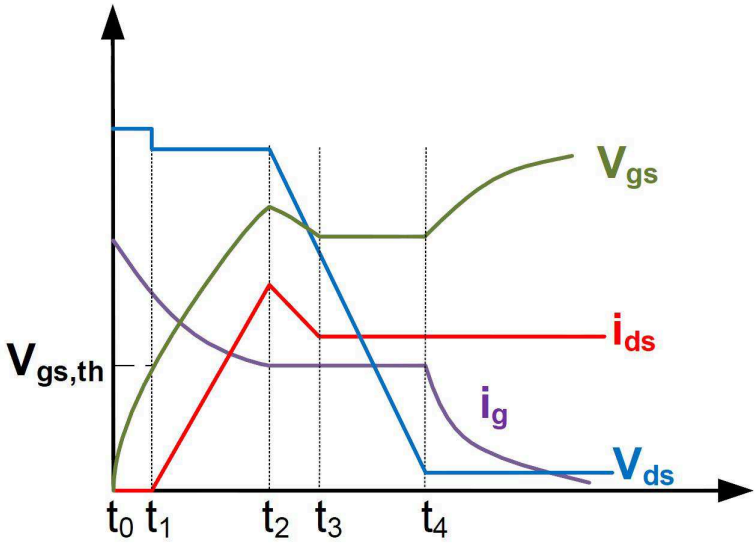

Figure 3.5: MOSFET turn-on waveforms

At the beginning, the device is off and the load current is passing through the freewheeling diode. The initial conditions are: $v_{gs} = 0\ V$, $v_{ds} = V_{dc}$ and $i_{ds} = i_{gs} = 0\ A$. At $t = t_0$, V_{gg} is applied to the gate-source and the internal (and externally added) capacitors across the gate-source and gate-drain, start to be charged through the gate resistor R_g. The gate-source voltage increases exponentially with the time constant $\tau = R_g \cdot (C_{gs} + C_{gd})$. The drain current remains zero until v_{gs} reaches the threshold voltage ($V_{gs,th}$). The threshold voltage is the minimum gate-source voltage required before the drain-source current starts to increase during the turn-on. The equations describing the current and voltage relations in the time interval $t_0 - t_1$ are

$$\begin{aligned} i_{gs} &= \frac{V_{gg} - v_{gs}}{R_g} \\ &= C_{gs}\frac{dv_{gs}}{dt} - C_{gd}\frac{d(V_{gg} - v_{gs})}{dt} \end{aligned} \tag{3.14}$$

$$\rightarrow \frac{V_{gg} - v_{gs}}{R_g} = C_{gs}\frac{dv_{gs}}{dt} - C_{gd}\frac{d(V_{gg} - v_{gs})}{dt} \tag{3.15}$$

$$\rightarrow v_{gs} = V_{gg}(1 - e^{-(t-t_0)/\tau}) \tag{3.16}$$

The delay time, which is the time that it takes for the gate-source voltage to reach the threshold voltage ($v_{gs}(t_2) = V_{gs,th}$), is

$$t_1 - t_0 = t_d = -\tau ln(1 - \frac{V_{gs,th}}{V_{gg}}) \tag{3.17}$$

When v_{gs} reaches the threshold voltage, the drain current starts to increase linearly causing the drain-source voltage to drop. At the same time the diode becomes reverse biased and turns off. The equations during the time period t_1-t_2 are

$$v_{ds} = V_{dc} - L_{Stray}\frac{di_{ds}}{dt} \tag{3.18}$$

$$i_{ds} = g_m(v_{gs} - V_{th}) \tag{3.19}$$

where g_m is the MOSFET forward transconductance and is a nonlinear factor which can be extracted from the datasheet of the switch. The drain current increases until it reaches the load current I_o. However, in case of having a diode reverse recovery current (I_{rr}), it increases up to $I_o + I_{rr}$ instead. The rise time of the drain current can be calculated as [51],

$$t_2 - t_1 = t_{ri} = \tau ln(\frac{g_m(V_{gg} - V_{gs,th})}{g_m(V_{gg} - V_{gs,th}) - (I_0 + I_{rr})}) \tag{3.20}$$

During the time interval t_2 to t_3, the reverse recovery takes place while v_{gs} starts from $v_{gs} = V_{gs,th} + \frac{I_o+I_{rr}}{g_m}$ and finishes at $v_{gs} = V_{gs,th} + \frac{I_o}{g_m}$ when reserve recovery ends.

At t_3, the gate voltage reaches the plateau level, the gate voltage and current remain constant and all the gate current passes through the gate-drain capacitor. Therefore the gate current is

$$i_{gs} = -C_{gd}\frac{dv_{ds}}{dt} \tag{3.21}$$

and the drain-source voltage is

$$v_{ds} = -\frac{V_{gg} - V_{gs,th}}{R_g C_{gd}}(t - t_2) + V_{dc} \tag{3.22}$$

As soon as the drain-source voltage reaches the input voltage, v_{gs} starts to increase toward V_{gg} while i_g decreases until it reaches zero.

Finally at t_4, the MOSFET enters the steady state mode and operates according to its forward characteristic.

$$v_{ds} = R_{ds,on} I_o \tag{3.23}$$

where $R_{ds,on}$ is the resistive behavior of the MOSFET according to its forward characteristic and I_o is the load current passing from the drain to the source.

3.3.2 Turn-off process

The principle of the turn-off is similar to the turn-on. The turn-off waveforms are shown in Fig. 3.6. The initial conditions for the turn-off period are $v_{ds} = R_{ds,on} I_o$, $v_{gs} = V_{gg}$, $i_{gs} = 0$ and $i_{ds} = I_o$.

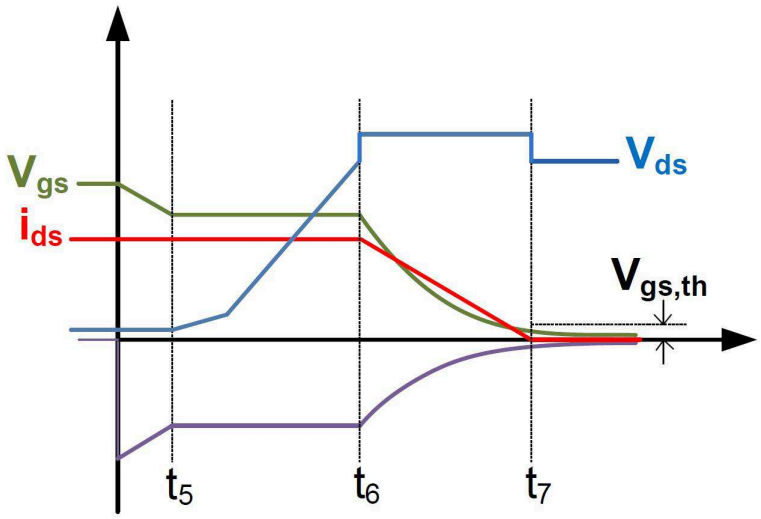

Figure 3.6: MOSFET turn-off waveforms

The turn-off process starts when the applied gate voltage starts falling, making the gate-source and gate-drain capacitors to discharge through C_{gs}, C_{gd} and R_g. The gate current and voltage can be obtained by

$$\begin{aligned} i_{gs} &= -\frac{V_{gg}}{R_g} \\ &= (C_{gs} + C_{gd}) \frac{dv_{gs}}{dt} \end{aligned} \tag{3.24}$$

$$v_{gs} = V_{gg} e^{-(t-t_0)/\tau} \tag{3.25}$$

The gate-source voltage continues to decrease until it reaches the plateau level at $t = t_5$, while the drain current remains at the same level as the load current. The gate-source voltage at $i_{ds} = I_o$ is

$$v_{gs} = \frac{I_o}{g_m} + V_{gs,th} \tag{3.26}$$

From (3.25) and (3.26), the time that it takes for the gate-source voltage to reach a constant value can be obtained by

$$v_{gs} = \tau \frac{V_{gg}}{\frac{I_o}{g_m} + V_{gs,th}} \tag{3.27}$$

In the time interval t_5-t_6 , the gate-source voltage is constant. Therefore, the entire gate current is discharged through C_{gd}. The gate current can expressed as,

$$\begin{aligned} i_{gs} &= C_{gd}\frac{dv_{gd}}{dt} \\ &= C_{gd}\frac{d(v_{gs} - v_{ds})}{dt} \\ &= -C_{gd}\frac{dv_{ds}}{dt} \end{aligned} \tag{3.28}$$

The gate current can also be expressed as

$$i_{gs} = \frac{V_{gs,th}}{R_g} = \frac{1}{R_g}(\frac{I_o}{g_m} + V_{gs,th}) \tag{3.29}$$

Therefore, the drain-source voltage will be achieved by combining (3.28) and (3.29)

$$v_{ds} = R_{ds}I_o + \frac{1}{R_g C_{gd}}(\frac{I_o}{g_m} + V_{gs,th})(t - t_1) \tag{3.30}$$

At the time t_6 the drain-source voltage reaches the dc-link voltage (V_{dc}), forcing the free-wheeling diode to be turned on. Hence the drain-source current starts falling and it is described according to the MOSFETs transconductance as

$$i_{ds} = g_m(v_{gs} - V_{gs,th}) \tag{3.31}$$

where v_{gs} is obtained from the following equation,

$$v_{gs} = (\frac{I_o}{g_m} + V_{gs,th})e^{-(t-t_2)/\tau} \tag{3.32}$$

The current fall time (t_{fi}) is calculated by having the time constant and the gate-source voltage at the load current ($V_{gs,Io}$).

$$t_{fi} = -R_g C_{iss} ln \frac{V_{gs,th}}{V_{gs,Io}} \tag{3.33}$$

While the current is falling, the lumped parasitic stray inductance in the circuit (L_{Stray}) causes an overshoot in v_{ds} as

$$v_{ds} = V_{dc} + L_\sigma \frac{di_{ds}}{dt} \tag{3.34}$$

where the rate of changes of the current($\frac{di_{ds}}{dt}$) in the device is achieved by dividing the MOSFET load current over the current fall time.

$$\frac{di_{ds}}{dt} = \frac{I_o}{t_{fi}} \tag{3.35}$$

However, it should be noted that the t_{fi} may not be necessarily decided by the MOSFET itself if the parasitic inductances in the drain-source loop are big enough to force a slower rate of current during the turn-on or turn-on.

Finally during the time interval t_6-t_7 the gate-source voltage reaches the threshold voltage ($v_{gs}(t_7) = V_{gs,th}$). The gate-source voltage goes to zero and the MOSFET is fully turned off.

3.4 Switching losses in paralleled Silicon Carbide MOSFETs

The theory of switching transients based on the theory and during the turn-on or turn-off is compared with an experiment in Section 3.3. In this section an experimental evaluation of switching losses is carried out to determine the actual switching loss of SiC MOSFET devices in various current and voltage levels.

In MOSFETs and SiC MOSFETs in particular, a discrete component has usually low current capability for vehicle applications. Therefore, either several discrete components are paralleled directly in the circuit board or a modular unit consisting of several components in parallel is used. Therefore, a better understanding of the consequence of parallel operation of these components and its impact on losses, is necessary. The power loss implication of paralleling is also evaluated.

Two separate SiC MOSFETs [46, 52] and a SiC freewheeling diode [53] are chosen for this experiment. The general characteristics of the MOSFETs are found in Table 3.1. In the circuit diagram shown in Fig. 3.7 , the circuit used for this experiment is illustrated.

Table 3.1: SiC MOSFETs used in the measurement

MOSFETS	$R_{ds,on}$ ($m\Omega$) @25 °C	$R_{ds,on}$ ($m\Omega$) @135 °C	V_{th} (V)	$R_{g,in}$ (Ω)	C_{iss} (pF)	C_{oss} (pF)	C_{rss} (pF)
CMF20120 (Cree)	80	95	2.45	5	1915	170	15
SCT2080KE (Rohm)	80	125	3	6.3	2080	120	20

The actual setup used to perform this experiment is show in Figs. 3.8 and the circuit layout is shown in Fig. 3.9.

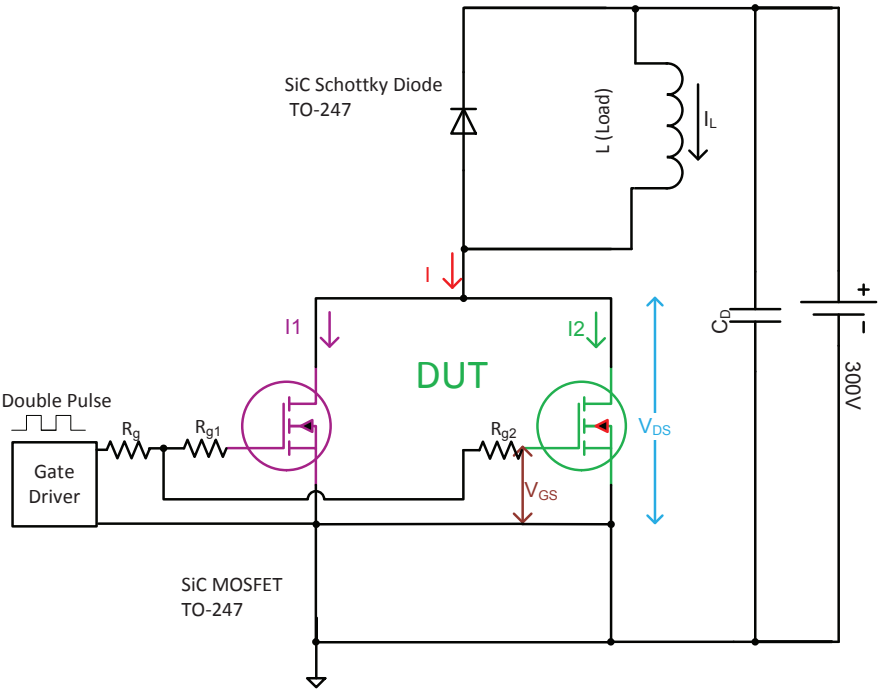

Figure 3.7: Circuit diagram

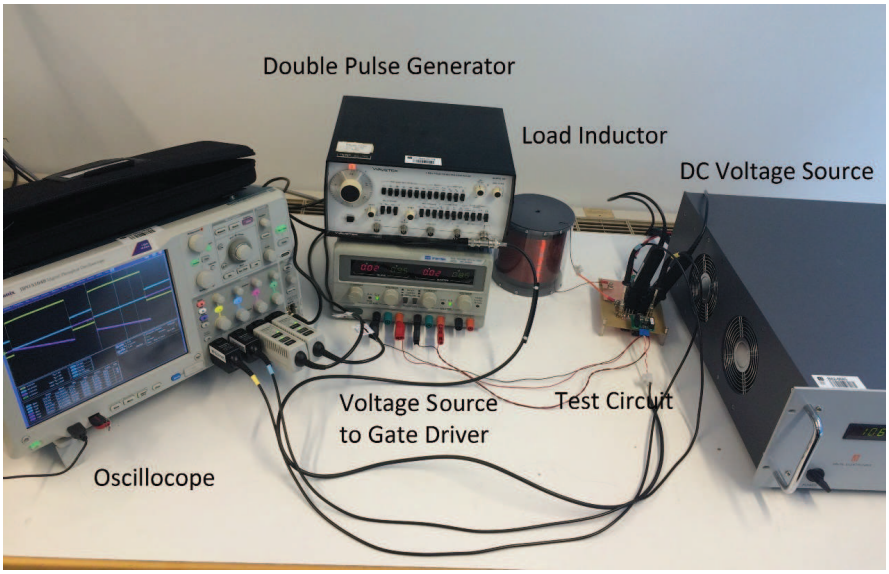

Figure 3.8: The laboratory setup

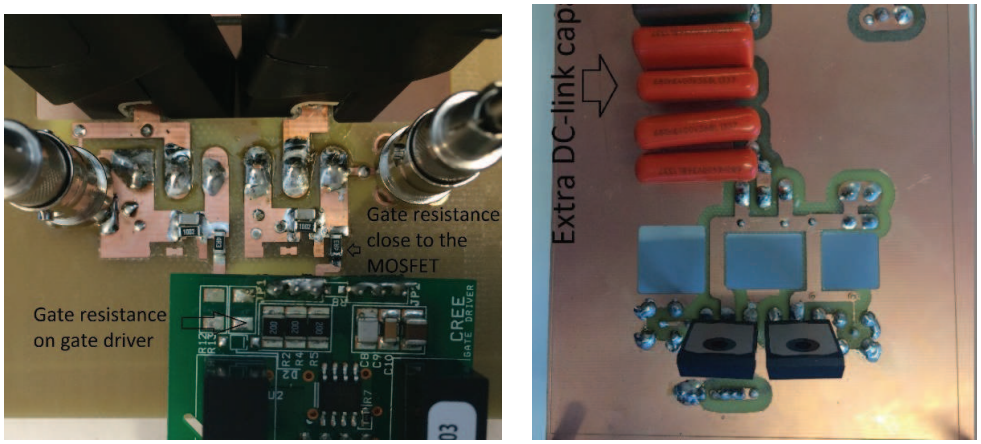

(a) Circuit layout(Top) (b) Circuit layout(Bottom)

Figure 3.9: Circuit layout for the evaluation of paralleled SiC MOSFET losses

3.4.1 Measurement considerations

The measurements of the switching behaviour should be performed with high accuracy since the result is highly dependent of the measurement setup and equipment. It is shown in this section that the choice of the inductor load can

affect the switching current during the turn-on and the choice of the voltage probe ground can change the measured overvoltage during the turn-off.

To measure the very fast switching voltage transients of SiC MOSFETs, a high bandwidth (1 GHz) passive voltage probe in combination with a high bandwidth oscilloscope is used. The drain source voltage of the SiC MOSFET during the turn-off is measured by two identical voltage probes, one with the standard ground wire (Case 1) and one with a BNC to tip adapter where the ground is directly connected to the probe through the BNC connection.

As can be seen in Fig. 3.10, the use of a standard ground cable for measuring the voltage (Case 1) mistakenly records a higher overshoot of 50 V during the switching than exists in reality. As a result, a BNC to tip adapter is used very close to the measuring point (Case 2) to minimize the measurement error.

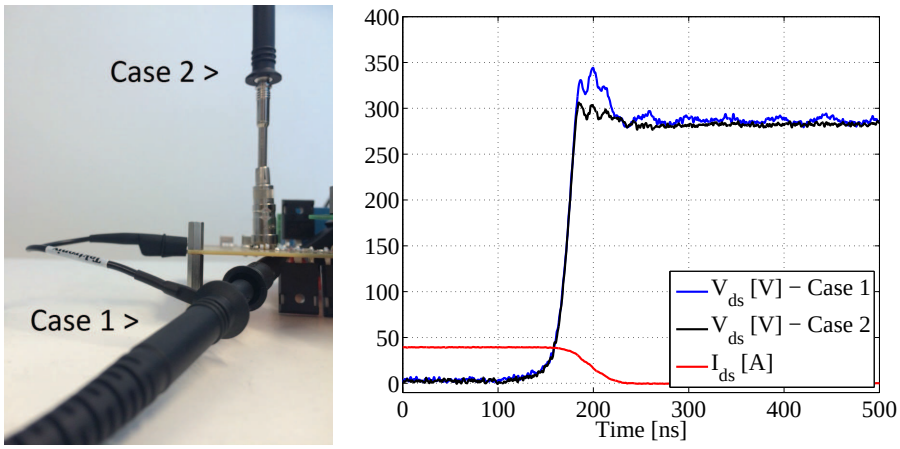

(a) Voltage probe placement

(b) Measured V_{ds}

Figure 3.10: Voltage measurement influence on the switching

In a double pulse switching test, the load inductor should act as a constant current source that keeps the current flowing during the turn-on and turn-off of the switch. Three different inductors, which are shown in Fig. 3.11, are examined for this experiment. Inductor 1 has an iron core whereas inductor 2 and 3 have an air core configuration. The influence of the different load inductors on the switching transients is shown in Fig. 3.12.

(a) Inductor 1 (Iron Core) (b) Inductor 2 (Air Core) (c) Inductor 3 (Air Core)

Figure 3.11: Selected Load Inductors

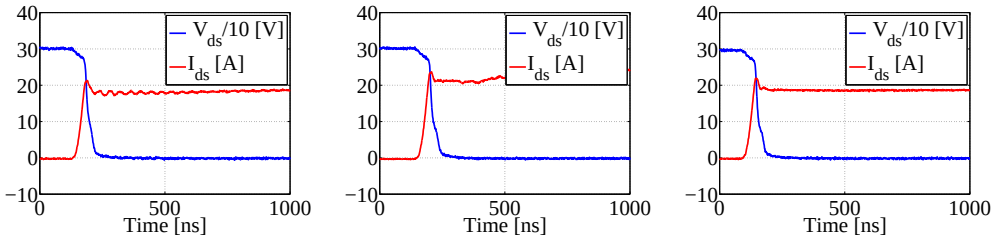

(a) Inductor 1 (b) Inductor 2 (c) Inductor 3

Figure 3.12: Switching behaviour obtained from the experimental results using the selected load inductors

An inductor has a parasitic capacitance at higher frequencies, which can be due to inner winding parasitic capacitance and/or core capacitance. The parasitic capacitance can cause oscillations during the switching. As can be seen in Fig. 3.12 (b), these oscillations are more significant in the iron core inductor, which also has several layers of winding. It is also observed that inductor 2 results in some disturbances, whereas inductor 3 gives the most smooth switching behaviour. Therefore, inductor 3, which is a single layer air core inductor, is chosen as the load in all the measurements during the tests. It can be seen that an unsuitable inductor can also lead to an oscillation of up to 10 % of load current during the turn-on.

3.4.2 Switching transients of paralleled Silicon Carbide MOSFETs

The switching transient obtained from the lab experiment is compared with the LTSpice simulations for a similar current/voltage rating in Fig. 3.14. These parasitics are included in the simulation model which is shown in Fig. 3.13.

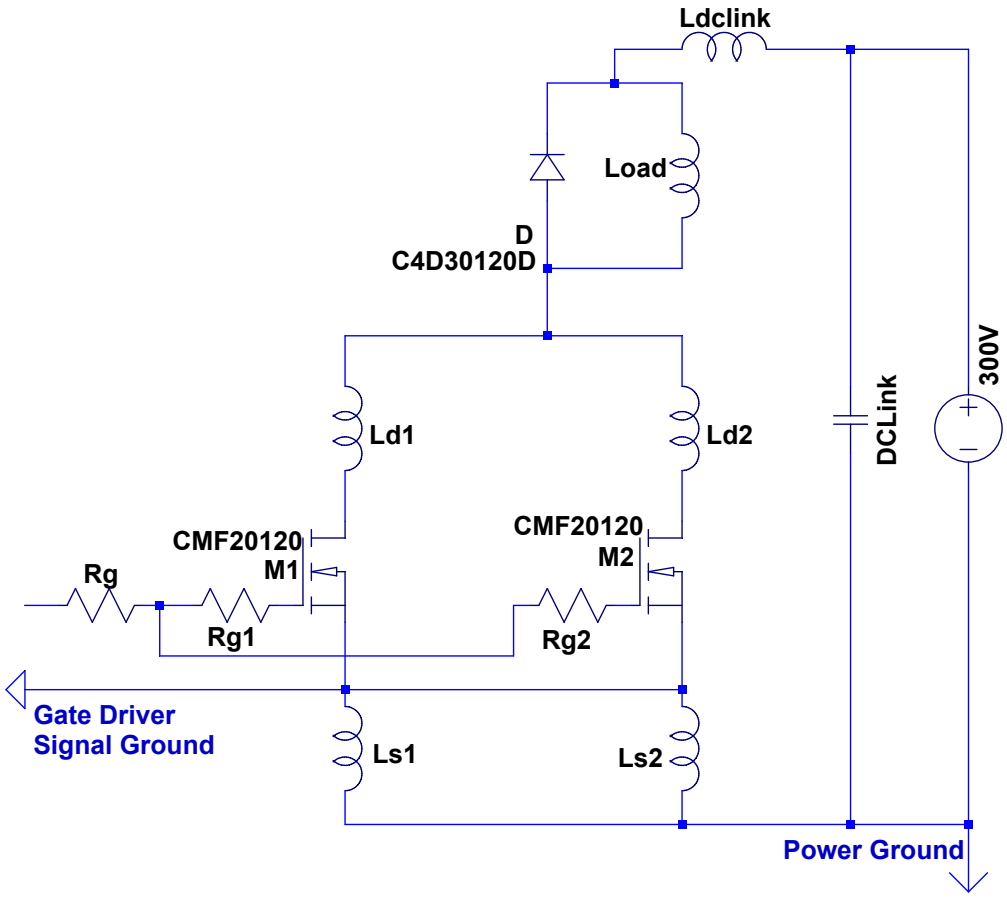

Figure 3.13: Equivalent circuit model in LTSpice used for the simulation of the switching behaviour

Fig. 3.14 (c) and Fig. 3.14 (d) show the turn-on and turn-off switching transients from laboratory test at a dc-link voltage of 300 V and a drain-source current of 10 A in each SiC MOSFET (CMF20120) at 25 °C.

The current and voltage probes are fully compensated prior to the measurement, and the phase delays between the probes are compensated. A current rise time of 21 ns and a voltage rise time of 18 ns are measured. Correspondingly,

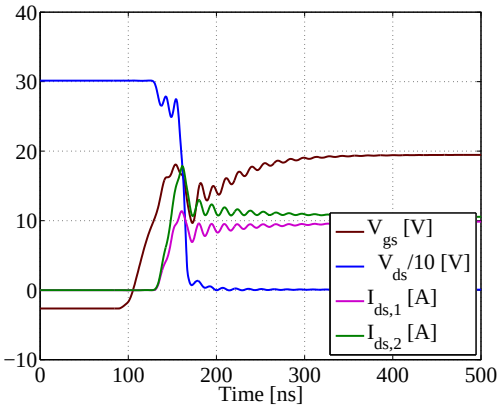

(a) Turn-on transient from the simulation

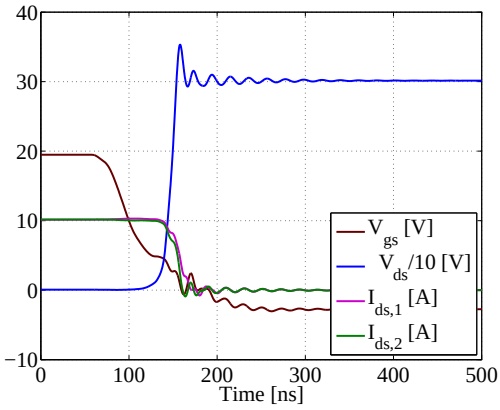

(b) Turn-off transient from the simulation

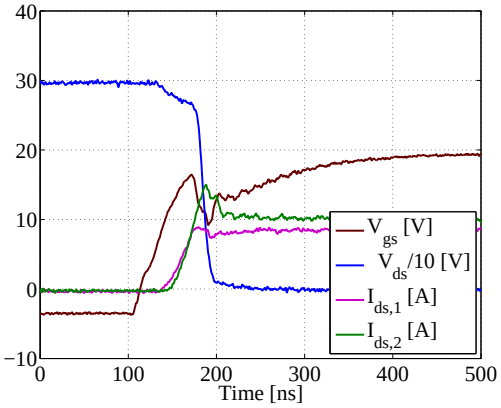

(c) Turn-on transient from the lab experiment

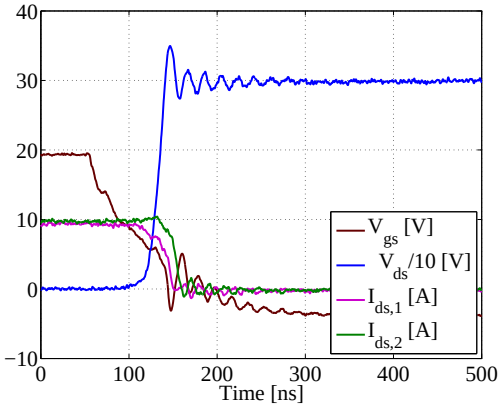

(d) Turn-off transient from the lab experiment

Figure 3.14: Turn-on and turn-off curves from the simulation and the lab experiment

dv/dt and di/dt are calculated to be 14 kV/μs and 404 A/μs respectively.

Additionally, a second SiC MOSFET (SCT2080KE) is also tested in order to observe the difference in performance between the two SiC MOSFETs. The current and the voltage rise times for the SCT2080KE MOSFET are observed to be 26.2 ns and 24 ns respectively. Likewise, the dv/dt is 11 kV/μs and the di/dt is 396 A/μs with a low overshoot and almost no ringings.

It can be seen that the CMF20120 MOSFET is switching faster than the SCT2080KE MOSFET, however, the SCT2080KE has a smaller overshoot and less ringing.

The total stray inductance (L_{stray}) is the sum of $L_{dc-link}$, L_{d1}/L_{d2} and

L_{s1}/L_{s2} which are depicted in Fig. 3.13. It is evident from Fig. 3.14 (d) that the voltage overshoot during the turn-off caused by the total stray inductance and di/dt of 769 A/μs is about 50 V. Thereby the switching loop inductance is estimated to be 50/0.769 = 65 nH. This stray inductance limits the di/dt of the drain current during the turn-on and reduces the drain to source voltage across the device by the factor of $L_{stray} \cdot di/dt$. The stray inductance effectively works as a turn-on snubber and reduces the turn-on losses while increasing it during the turn-off due to the voltage overshoot.

3.4.3 Switching loss and overvoltage in discrete versus paralleled MOSFETs

The study of switching process is mainly intended to obtain the switching losses for energy efficiency analysis. Therefore, the switching losses for the two aforementioned SiC MOSFETs are measured in various load currents. The experiment is repeated for both the discrete SiC MOSFETs (SCT2080KE) and the paralleled ones (two SCT2080KE). The results are shown in Fig. 3.15.

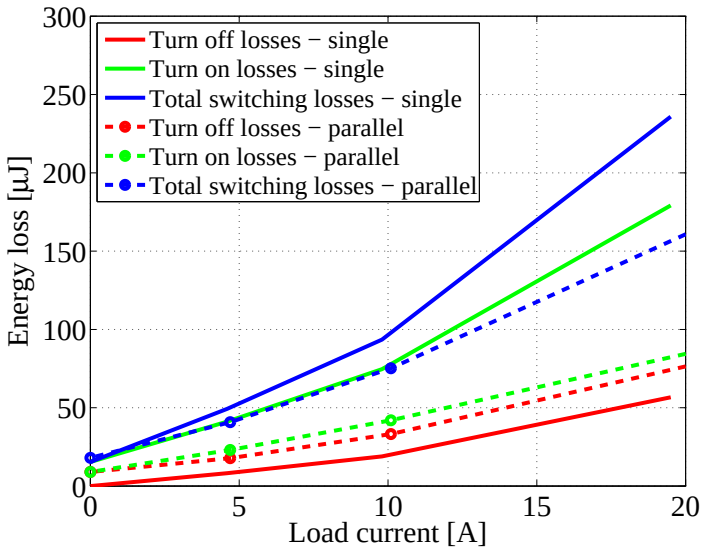

Figure 3.15: Comparison of the switching losses when using a single discrete MOSFET (SCT2080KE) or two parallel ones are used

However, it should be noted, the study of switching losses in SiC MOSFETs is irrelevant without considering the impact of the overvoltages since generally a lower switching loss is achieved by lowering the gate resistance which results

in a higher overvoltage. Therefore, an overvoltage requirement should be put in place before any attempt to reduce the switching losses. In Fig. 3.16, the overvoltage values related to the switching losses shown in Fig. 3.15.

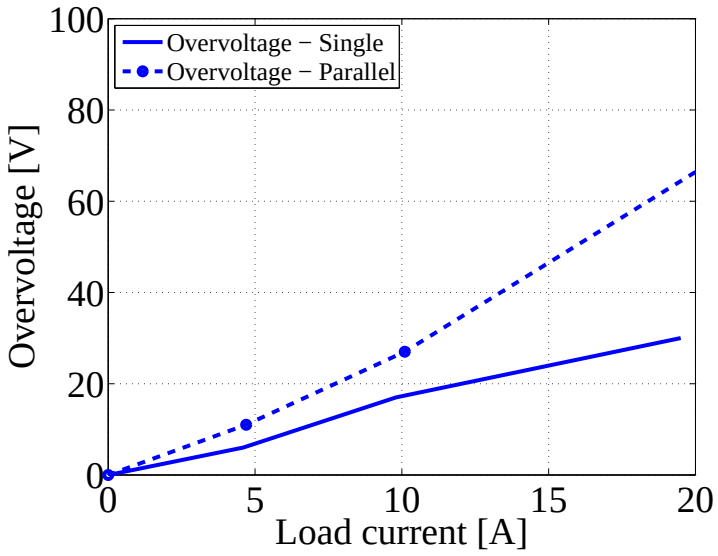

Figure 3.16: Switching losses and overvoltages and their dependencies on the load current when using a single discrete MOSFET (SCT2080KE) or two parallel ones

Apart from the load current, the switching loss is greatly dependent on the operating switching voltage. The switching energy loss of a SiC MOSFET (CMF20120) in various switching voltages is shown in Fig. 3.17.

The switching loss coefficients $k_{V,on}$, $k_{V,off}$, $k_{V,rr}$, $k_{I,on}$, $k_{I,off}$ and $k_{I,rr}$ that relate the losses calculated in the reference current and voltage to other currents and voltages are extracted by measuring the switching losses for various currents and voltages and are presented in Table 3.2.

The switching losses can be reduced by decreasing the switching time through the gate resistor (R_G). The switching energy loss for a lower gate resistance and higher one are shown in Fig. 3.18.

Finally, the total switching losses is shown to increase with an increasing load current and dc-link voltage. However, it is shown to be higher than a linear first order increment. As a result, two parallel SiC MOSFETs have lower total switching losses than a single one for a given load current. On the other hand, this paralleled configuration leads to a higher overvoltage which can be mitigated by increasing the gate resistance, which eventually increases the switching loss.

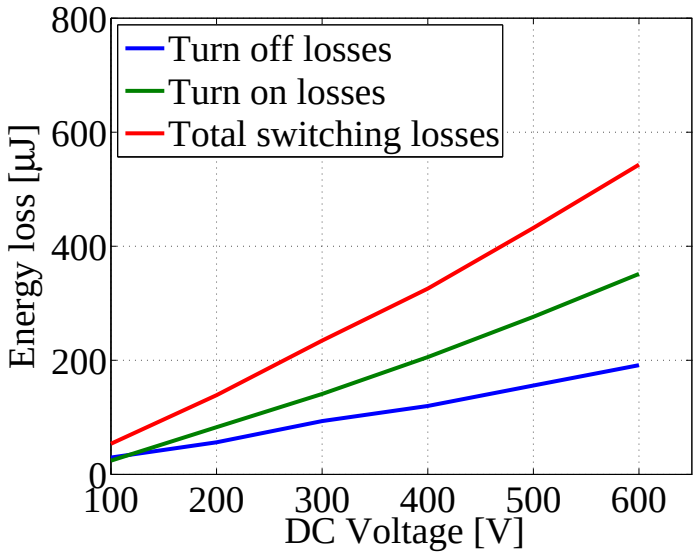

Figure 3.17: Switching energy losses and its dependency on dc-link voltage for two paralleled MOSFETs (CMF20120) with 10 A in each MOSFET

Table 3.2: Experimentally determined switching loss coefficients

Switching device	$k_{I,off}$	$k_{I,on}$	$k_{V,off}$	$k_{V,on}$
CMF20120 (Cree) - Paralleled	1.3	1.4	1	1.5
SCT2080KE (Rohm) - Paralleled	1.3	1.4	1	1.5

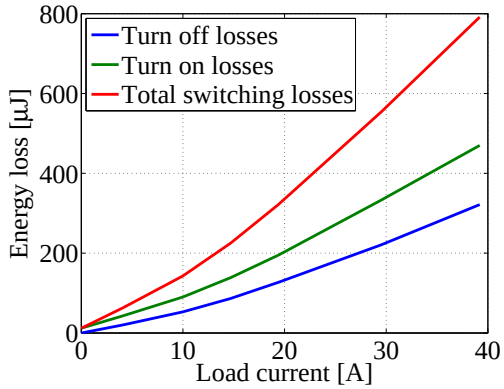

(a) SCT2080KE paralleled with a higher R_g

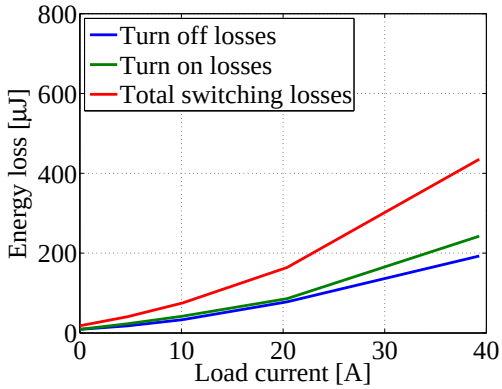

(b) SCT2080KE paralleled with a lower R_g

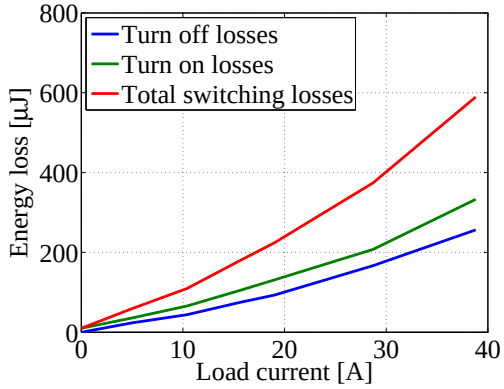

(c) CMF20120 paralleled with a higher R_g

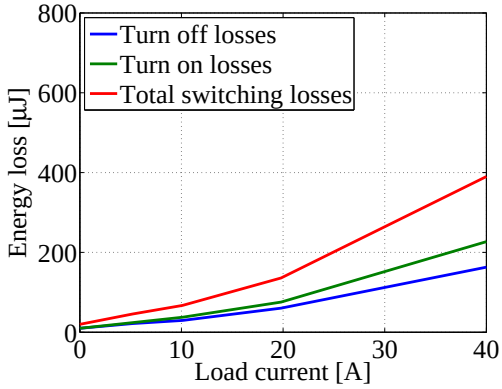

(d) CMF20120 paralleled with a lower R_g

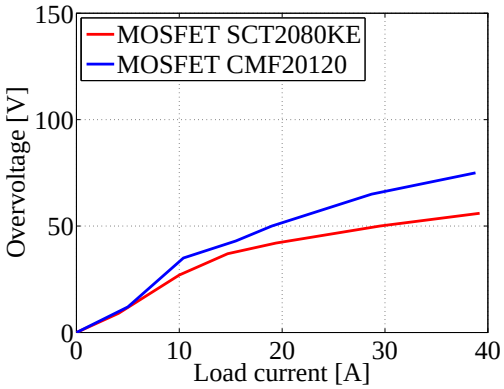

(e) Overvoltage for two different MOSFETs using similarly high gate resistances

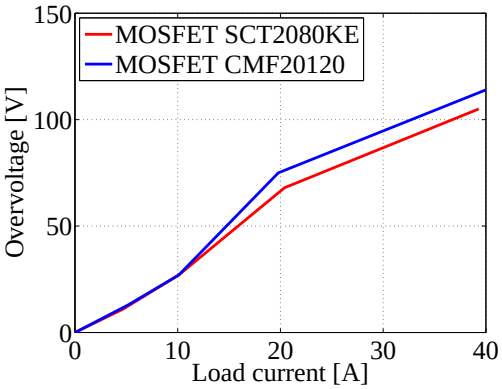

(f) Overvoltage for two different MOSFETs using similarly low gate resistances

Figure 3.18: Switching energy losses of paralleled SiC MOSFETs and their dependencies on the load current for a lower and a higher gate resistor

Chapter 4

Energy efficiency improvement of the electric machines using various control algorithms

In this Chapter, several algorithms for current vector control using MTPA are presented and compared with each other. The main objective of a current vector control is to obtain the required torque reference through a desired current from the machine. However, a secondary objective can be to obtain the required reference torque with the minimum magnitude of current to minimize the copper losses or to obtain the required reference torque with the minimum total losses including both the copper and iron losses.

Furthermore, the vehicle dynamics and a case setup including the parameters of a vehicle and various drive cycles are provided in Section 4.7.2 and 4.7.1 for energy efficiency evaluation of various control strategies.

4.1 Derivation of an ordinary Maximum Torque Per Ampere equation using constant equivalent circuit parameters

A general MTPA control method without the voltage and the current constraints is often derived with the knowledge of the parameters of the PMSM such as L_d, L_q and Ψ_m including an approximation of the torque obtained using these parameters.

The torque equation (2.10) can be simplified using constant parameters

and be rewritten as

$$T_e = \frac{3}{2}p\Big(\Psi_m i_{sq} + (L_d - L_q)i_{sd}i_{sq}\Big) \tag{4.1}$$

The d-q currents and torque can be expressed as a function of current angle by

$$i_{sd} = i_a cos(\beta) \tag{4.2}$$

$$i_{sq} = i_a sin(\beta) \tag{4.3}$$

where i_a is the current magnitude vector and β is the angle toward the d-axis. Consequently the torque equation can be rewritten as

$$T_e = \frac{3}{2}p\Big(\Psi_m i_a sin(\beta) + (L_d - L_q)i_a i_a cos(\beta)sin(\beta)\Big). \tag{4.4}$$

The torque can then be maximized by

$$\frac{dT_e}{d\beta} = 0. \tag{4.5}$$

Finally the current vector angle as a function of current magnitude can then be obtained as

$$cos(\beta) = -\frac{\Psi_m}{4(L_d - L_q)i_a} \pm \sqrt{\frac{\Psi_m^2}{16(L_d - L_q)^2 i_a^2} + \frac{1}{2}} \tag{4.6}$$

However, an inverted fed PMSM has some constraints due to the limitations of the inverter and the supplying DC source. The key limitations are the maximum current and voltage of the machine [54].

$$U_{max} \geq \sqrt{u_{sd}^2 + u_{sq}^2} \tag{4.7}$$

$$I_{max} \geq \sqrt{i_{sd}^2 + i_{sq}^2} \tag{4.8}$$

Therefore, the required torque-speed in the entire operating region of the electric machine cannot be achieved by only using (4.6).

4.2 A procedure to evaluate a control algorithm above the maximum voltage limit

In this section a procedure to obtain MTPA-values for the whole operating region using the ordinary MTPA structure, is presented. Due to the non-linearity of the machine, it is not sufficient to apply only the initially obtained current vectors to the FEA model. The following issues should be addressed.

1) The current reference obtained from the control algorithm (MTPA or any other suggested algorithm) may not lead to a torque sufficiently close to the reference torque desired. In order to achieve sufficient accuracy an iterative procedure has to take place to resolve this problem.

2) Moreover, the MTPA algorithm does not include any voltage limit which is often set due to the converter limitations. Therefore, the current references obtained from the control algorithm might lead to that the maximum voltage values are exceeded in the field weakening area or close to the field weakening area (due to the mismatch between the model anticipated by the algorithm and the actual model used in FEA).

The algorithm flow shown in Fig. 4.1 can resolve the aforementioned issues when using an ordinary MTPA control structure to find the desired current values.

As it can be seen in Fig. 4.1, a compensation is made using the knowledge of the torque reference to make sure that the torque reference is achieved. Besides, a complementary algorithm provides the current vector references when the maximum voltage is reached. The complementary MTPA box uses (4.9-4.12) resulting in 4 equations with 4 variables, which can then provide the i_{sd} and i_{sq} references.

$$u_{sd} = R_s i_{sd} - \omega_{el} L_q i_{sq} \tag{4.9}$$

$$u_{sq} = R_s i_{sq} + \omega_{el} L_d i_{sd} + \omega_{el} \Psi_m \tag{4.10}$$

$$T_e = \frac{3}{2} p(\Psi_m i_{sq} + (L_d - L_q) i_{sd} i_{sq}) \tag{4.11}$$

$$U_{max} = \sqrt{u_{sd}^2 + u_{sq}^2} \tag{4.12}$$

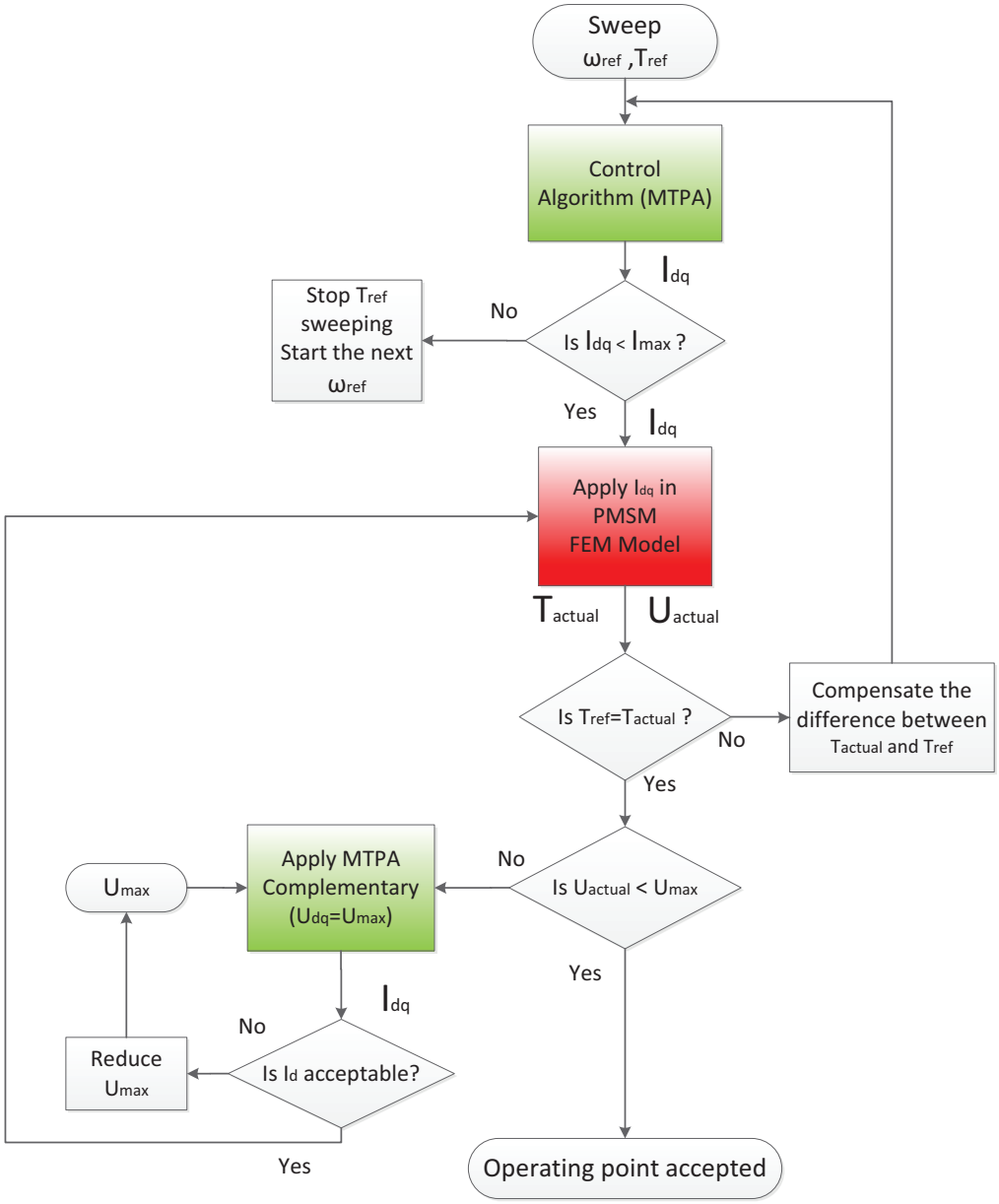

Figure 4.1: The proposed process to evaluate an MTPA algorithm including the complementary MTPA section for obtaining the operating points where the maximum allowed voltage is reached.

4.3 Torque maximization algorithm considering saturation, cross coupling and temperature using Lagrangian method - method I

With the help of the Lagrange multiplier, a function of f_L can be minimized with subject to the equality of $(g_L - c_L) = 0$ [13–15, 55].

In this case, the minimizing function ($f_L = i_{sd}^2 + i_{sq}^2$) is the current magnitude and the subjected equality is the produced torque. Therefore, $c_L = T_{ref}$ and $g_L = T_e$ which is

$$T_e = \frac{3}{2}p\Big(\Psi_d(i_{sd}, i_{sq}, T)i_{sq} - \Psi_q(i_{sd}, i_{sq}, T)i_{sd}\Big). \tag{4.13}$$

The variables are i_{sd}, i_{sq} and T. However, temperature is not a state that should be minimized. Therefore, it is assumed constant for a single optimization and a new optimization is performed for a new temperature reference.

The Lagrangian function(Λ) can, therefore, be expressed as

$$\Lambda = f_L + \lambda(g_L - c_L) = i_{sd}^2 + i_{sq}^2 + \lambda\left(\frac{3}{2}p\Big(\Psi_d(i_{sd}, i_{sq})i_{sq} - \Psi_q(i_{sd}, i_{sq})i_{sd}\Big) - T_{ref}\right) \tag{4.14}$$

Partial derivatives of Λ with respect to the variables i_{sd}, i_{sq} and λ which is an extra variable called Lagrange multiplier are obtained and are then put to zero.

$$\frac{\partial\Lambda}{\partial i_{sd}} = 2i_{sd} + \lambda\frac{3}{2}p(\frac{\partial\Psi_d}{\partial i_{sd}}i_{sq} - \frac{\partial\Psi_q}{\partial i_{sd}}i_{sd} - \Psi_q) = 0 \tag{4.15}$$

$$\frac{\partial\Lambda}{\partial i_{sq}} = 2i_{sq} + \lambda\frac{3}{2}p(\frac{\partial\Psi_d}{\partial i_{sq}}i_{sq} - \frac{\partial\Psi_q}{\partial i_{sq}}i_{sd} + \Psi_d) = 0 \tag{4.16}$$

$$\frac{\partial\Lambda}{\partial\lambda} = \frac{3}{2}p(\Psi_d i_{sq} - \Psi_q i_{sd}) - T_{ref} = 0 \tag{4.17}$$

where λ is eliminated from (4.15) and (4.16) which leads to

$$\frac{\partial\Psi_d}{\partial i_{sq}}i_{sd}i_{sq} + \Psi_d i_{sd} - \frac{\partial\Psi_q}{\partial i_{sq}}i_{sd}^2 - \frac{\partial\Psi_d}{\partial i_{sd}}i_{sq}^2 + \frac{\partial\Psi_q}{\partial i_{sd}}i_{sd}i_{sq} + \Psi_q i_{sq} = 0 \tag{4.18}$$

where $\Psi_d(i_{sd}, i_{sq}), \Psi_q(i_{sd}, i_{sq})$ and their derivatives can be expressed as

$$\Psi_d(i_{sd}, i_{sq}) = L_d(i_{sd}, i_{sq})i_{sd} + \Psi_m(i_{sd}, i_{sq}) \tag{4.19}$$

$$\Psi_q(i_{sd}, i_{sq}) = L_q(i_{sd}, i_{sq}) i_{sq} \tag{4.20}$$

$$\frac{\partial \Psi_d}{\partial i_{sd}} = L_d + \frac{\partial L_d}{\partial i_{sd}} i_{sd} + \frac{\partial \Psi_m}{\partial i_{sd}} \tag{4.21}$$

$$\frac{\partial \Psi_d}{\partial i_{sq}} = \frac{\partial L_d}{\partial i_{sq}} i_{sd} + \frac{\partial \Psi_m}{\partial i_{sq}} \tag{4.22}$$

$$\frac{\partial \Psi_q}{\partial i_{sd}} = \frac{\partial L_q}{\partial i_{sd}} i_{sq} \tag{4.23}$$

$$\frac{\partial \Psi_q}{\partial i_{sq}} = L_q + \frac{\partial L_q}{\partial i_{sq}} i_{sq} \tag{4.24}$$

Inserting all equations from (4.19) to (4.24) in (4.17) and (4.18), the two main Lagrangian equations which maximize the torque become,

$$\begin{aligned} &L_d(i_{sq}^2 - i_{sd}^2) + \tfrac{\partial L_d}{\partial i_{sd}}(i_{sd} i_{sq}^2) + \tfrac{\partial L_d}{\partial i_{sq}}(-i_{sd}^2 i_{sq}) \\ &+L_q(i_{sd}^2 - i_{sq}^2) + \tfrac{\partial L_q}{\partial i_{sd}}(-i_{sd} i_{sq}^2) + \tfrac{\partial L_q}{\partial i_{sq}}(i_{sd}^2 i_{sq}) \\ &+\Psi_m(-i_{sd}) + \tfrac{\partial \Psi_m}{\partial i_{sd}}(i_{sq}^2) + \tfrac{\partial \Psi_m}{\partial i_{sq}}(-i_{sd} i_{sq}) = 0 \end{aligned} \tag{4.25}$$

and

$$\frac{3}{2} p(L_d i_{sd} i_{sq} - L_q i_{sd} i_{sq} + \Psi_m i_{sq}) - Tref = 0 \tag{4.26}$$

where L_d, L_q and Ψ_m are obtained from (2.11) to (2.13) which are extracted from the FEA model of the machine as a function of i_{sd} and i_{sq} in Section 2.2.

(4.25) and (4.26) are two equations which are only a function of i_{sd} and i_{sq}. Therefore, solving these two equations provides the d-q current trajectory. The resulting current trajectories are illustrated in Fig. 4.2 together with the torque per current loci with a range between 0 to 0.62 [N.m/A].

Since none of the equations used in method I depend on rotational speeds, the current trajectories are expected to be independent of the rotational speed as can be seen in Fig. 4.2. The current trajectories for the 1000 RPM and 3000 RPM cases completely overlap on each other and they closely follow the maximum torque per ampere loci. However, at 5000 RPM, the current trajectory initially overlap with the 1000 RPM and 3000 RPM trajectories until it reaches the maximum allowed voltage limit. Thereafter, the algorithm which

is used for extraction of the current trajectory is changed to the complementary MTPA explained in Section 4.2.

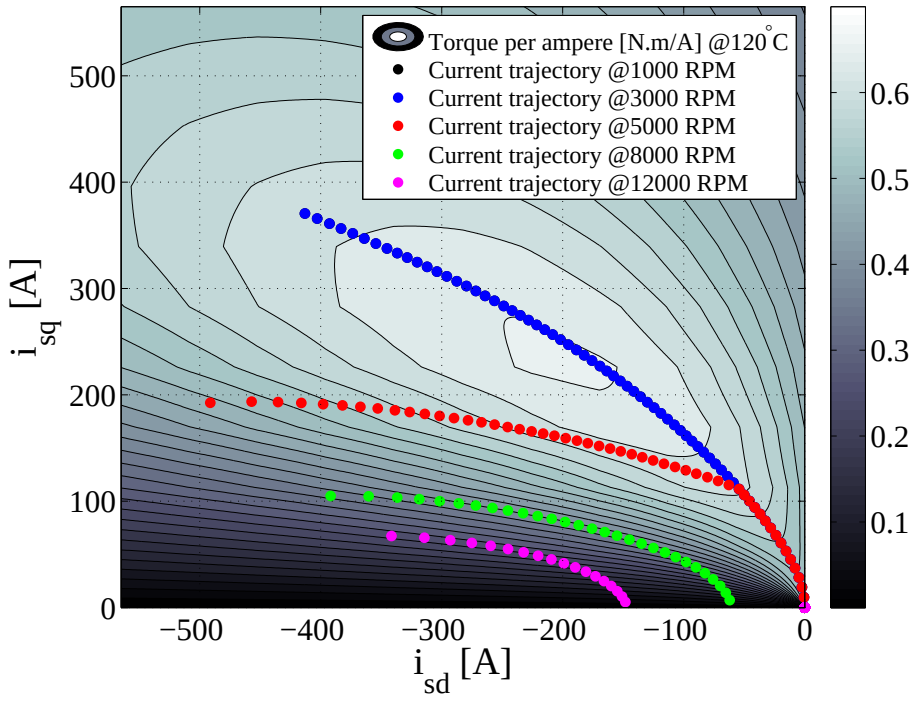

Figure 4.2: Torque per ampere loci obtained from the FEA shown together with the d-q current trajectory using method I in various speeds.

4.3.1 Comparison of various control strategies

In this section the current references obtained by the proposed MTPA method is compared with several other MTPA methods. The following MTPA algorithms are used in the comparison toward the torque per ampere trajectories obtained from the FEA directly.

- Case I: A constant angle between the d-q currents which is obtained from an ordinary MTPA that maximizes the output torque at the highest reference torque and current magnitude with parameters $L_d = 175\mu H$, $L_q = 375\mu H$ and $\Psi_m = 0.0685\ Wb$.
- Case II: An ordinary MTPA with constant parameters which are chosen from the low current operating area of the machine ($L_d = 250\mu H$,

$L_q = 750\mu H$ and $\Psi_m = 0.0952\ Wb$).

- Case III: An ordinary MTPA with constant parameters which are chosen from the high current operating area of the machine ($L_d = 175\mu H$, $L_q = 375\mu H$ and $\Psi_m = 0.0685\ Wb$).

- Case IV: An ordinary MTPA with variable parameters which are updated outside the MTPA algorithm depending on the current operating point of the machine (i_{sd} and i_{sq}).

- Case V: The proposed MTPA where the variable parameters are included in the maximization algorithm of MTPA.

As it can be seen in Fig. 4.3, the proposed MTPA (Case V) is the closest to the absolute torque per ampere loci obtained from the FEA in the entire region. However, the other algorithms diverge from the actual maximum torque per ampere points to different extents.

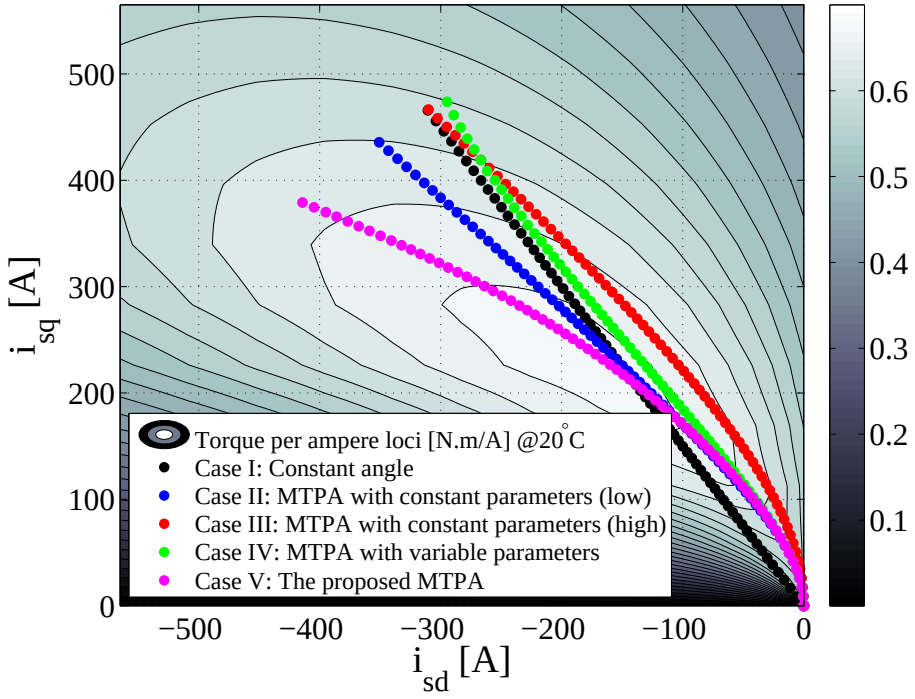

Figure 4.3: Torque per ampere loci obtained from the FEA shown together with the d-q current trajectory using several methods.

As could be expected, an ordinary MTPA with variable parameters updating outside the MTPA algorithm (Case IV), provides a trajectory similar to Case II at lower current ratings. However, as the current increases, the trajectory changes to become more similar to Case III. A more significant finding from Case IV is that that updating the parameters outside the minimization process, which is a popular approach in the literature, would actually make the current trajectory diverge from the absolute maximum torque per ampere.

In Fig. 4.4 only the proposed algorithm (Case IV) and the ordinary MTPA with variable parameters (Case IV) are shown for three different operating temperatures. It can be seen than the temperature is not affecting the MTPA current trajectory for each method alone.

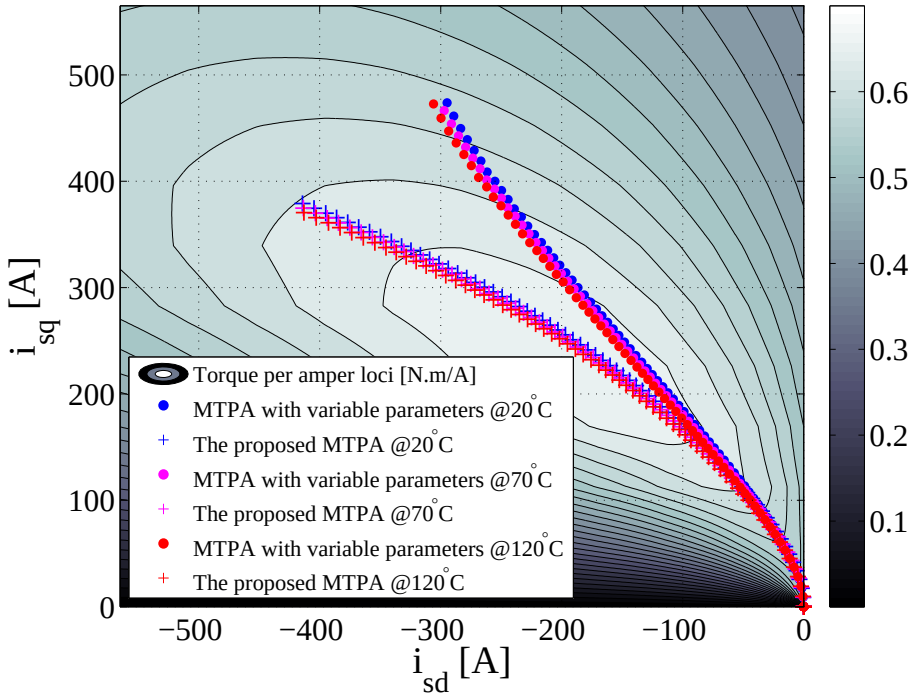

Figure 4.4: The d-q current trajectory using an ordinary MTPA with variable parameters and the proposed MTPA (method I) in several temperatures shown together with torque per ampere loci obtained from the FEA.

In Fig. 4.5 the total energy efficiency improvement of the machine is shown in the entire torque-speed operating region of the machine. The energy efficiency impact is mostly unchanged except at the very high torque region. In this region, it can be noted that the efficiency can be improved up to 5 %

at very low speeds and very high torques. This means that the operation of the electric machine at initial high torque which in a real application often is limited due to a certain time constant, can be extended.

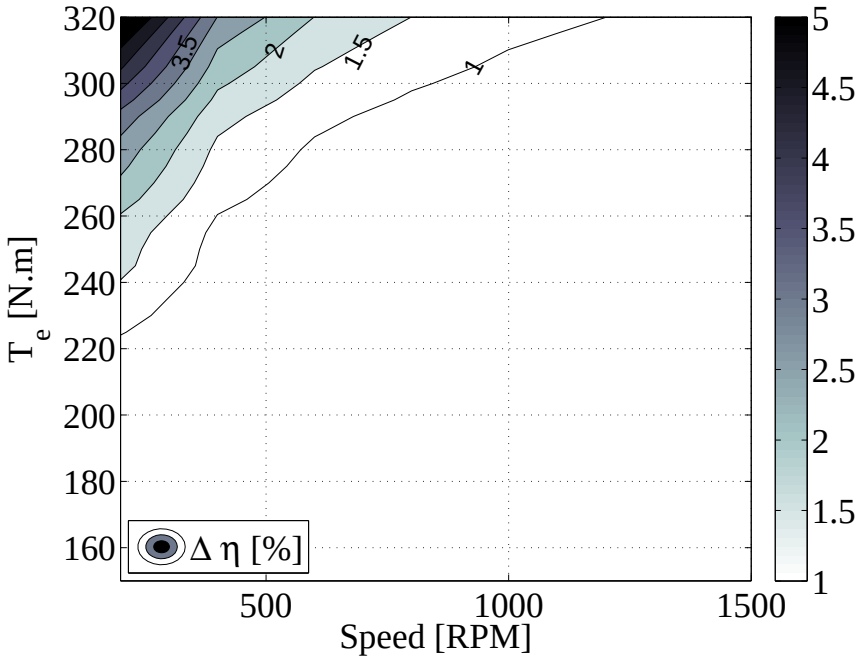

Figure 4.5: Efficiency improvement due to the use of the proposed MTPA instead of the ordinary MTPA with variable parameters at 120°C.

4.4 Torque performance impact due to method I

In Section 4.3.1, the resulting current trajectories in the various control algorithms are compared with each other in a set of reference torque values. However, the impact of using the proposed control strategy versus the ordinary MTPA with variable L_d and L_q on the maximum available torque is of interests. This can be achieved by comparing the control algorithms in a common reference current magnitude instead of a common reference torque value.

Therefore, a peak current magnitude of 555 A is chosen and each method is used to derive the d-q current trajectory. Thereafter, the d-q current trajectories are evaluated using FEA and the output torque is observed.

The proposed control strategy provides a current reference of I_{sd} = -408 A and, I_{sq} = 376 A which results in a torque of 357.6 N.m whereas the MTPA using variable L_d and L_q provides current references of I_{sd} = -291.5 A and I_{sq} = 471 A which results in a torque of 333.2 N.m. This corresponds to a torque increase of more than 7 % for this current magnitude. This means that the low-speed and standstill torque characteristics of a vehicle using this machine can be improved by 7 % when using the proposed MTPA instead of an MTPA algorithm where the L_d and L_q parameters are updated online.

4.5 Loss minimization algorithm considering saturation, cross coupling, temperature and irons losses using Lagrangian method - method II

The solution provided in Section 4.3 minimizes the ohmic losses for a given operating point by maximizing the torque for a given current magnitude. A further improvement step is to have a solution that minimizes the total losses including the ohmic losses, iron losses or even the purely resistive converter losses. This can be achieved by redefining (4.27) as

$$\Lambda = P_{cu} + P_{fe} + \lambda(\frac{3}{2}p(\Psi_d(i_{sd}, i_{sq})i_{sq} - \Psi_q(i_{sd}, i_{sq})i_{sd}) - T_{ref}) \tag{4.27}$$

where P_{fe} is obtained from (2.16) and P_{cu} is the ohmic losses of the windings (r_w) and end windings (r_{ew}) which can be represented by one resistance ($R_s(T)$) as

$$R_s = r_w(T) + r_{ew}(T) \tag{4.28}$$

$$P_{cu} = R_s(i_{sd}^2 + i_{sq}^2) \tag{4.29}$$

Partial derivatives of Λ with respect to the variables i_{sd}, i_{sq} and λ are obtained and are then put to zero.

$$\frac{\partial \Lambda}{\partial i_{sd}} =$$
$$2R_s i_{sd} + P_{fe10} + 2P_{fe20}i_{sd} + P_{fe11}i_{sq} + \lambda\frac{3}{2}p(\frac{\partial \Psi_d}{\partial i_{sd}}i_{sq} - \frac{\partial \Psi_q}{\partial i_{sd}}i_{sd} - \Psi_q) = 0 \tag{4.30}$$

$$\frac{\partial \Lambda}{\partial i_{sq}} =$$
$$2R_s i_{sq} + P_{fe01} + 2P_{fe02} i_{sq} + P_{fe11} i_{sd} + \lambda \frac{3}{2} p(\frac{\partial \Psi_d}{\partial i_{sq}} i_{sq} - \frac{\partial \Psi_q}{\partial i_{sq}} i_{sd} + \Psi_d) = 0 \tag{4.31}$$

$$\frac{\partial \Lambda}{\partial \lambda} = \frac{3}{2} p(\Psi_d i_{sq} - \Psi_q i_{sd}) - T_{ref} = 0 \tag{4.32}$$

where λ is eliminated from (4.30) and (4.31) which leads to

$$\begin{gathered}
\Psi_d((2R_s + 2P_{fe20})i_{sd} + P_{fe11} i_{sq} + P_{fe10}) \\
+\Psi_q((2R_s + 2P_{fe02})i_{sq} + P_{fe11} i_{sd} + P_{fe01}) \\
+\tfrac{\partial \Psi_d}{\partial i_{sd}}(-(2R_s + 2P_{fe02})i_{sq}^2 - P_{fe11} i_{sd} i_{sq} - P_{fe01} i_{sq}) \\
+\tfrac{\partial \Psi_d}{\partial i_{sq}}((2R_s + 2P_{fe20})i_{sd} i_{sq} + P_{fe11} i_{sq}^2 + P_{fe10} i_{sq}) \\
+\tfrac{\partial \Psi_q}{\partial i_{sd}}((2R_s + 2P_{fe02})i_{sd} i_{sq} + P_{fe11} i_{sd}^2 + P_{fe01} i_{sd}) \\
+\tfrac{\partial \Psi_q}{\partial i_{sq}}(-(2R_s + 2P_{fe20})i_{sd}^2 - P_{fe11} i_{sd} i_{sq} - P_{fe10} i_{sd}) \;=\; 0
\end{gathered} \tag{4.33}$$

By using (4.19) to (4.24) in (4.17) and (4.18), flux linkage equations are functions of the equivalent circuit parameters L_d, L_q, Ψ_m.

$$\begin{gathered}
\Psi_m(2R_s + 2P_{fe20})i_{sd} + \Psi_m P_{fe11} i_{sq} + \Psi_m P_{fe10} \\
+L_d i_{sd}^2(2R_s + 2P_{fe20}) + L_d i_{sd} i_{sq} P_{fe11} + L_d i_{sd} P_{fe10} \\
+L_q i_{sq}^2(2R_s + 2P_{fe02}) + L_q i_{sd} i_{sq} P_{fe11} + L_q i_{sq} P_{fe01} \\
-L_d i_{sq}^2(2R_s + 2P_{fe02}) - L_d i_{sd} i_{sq} P_{fe11} - L_q i_{sq} P_{fe01} \\
-\tfrac{\partial L_d}{\partial i_{sd}} i_{sd} i_{sq}^2(2R_s + 2P_{fe02}) - \tfrac{\partial L_d}{\partial i_{sd}} i_{sd}^2 i_{sq} P_{fe11} - \tfrac{\partial L_d}{\partial i_{sd}} i_{sd} i_{sq} P_{fe01} \\
+\tfrac{\partial L_d}{\partial i_{sq}} i_{sd}^2 i_{sq}(2R_s + 2P_{fe20}) + \tfrac{\partial L_d}{\partial i_{sq}} i_{sd} i_{sq}^2 P_{fe11} + \tfrac{\partial L_d}{\partial i_{sq}} i_{sd} i_{sq} P_{fe10} \\
+\tfrac{\partial \Psi_m}{\partial i_{sq}} i_{sd} i_{sq}(2R_s + 2P_{fe20}) + \tfrac{\partial \Psi_m}{\partial i_{sq}} i_{sq}^2 P_{fe11} + \tfrac{\partial \Psi_m}{\partial i_{sq}} i_{sq} P_{fe10} \\
\tfrac{\partial L_q}{\partial i_{sd}} i_{sd} i_{sq}^2(2R_s + 2P_{fe02}) + \tfrac{\partial L_q}{\partial i_{sd}} i_{sq}^2 i_{sd} P_{fe11} + \tfrac{\partial L_q}{\partial i_{sd}} i_{sd} i_{sq} P_{fe01} \\
-L_q i_{sd}^2(2R_s + 2P_{fe20}) - L_q i_{sd} i_{sq} P_{fe11} - L_q i_{sd} P_{fe10} \\
-\tfrac{\partial L_q}{\partial i_{sq}} i_{sd}^2 i_{sq}(2R_s + 2P_{fe20}) - \tfrac{\partial L_q}{\partial i_{sq}} i_{sd} i_{sq}^2 P_{fe11} - \tfrac{\partial L_q}{\partial i_{sq}} i_{sd} i_{sq} P_{fe10} = 0
\end{gathered} \tag{4.34}$$

$$\frac{3}{2}p(L_d i_{sd} i_{sq} - L_q i_{sd} i_{sq} + \Psi_m i_{sq}) - Tref = 0 \tag{4.35}$$

where L_d, L_q and Ψ_m are obtained from (2.11) to (2.13) which are obtained from the FEA model of the machine as functions of i_{sd} and i_{sq} in Section 2.2.

This results in a d-q current trajectory which is illustrated in Fig. 4.6. Although the difference between the current trajectory is very little at lower rotations speeds such as 1000 RPM and 3000 RPM, they do not have a complete overlap as in method I. This is due to the fact that the parameters modelling the iron losses changes with the rotation speed. As the speed increases, the iron losses increases, thus the loss minimization method needs to provide a different current trajectory to minimize the total losses. This is more visible at 5000 RPM where the iron loss is sufficiently high so that the proposed optimization suggest a current trajectory more in the direction of the d-axis to reduce the iron losses.

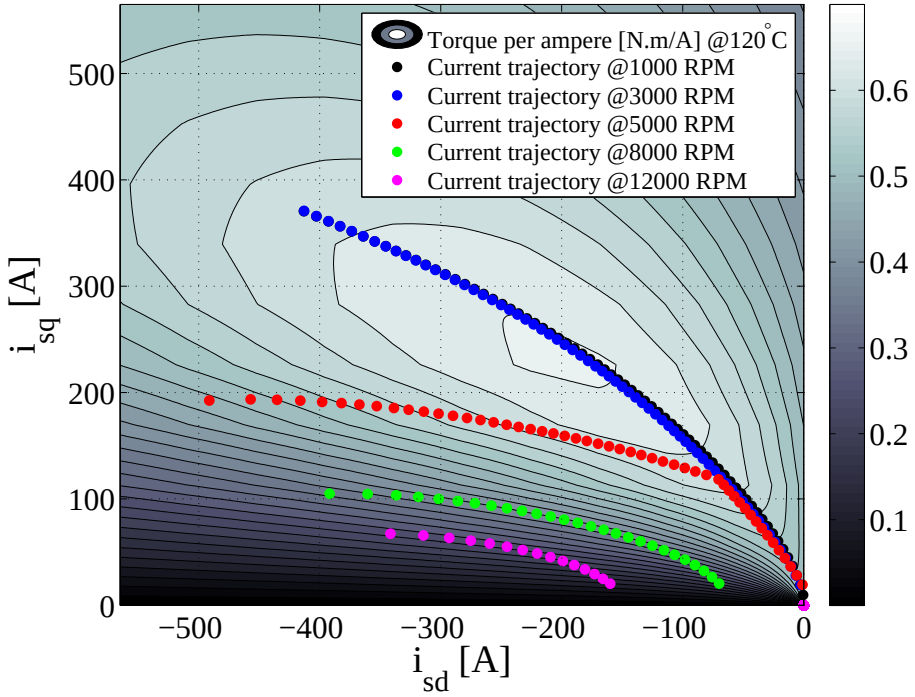

Figure 4.6: The d-q current trajectory obtained by method II in various speeds shown together with torque per ampere loci obtained from the FEA.

In order to investigate the impact of method II, the current trajectories

obtained by method II are compared with method I in Figs. 4.7 and 4.8. In Fig. 4.7 the current trajectories are illustrated together with the torque per ampere loci whereas in Fig. 4.8 the current trajectories are illustrated together with the torque per loss loci.

As it can be seen in Figs. 4.7 and 4.8 the difference between the proposed methods I and II is minimal.

It can also be seen that the maximum torque per ampere loci in Fig. 4.7 is similar the maximum torque per unit loss in Fig. 4.8. Therefore, method I which provides the maximum torque per ampere should not be very different from the results obtained by using method II which provides the maximum torque per unit loss. This is due to the fact that total iron loss of the machine obtained from FEA which is shown in Fig. 2.6 is increasing towards both d- and q-direction. This behaviour resembles the ohmic losses. Therefore, the provided current trajectory in method II is not very different from method I where the iron losses are not included.

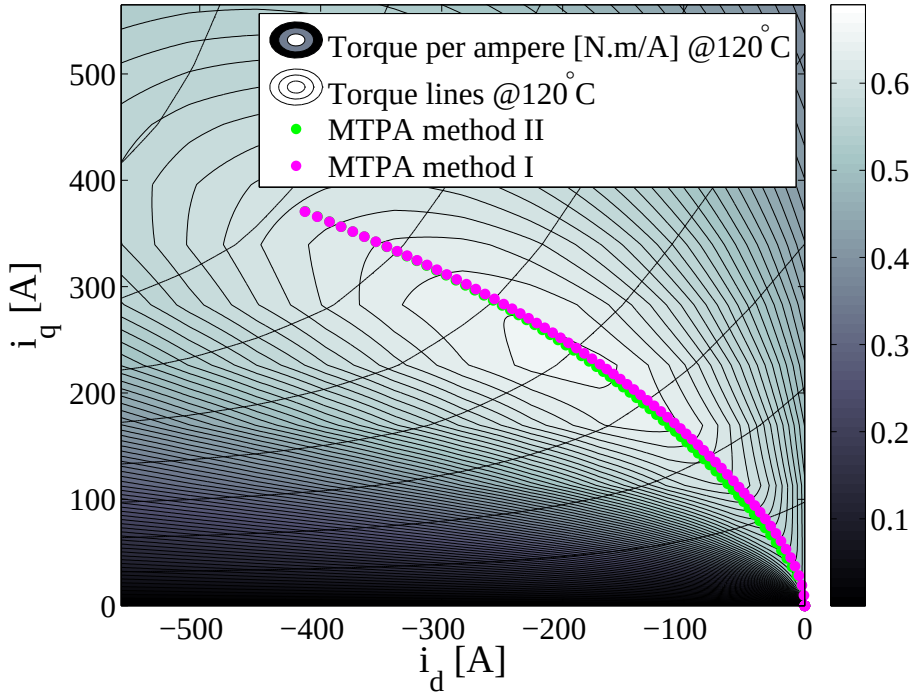

Figure 4.7: Torque per ampere loci obtained from the FEA shown together with the d-q current trajectory using method I and II for a single speed.

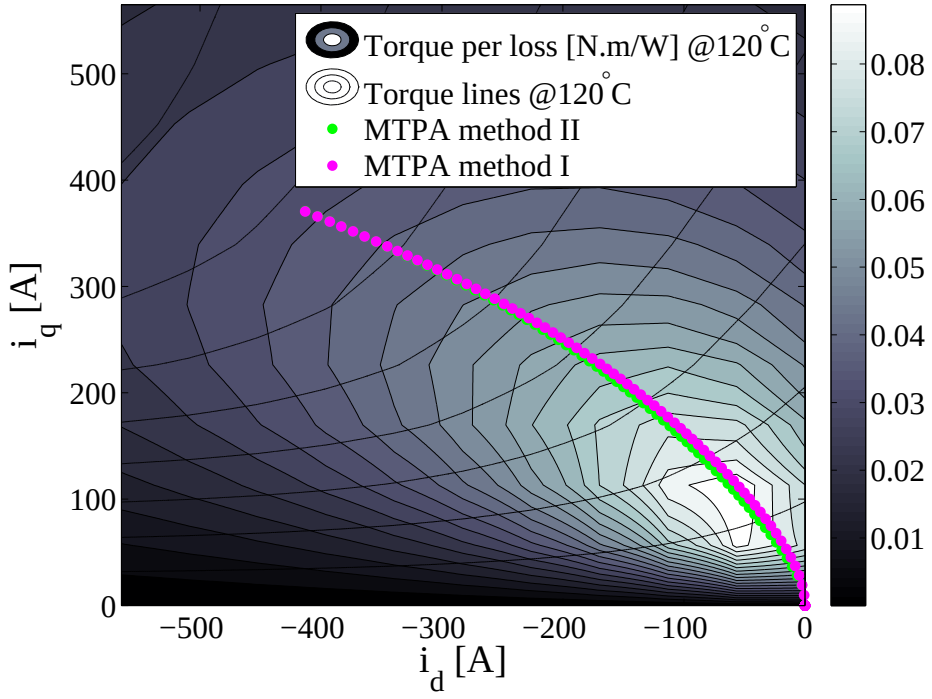

Figure 4.8: Torque per unit loss loci obtained from the FEA shown together with the d-q current trajectory using method I and II for a single speed.

On the other hand, with a threefold increase of the iron losses in the q-direction, the difference between there two methods can be more significant. This assumption is an exaggerated PMSM with much higher iron losses where a simple iron loss modelling is used for optimization. The results can be seen in Figs. 4.9 and 4.10.

It can be seen in Fig. 4.9 that method I provides a trajectory closest to the maximum torque per ampere loci. However, as it can be seen in Fig. 4.10, method II provides a trajectory which is closest to the maximum torque per unit loss instead. This is obtained by bending the current trajectory more toward the d-direction to reduce the iron losses.

It should be noted that the proposed method II provides a possibility to include the losses of other components such as the converter in the minimization method. With a purely resistive inverter losses such as the conduction losses of the inverter, the on-state resistance of the MOSFET can simply be added to the total stator resistance of the machine.

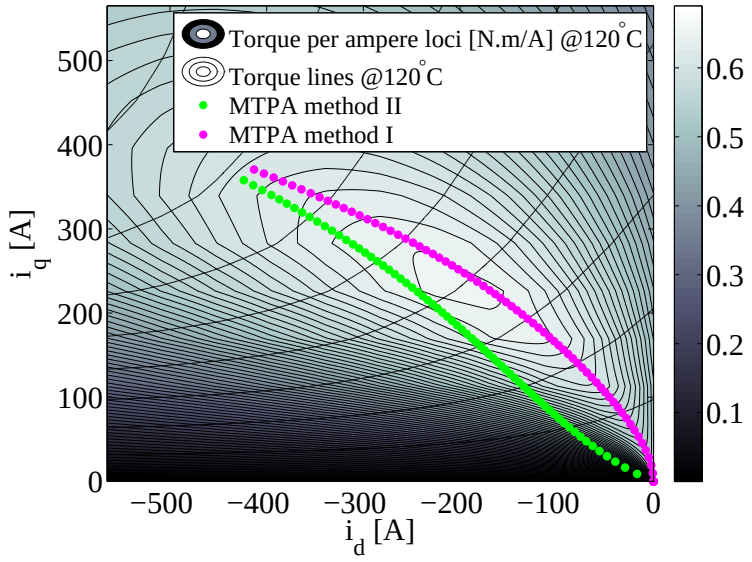

Figure 4.9: Torque per ampere loci [N.m/A] shown together with the d-q current trajectories using method I and II for a machine with threefold iron losses on q-axis.

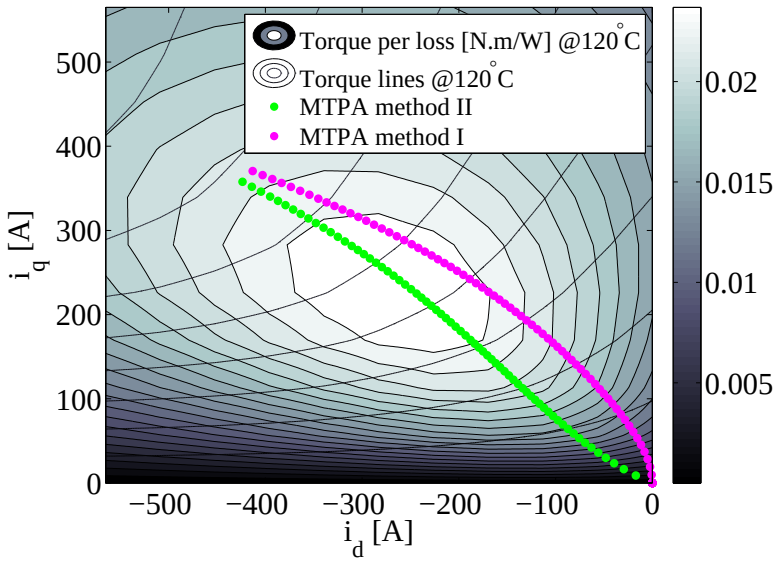

Figure 4.10: Torque per unit loss loci [N.m/W] shown together with the current trajectories using method I and II for a machine with threefold iron losses on q-axis.

4.6 Loss minimization algorithm considering saturation, cross coupling, temperature and irons losses using a non-linear optimization method - method III

The proposed method I in Section 4.3 and method II in Section 4.5 provide the maximum torque per ampere and maximum torque per unit loss respectively. However, in both methods, a similar approach as explained in Section 4.2 is used when the maximum voltage limit is reached since the Lagrangian method is unable to inherently include an additional nonlinear limitation. Therefore, in this section, a non-linear loss minimizing optimization algorithm (method III), which is explained in [6], is implemented to find the current trajectory for the entire operating region of the machine. By using this algorithm, similar results to method II are expected since the Lagrangian multiplier is similarly minimizing the total losses until the voltage limit is reached. Therefore, the only difference between method II and III would be in the region where the maximum voltage is reached. With this method, the voltage limit can be directly implemented in the non-linear optimization algorithm leading to a more optimum solution in the extended MTPA region of the machine.

The main purpose of this optimization is to minimize the target function $f_N(N_L)$ subject to the following constraints

$$A_N \cdot X_N = B_N \qquad Linear\ equality \tag{4.36}$$
$$C_N \cdot X_N \leq D_N \qquad Linear\ non-equality \tag{4.37}$$
$$E_N(X_N) = 0 \qquad Non-linear\ equality \tag{4.38}$$
$$F_N(X_N) \leq 0 \qquad Non-linear\ non-equality \tag{4.39}$$

The target function $f_N(N_L)$ consists of the copper losses and core losses which can be introduced as

$$f_N(X_N) \;=\; P_{cu} + P_{fe} \tag{4.40}$$

where the copper losses and iron losses are defined as in (2.14) and (2.16) respectively. This results in

$$f_N(X_N) \;= \frac{3}{2}R_s(T)(i_{sd}^2 + i_{sq}^2) + P_{fe0} + P_{fe10}i_{sd} + P_{fe01}i_{sq} + P_{fe20}i_{sd}^2 + P_{fe11}i_{sd}i_{sq} + P_{fe02}i_{sq}^2 \tag{4.41}$$

The state matrix X_N is chosen to be

$$X_N = \begin{bmatrix} i_{sd} \\ i_{sq} \\ u_{sd} \\ u_{sq} \end{bmatrix} \tag{4.42}$$

The linear equality and non-equality matrix are not used. However, the non-linear equality and non-linear non-equality matrix are defined as

$$E_N(X) = \begin{bmatrix} T_{ref} - \frac{3}{2}p\Big(\Psi_m(i_{sq})i_{sq} + \big(L_d(i_{sd}, i_{sq}) - L_q(i_{sd}, i_{sq})\big)i_{sd}i_{sq}\Big) \\ u_{sd} - \Big(R_s(T)i_{sd} - \omega_{el}L_q(i_{sd}, i_{sq})i_{sq}\Big) \\ u_{sq} - \Big(R_s(T)i_{sq} + \omega_{el}L_d(i_{sd}, i_{sq})i_{sd} + \omega_{el}\Psi_m(T, i_{sq})\Big) \end{bmatrix} \tag{4.43}$$

$$F_N(X) = \begin{bmatrix} -U_{max} + \sqrt{u_{sd}^2 + u_{sq}^2} \\ -I_{max} + \sqrt{i_{sd}^2 + i_{sq}^2} \end{bmatrix} \tag{4.44}$$

The resulting d-q current trajectory is illustrated in Fig. 4.11.

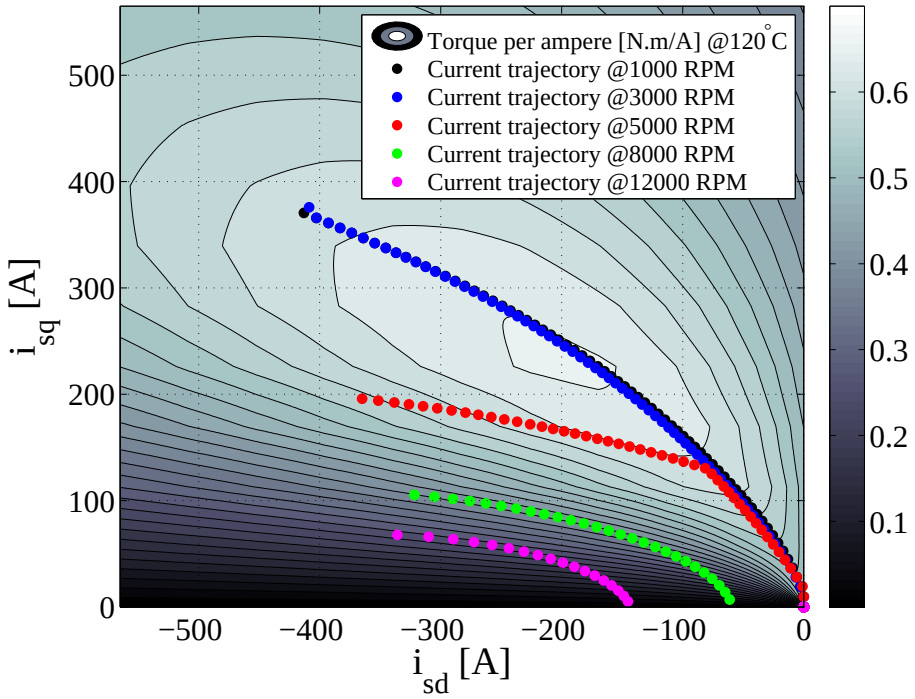

Figure 4.11: The d-q current trajectory obtained by method III in various speeds shown together with torque per ampere loci obtained from the FEA.

Similar to method II which is shown in Fig. 4.6, the difference between the current trajectories in lower speeds is insignificant. However, at higher speeds some difference can be observed.

In Fig. 4.12 the current trajectory between method II and III is shown at 3000 RPM where the maximum voltage is not reached. As it can be expected, there is no visible difference.

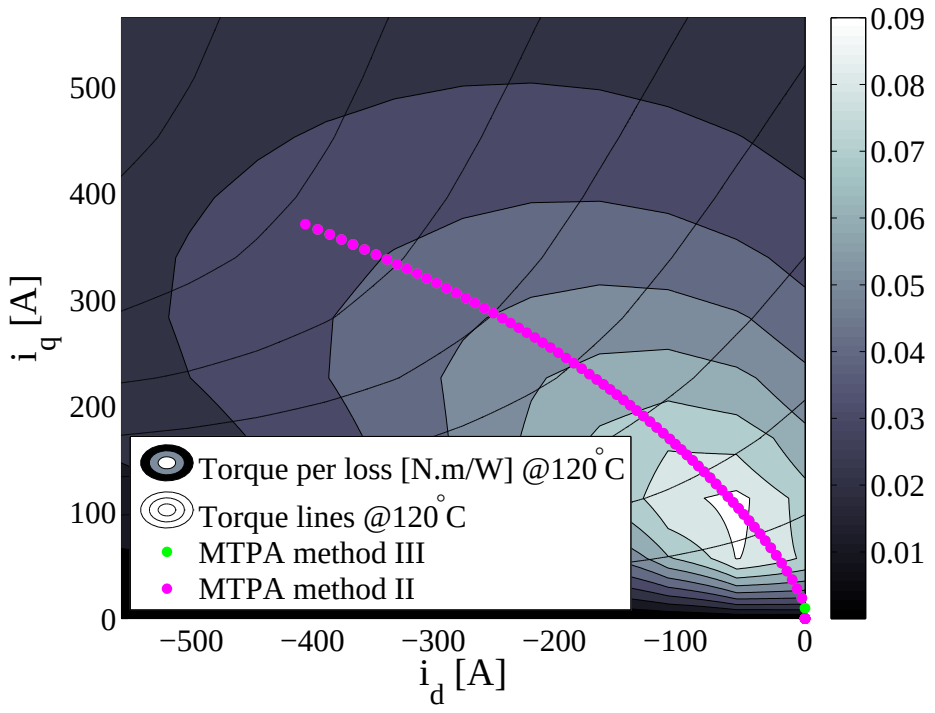

Figure 4.12: Torque per unit loss loci [N.m/W] shown together with the d-q current trajectories using method II and method III @3000 RPM

However, as it can be seen in Fig. 4.13 the power loss difference between these two methods (Method II and III) is visible at higher rotational speeds. Method II and the previous methods use the complementary MTPA method explained in Section 4.2 when the maximum voltage is reached since the Lagrangian multiplier method cannot include the voltage limit in the minimization algorithm. However, in a non-linear loss minimization method the maximum voltage limit can be included in the optimization method, therefore, the optimization can be achieved for the entire operating region of the machine.

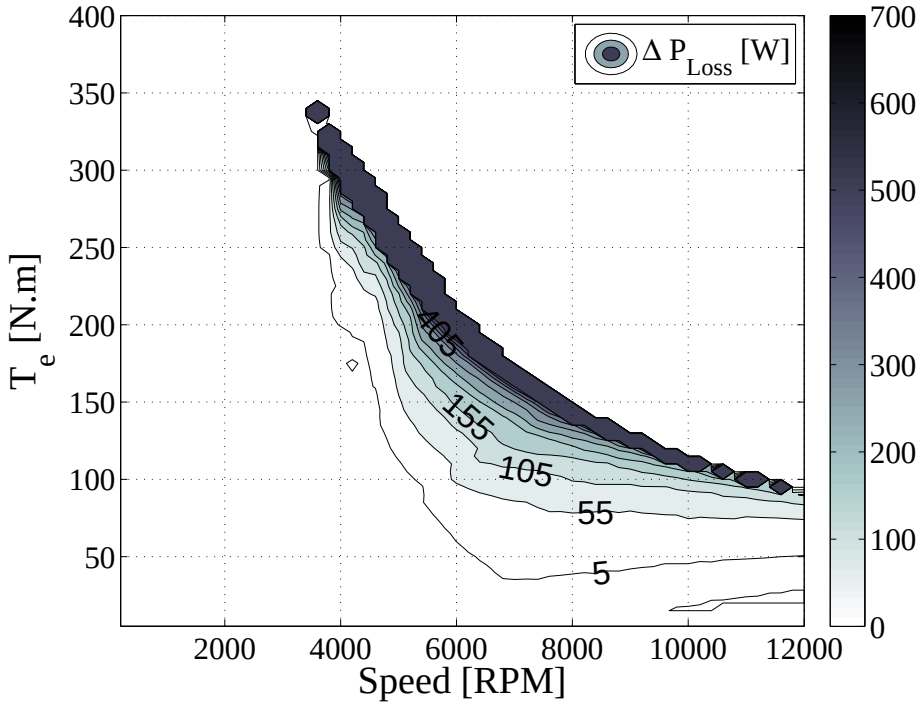

Figure 4.13: Total power loss difference between method II and III ($P_{loss,method\ II} - P_{loss,method\ III}$)

4.7 Drive cycle energy efficiency

The efficiency improvement impact of various control algorithm methods which are discussed in Section 4.3 to 4.6 provide an overview for the energy efficiency of the PMSM using various control methods. In this section an overview of the energy efficiency when the PMSM is used in an actual vehicle is evaluated. Therefore, a vehicle case setup including the vehicle parameters, drive cycles and the vehicle dynamics are used to obtain the operating points where the PMSM is operated. Then, the control algorithms (methods I, II and III) which are explained in the previous sections are compared from an energy efficiency perspective.

4.7.1 Vehicle case setup

The specifications of a suitable vehicle (Renault Master Minibus) is selected for this thesis can be found in Table 4.1. Some selected automotive drive

Table 4.1: Vehicle Parameters

Parameter	Vehicle
Air density (ρ)	1.2 kg/m^3
Air drag coefficient (C_d)	0.5
Frontal area (A_f)	4.8 m^2
Rolling resistance coefficient (C_r)	0.009
Wheel radius (r_{wheel})	0.34798 m
Vehicle mass (m)	2770 kg
Gear box ratio (R_{GB})	9

cycles were used in the investigation. New European Driving Cycle (NEDC) is a widely used drive cycle used for legislations and Artemis is a group of drive cycles which are developed to represent the real-world drive cycles in a joint European project [56]. Finally, a real drive cycle using the selected vehicle from Chalmers University in Gothenburg to Sahlgrenska hospital and the return trip, is also used. The speed shapes of the drive cycles are shown in Fig. 4.14.

4.7.2 Static relation of the electric machine versus the vehicle movement

In a drive cycle, the road angle slope (α), the speed reference ($V_{drive\ cycle}$ [km/h]) and the vehicle acceleration(a) which are obtained from the drive cycle. The required vehicle traction force can then be calculated as [57]

$$F = ma + \frac{1}{2}\rho C_d A_f V_{drive\ cycle}^2 + C_r mg + mg\sin\alpha \tag{4.45}$$

where the ρ is the air density, C_d is the air drag coefficient, A_f is the frontal area of the vehicle, C_r is the rolling resistance coefficient and g is the acceleration due to gravity which can be found in Table 4.1. The road angle slope (α) for the selected drive cycles is zero.

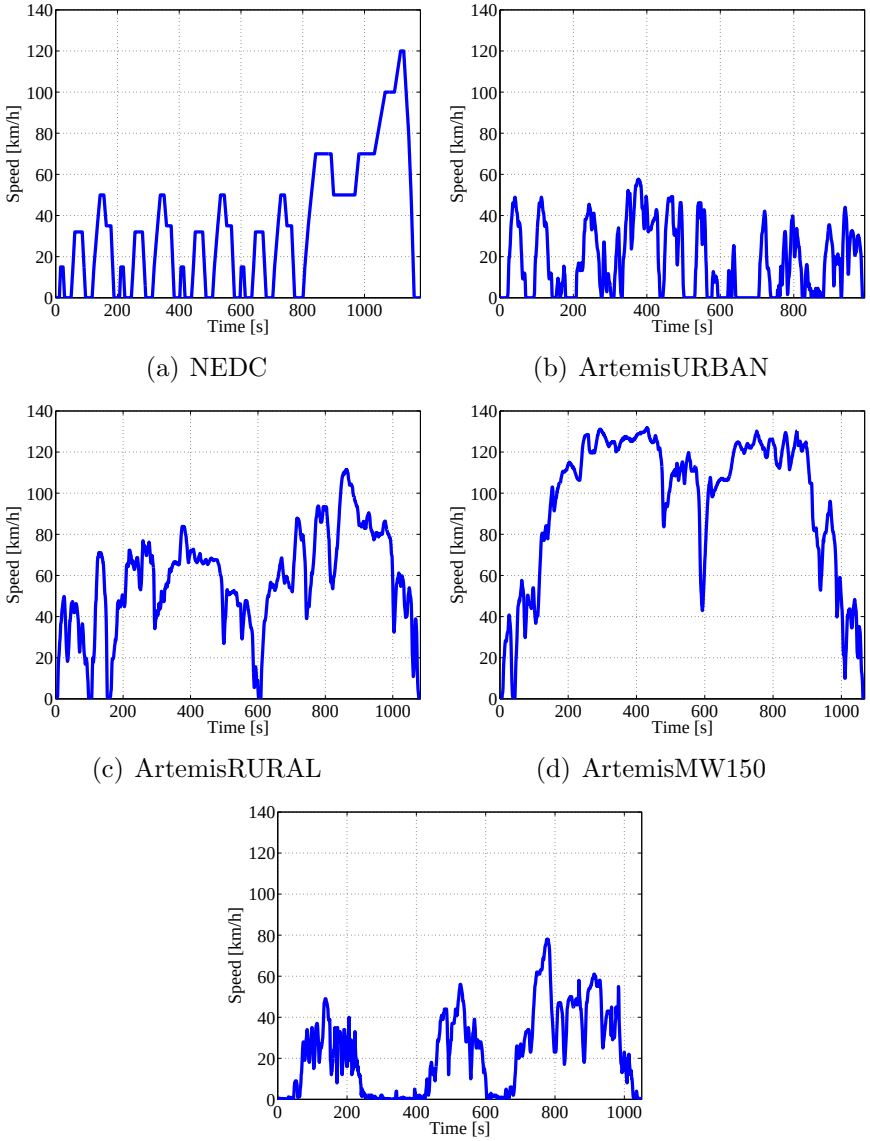

(a) NEDC

(b) ArtemisURBAN

(c) ArtemisRURAL

(d) ArtemisMW150

(e) Chalmers University - Sahlgrenska Hospital (round trip)

Figure 4.14: Drive cycles

The required traction force (F) and the speed reference ($V_{drive\ cycle}$ [km/h]) from the drive cycle are, then transformed to torque (T_{motor}) and speed (V_{motor}) references which need to be provided by the electric machine to fulfill the drive cycle.

$$T_{motor} = \frac{F \cdot r_{wheel}}{R_{GB}} \tag{4.46}$$

$$V_{motor} = V_{drive\ cycle} R_{GB} \frac{60}{3.6 \cdot 2 \cdot \pi \cdot r_{wheel}} \tag{4.47}$$

where r_{wheel} is the wheel radius and R_{GB} is the gear box ratio which can be found in Table 4.1.

4.7.3 Drive cycle energy efficiency impact due to the proposed MTPA algorithms

The selected drive cycles shown in Fig. 4.14 are used to obtain the demanded power which should be provided by the vehicle and the electric machine. The demanded torque and rotation speeds on the electric machine for the selected drive cycles are shown in Fig. 4.15.

The difference between the proposed control strategy (Method I, II and II) and the MTPA with variable parameters affect the power loss and efficiency of the machine. The average efficiency improvement using the proposed methods for various drive cycles is shown in Table 4.2.

Table 4.2: Energy loss decrease due to the proposed MTPA instead of the ordinary MTPA with variable parameters and the percentage of energy loss decrease over the total energy required by various drive cycles.

Drive cycle	Method I (%)	Method II (%)	Method III (%)
NEDC	0.004	0.025	0.051
Artemis Urban	0.167	0.190	0.190
Artemis Rural	0.024	0.045	0.069
Artemis MW130	0.004	0.005	0.128
Chalmers-Sahlgrenska	0.115	0.137	0.20

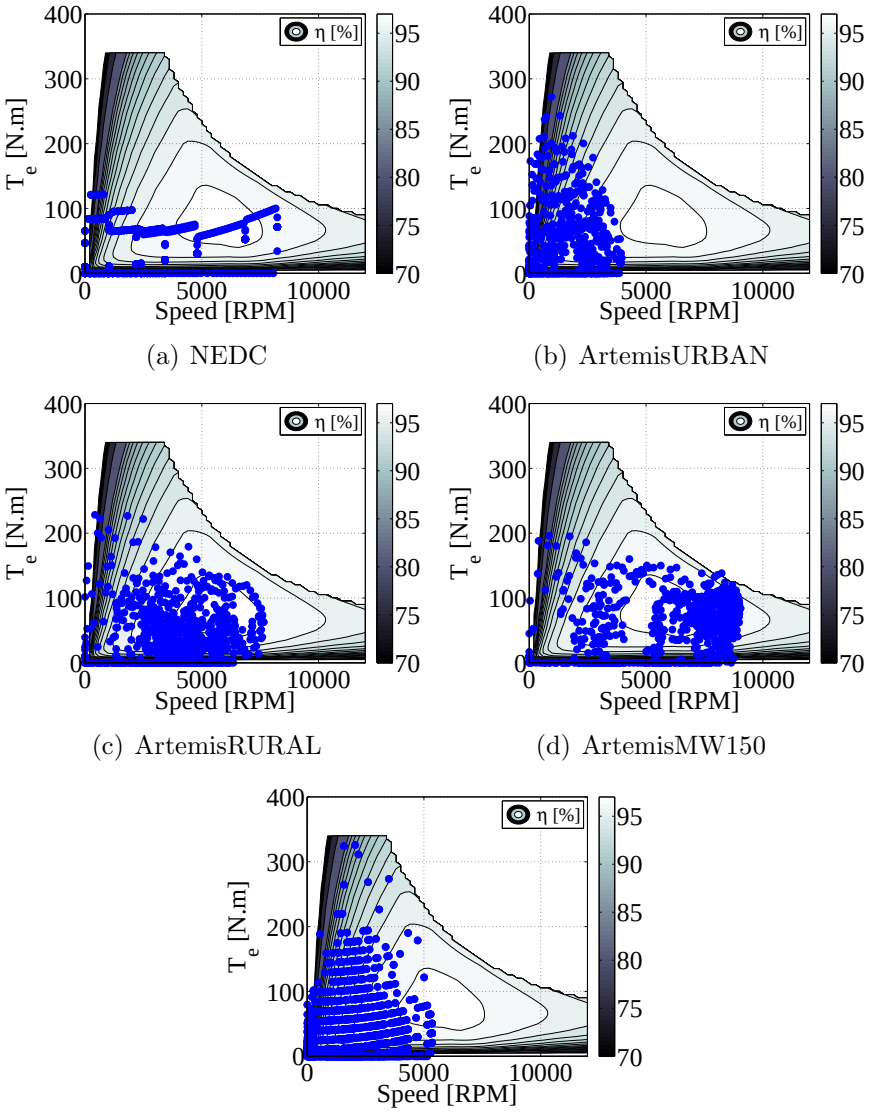

(a) NEDC

(b) ArtemisURBAN

(c) ArtemisRURAL

(d) ArtemisMW150

(e) Chalmers University - Sahlgrenska Hospital (round trip)

Figure 4.15: Demanded operating points of the drive cycles together with the efficiency map obtained from method III

It can be seen in Table 4.2, that the overall energy efficiency improvement is not huge and can be up to 0.2 %. However, all methods show an improvement in energy efficiency in urban driving condition where the high torque demand is more often required. The difference between these three methods is not substantial either. It can be seen that Method III using loss minimization

has some advantage in drive cycles with a high speed profile such as "Artemis MW130". However, the greatest impact of these control strategies as shown in Section 4.4 seems to be the performance improvement thorough the increase of the initial torque, expansion of the maximum allowed torque at low speeds and extension of maximum allowed torque by reducing the power loss to at a high initial torque.

Chapter 5

Energy efficiency evaluation of the electric drive-train in electric vehicles

In this chapter, the energy efficiency investigation has been extended from the electric drive in Chapter 4 to the propulsion inverter. Various inverter solutions such as using switching devices with new materials or higher reverse blocking voltage levels are evaluated for a vehicle propulsion inverter. Furthermore, the energy efficiency consequence of using a controllable dc-link for the propulsion inverter in order to minimize the total drive system losses is studied.

The drive cycle energy efficiency calculation, are based on the vehicle case setup explained in Section 4.7.1 and the electrical drive-train setup introduced in Section 5.1.

The scenarios to be investigated are

- Section 5.2 : Energy efficiency consequence of using a SiC diode as the freewheeling diode in an IGBT-based inverter
- Section 5.3 : Energy efficiency consequence of changing the dc-link voltage level from 400 V to 800 V
- Section 5.4 : Energy efficiency consequence of using a SiC MOSFET as the switching device in the inverter
- Section 5.5 : Energy efficiency consequence of overdimensioning the current ratings of the switching devices in the inverter
- Section 5.6 : Energy efficiency consequence of using a variable dc-link voltage for inverter

5.1 Electric drive-train setup

In this section, a case setup for the electric drive-train which consists of the electric machine, the propulsion inverter and the battery is selected.

5.1.1 Battery

A battery with the specifications given in Table 5.1 is used in this thesis.

Table 5.1: Battery Specification

Parameter	Value
Internal resistance (R_{bat})	0.2 Ω
Rated charge capacity (Q_{rated})	26 $A \cdot h$
Initial voltage	800 V
Initial SOC	90 %

Dynamic battery models are highly complex. The voltage source which is also known as Open Circuit Voltage (OCV) is a function of both temperature and SOC (State Of Charge), whereas the resistor is only a function of temperature. In this thesis, the electric model consists of a voltage source (OCV) and a resistance whereas the OCV is only dependent on the SOC [57]. Therefore, the output voltage of the battery (V_{bat}) in a certain dc-link current ($I_{dc-link}$) can be expressed as

$$V_{bat} = OCV + R_{bat} \cdot I_{dc-link}. \tag{5.1}$$

The SOC can be expressed as

$$\frac{dSOC}{dt} = k \cdot I_{dc-link}(t) \tag{5.2}$$

where

$$k = \frac{1}{Q_{rated} \cdot 3600}. \tag{5.3}$$

This model sufficiently represents the voltage variations in the dc-link which are needed for the here presented energy efficiency studies.

5.1.2 Electric Machines

For energy efficiency analysis of the propulsion inverter, the knowledge of the phase voltage, current and load angle required by the electric machine are required. Therefore, the electric machine which is presented introduced in Chapter 2 in two configurations of 400 V (Machine I) and 800 V (Machine II) are used to obtain the required output phase voltage and current for the inverter. The required voltage, current and power factor demanded by each machine depend on the control algorithm used to obtain the current references of the electric machine. Therefore, in this Chapter, the result obtained from the non-linear optimization explained in Section 4.6 is used as a reference case for inverter studies. The required phase voltage, current and power factor which have to be provided by the inverter for Machine I are illustrated in Fig. 5.1.

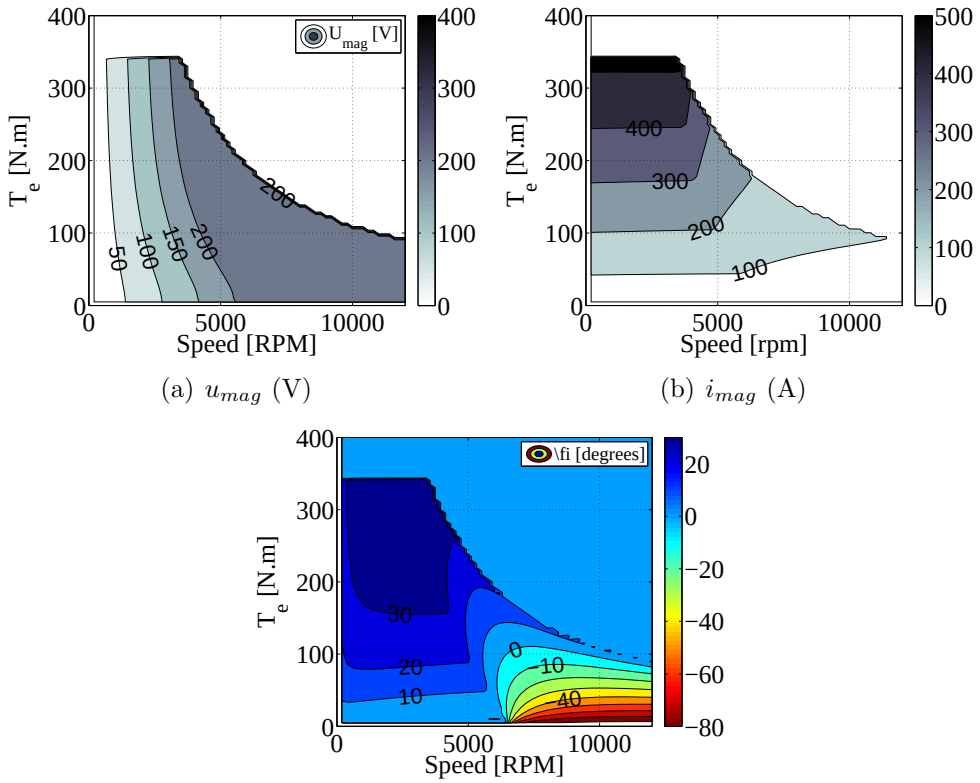

(a) u_{mag} (V)

(b) i_{mag} (A)

(c) ϕ (degree)

Figure 5.1: The required phase voltage, current and load angle requested by the machine controller

The corresponding power loss and efficiency map of the electric machine in these operating conditions are also shown in Fig. 5.2.

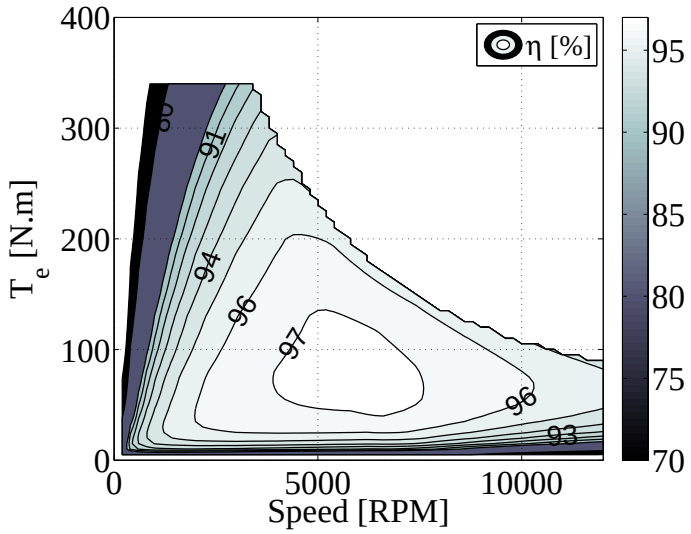

(a) The efficiency of the PMSM (%)

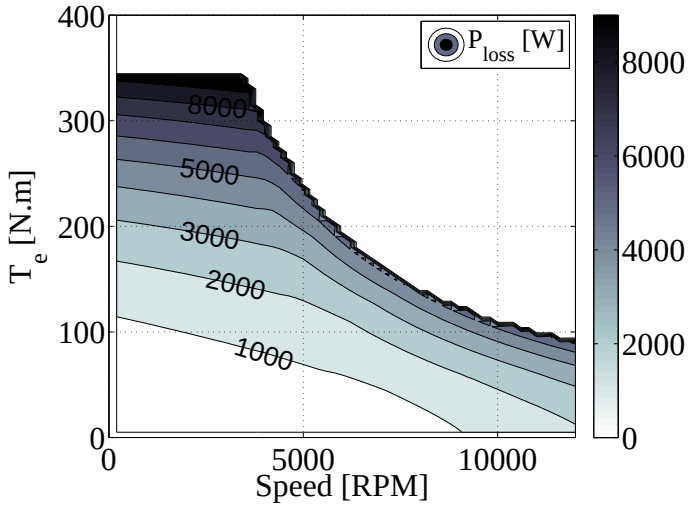

(b) Total power loss of the PMSM including the ohmic and iron losses (P_{loss}) (W)

Figure 5.2: Total power loss and efficiency map of the selected electric machine

5.1.3 Inverter

In this thesis, the dc-link voltage level of the electric system on the battery side is chosen to be either 400 V or 800 V. This corresponds to a suitable breakdown voltage level of either 650 V or 1200 V for the power electronic components, respectively. The safety margin of 250 V or 400 V is chosen mainly due to handle the switching overvoltages due to the parasitic inductances in the commutating circuit. The components which are used in the converter for different analysis are listed below.

- 650V Silicon IGBT Punch-Through (PT) (IXYK100N65C3D1) [58]
- 650V Silicon IGBT Non-Punch-Through (NPT) (IXYN100N65A3) [59]
- 650V Silicon pn diode (IXYX100N65C3D1) [60]
- 650V SiC MOSFET (SCT2120AF) [61]
- 650V SiC Schottky diode (C5D50065D) [62]
- 1200V Silicon IGBT Punch-Through (PT) (IXGK82N120A3) [63]
- 1200V Silicon IGBT Non-Punch-Through (NPT) (IXYH82N120C3) [64]
- 1200V Silicon pn diode (DHG60I1200HA) [65]
- 1200V SiC MOSFET (SCT2080KE) [46]
- 1200V SiC Schottky diode (C4D30120D) [53]

In order to obtain an identical power rating for all components, some components are assumed to be in parallel to reach the desired current rating. The current ratings are chosen based on the suggested current ratings given by the manufacturers for a case temperature of 100 $°C$ to 110 $°C$ for all components.

The components which are in parallel, are assumed to be in one module, disregarding the issues arising from the parallel connection of components for energy efficiency studies in this thesis. The name of these new modules consists of the name of the component they are made of, followed by a number and 'X'. This means for example that, MOSFET (SCT2080KE)12X, is one module which consists of 12 MOSFET (SCT2080KE) in parallel. Consequently, the forward characteristics such as the constant voltage drop and equivalent forward hesitance as well as the switching characteristics such as the switching

losses at a specific switching condition are presented in Tables 5.2 for the components with a breakdown voltage of 650 V and in Table 5.3 for components with a breakdown voltage of 1200 V.

Table 5.2: Characteristics of the components with the breakdown voltage of 650 V $@T_c = 100°C - 110°C$

Components	Forward Characteristics $@T_j = 150°C$	Switching Characteristics $@T_j = 150°C$
Si IGBT PT (IXYK100N65C3D1)6X	$V_{ce,0} = 1.25\ V$ $R_{on} = 2.2\ m\Omega$	$E_{on,pn\ diode} = 20.1\ mJ$ $E_{on,SiC\ diode} = 3.4\ mJ$ $E_{off} = 6.9\ mJ\ @V_{ce} = 400\ V, I_{ce} = 600\ A$
Si IGBT NPT (IXYN100N65A3)6X	$V_{ce,0} = 0.8\ V$ $R_{on} = 1.9\ m\Omega$	$E_{on,pn\ diode} = 21\ mJ$ $E_{on,SiC\ diode} = 4.6\ mJ$ $E_{off} = 14.4\ mJ\ @V_{ce} = 400\ V, I_{ce} = 600\ A$
SiC MOSFET (SCT2120AF)30X Body diode	$V_{ds,0} = 0\ V$ $R_{on} = 6\ m\Omega$ $V_{body,0} = 1\ V$ $R_{body} = 7.5\ m\Omega$	$E_{on,SiC\ diode} = 8.3\ mJ$ $E_{off} = 3.3\ mJ\ @V_{ds} = 300\ V, I_{ds} = 600\ A$
Si pn diode (IXYX100N65C3D1)6X	$V_{f,0} = 0.9\ V$ $R_{f,on} = 1.3\ m\Omega$	$E_{rr,di/dt=300A/\mu s} = 680\ \mu J$ $E_{rr,di/dt=750A/\mu s} = 1100\ \mu J\ @V_R = 400\ V$
SiC Schottky diode (C5D50065D)10X	$V_{f,0} = 0.8\ V$ $R_{f,on} = 2\ m\Omega$	$E_{rr,di/dt=500A/\mu s} = 36.6\ \mu J$ $@V_R = 400\ V$

The switching energy losses are calculated using the datasheet values for IGBTs and diodes with the method explained in Section 3.2.

For the SiC MOSFET (SCT2080KE) a series of experiments were presented in Section 3.4 to obtain the switching energy losses. These switching losses are close to the values given in the new datasheet [46].

Table 5.3: Characteristics of the components with the breakdown voltage of 1200 V @$T_c = 100°C - 110°C$ [46]

Components	Forward Characteristics @$T_j = 125 - 150°C$	Switching Characteristics @$T_j = 125°C$
Si IGBT PT (IXYH82N120C3)4X	$V_{ce,0} = 1.6\ V$ $R_{on} = 5.9\ m\Omega$	$E_{on,pn\ diode} = 101\ mJ$ $E_{on,SiC\ diode} = 44\ mJ$ $E_{off} = 14.8\ mJ$ @$V_{ce} = 600\ V, I_{ce} = 320\ A$
Si IGBT NPT (IXGK82N120A3)4X	$V_{ce,0} = 1\ V$ $R_{on} = 2.9\ m\Omega$	$E_{on,pn\ diode} = 98\ mJ$ $E_{on,SiC\ diode} = 41.5\ mJ$ $E_{off} = 90\ mJ$ @$V_{ce} = 600\ V, I_{ce} = 320\ A$
SiC MOSFET (SCT2080KE)12X Body diode	$V_{ds,0} = 0\ V$ $R_{on} = 12.3\ m\Omega$ $V_{body,0} = 1\ V$ $R_{body} = 20.8\ m\Omega$	$E_{on,SiC\ diode} = 27.4\ mJ$ $E_{off} = 3\ mJ$ @$V_{ds} = 600\ V, I_{ds} = 320\ A$
Si pn diode (DHG60I1200HA)6X	$V_{f,0} = 1.1\ V$ $R_{f,on} = 2.3\ m\Omega$	$E_{rr,di/dt=1200A/\mu s} = 6.3\ mJ$ @$V_R = 600\ V$
SiC Schottky diode (C4D30120D)6X	$V_{f,0} = 0.8\ V$ $R_{f,on} = 6.3\ m\Omega$	$E_{rr} = 93\ \mu J$ @$V_R = 600\ V$

5.2 Silicon Carbide Schottky freewheeling diode instead of a Silicon pn diode

Silicon Schottky diodes are known to have relatively lower losses than their pn counterparts thanks to the absence of a pn junction and high reverse recovery charge. Accordingly, at a higher breakdown voltage of 400 V or above, a SiC Schottky diode might be a possible alternative as a freewheeling diode. In this section the energy efficiency consequence of choosing such a diode instead of a Silicon pn diode is studied. The selected switching devices for the inverter are

- Setup A1: A 650 V PT IGBT module (XYK100N65C3D1) with a pn diode module (IXYX100N65C3D1) in a 400 V dc-link system

- Setup A2: A 650 V PT IGBT module (XYK100N65C3D1) with a SiC Schottky diode module (C5D50065D) in a 400 V dc-link system
- Setup A3: A 650 V NPT IGBT module (IXYN100N65A3) with a pn diode (IXYX100N65C3D1) in a 400 V dc-link system
- Setup A4: A 650 V NPT IGBT module (IXYN100N65A3) with a SiC Schottky diode module (C5D50065D) in a 400 V dc-link system

For each setup, the total losses of the inverter is evaluated when using the electric machine presented in Section 5.1.2 (Machine I). The conduction and switching losses for the inverter is calculated based on the equations found in Section 3.1 for the entire operating region of the electric motor.

The switching and the conduction losses for Setup A1 with the PT IGBT and pn diode is shown in Fig. 5.3 for the entire operating region of the motor and a switching frequency of 20 kHz.

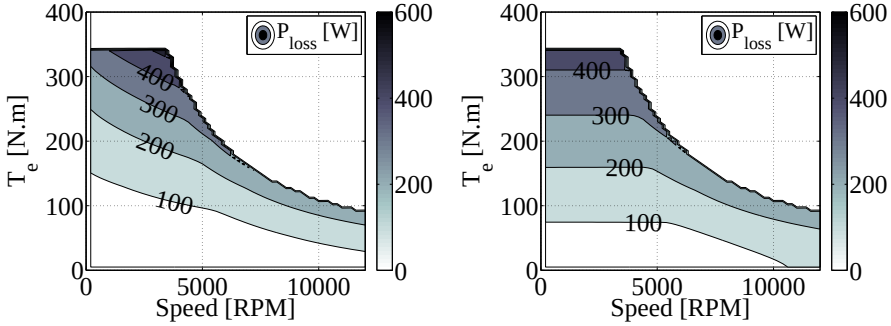

(a) Conduction loss of the switch (W) (b) Switching loss of the switch (W)

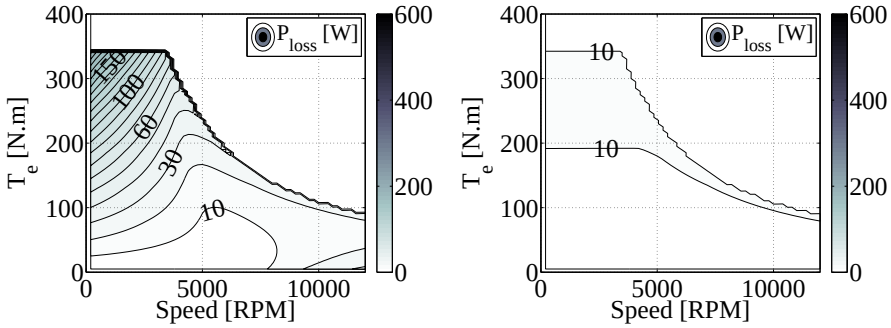

(c) Conduction loss of the freewheeling diode (W) (d) Switching loss of the freewheeling diode (W)

Figure 5.3: The conduction and the switching loss maps for a PT IGBT module with a pn Silicon freewheeling diode module (Setup A1) in the 400 V dc-link system.

By replacing the pn freewheeling diode in Setup A1 with a Schottky SiC diode Setup A1, turns into Setup A2. Therefore, the conduction and the switching losses of the IGBT and the diode for Setup A2 would change accordingly as it is illustrated in Fig. 5.4. The switching loss of the SiC freewheeling diode is too little to be shown in the scale of 10 W, therefore, Fig. 5.4 (d) is shown blank. The absence of a reverse recovery current affects the turn-on losses of the transistor, which can be seen in Fig. 5.4 (b).

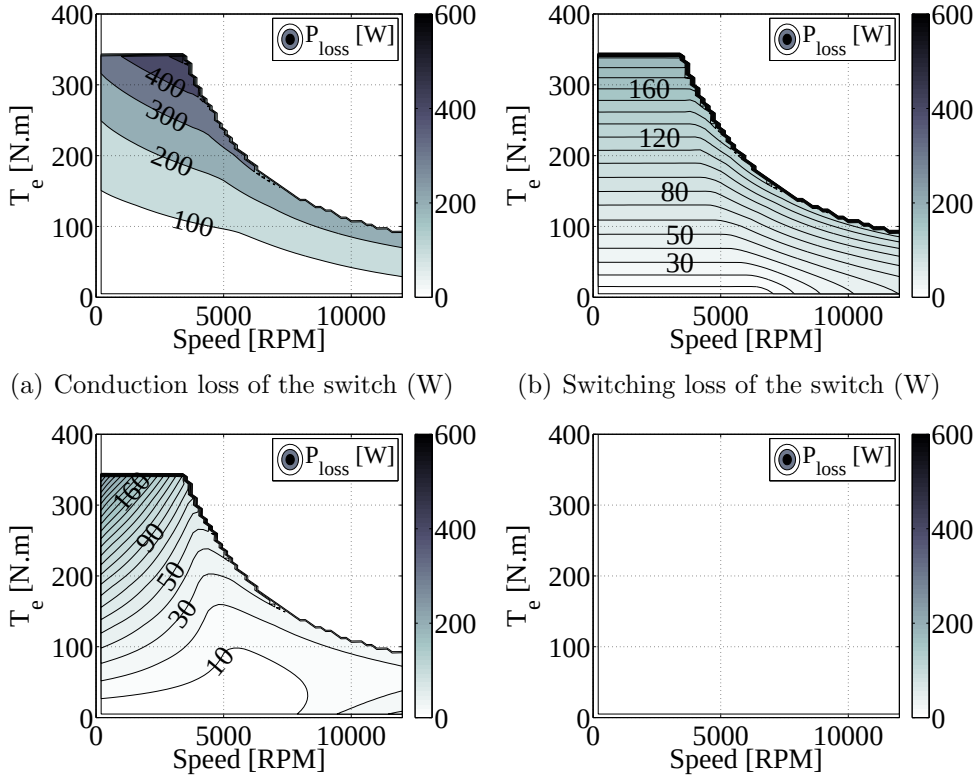

(a) Conduction loss of the switch (W)

(b) Switching loss of the switch (W)

(c) Conduction loss of the freewheeling diode (W)

(d) Switching loss of the freewheeling diode (W)

Figure 5.4: The conduction and the switching loss maps for a PT IGBT module with a SiC freewheeling diode module (Setup A2) in the 400 V dc-link system.

By changing the pn freewheeling diode in Setup A1 to a SiC Schottky diode in Setup A2, even the switching losses of the IGBT would change during the turn-on as it was shown in Section 3.2 for the calculation of the switching energy during the turn-on using (3.7). Therefore, to compare both setups, the total power loss including the conduction and the switching losses for both the

switches and diodes in each setup are now added, making up the total power loss of the inverter. The total power loss and efficiency map for each setup (Setup A2 and A1) are subtracted from each other and the results are shown in Fig. 5.5 for two frequencies of 20 kHz and 10 kHz. It can be seen that the setup with a SiC diode has reduced the switching losses in the entire operating region. This is mainly due to a significantly lower switching loss during the turn-on due to the use of the SiC diode.

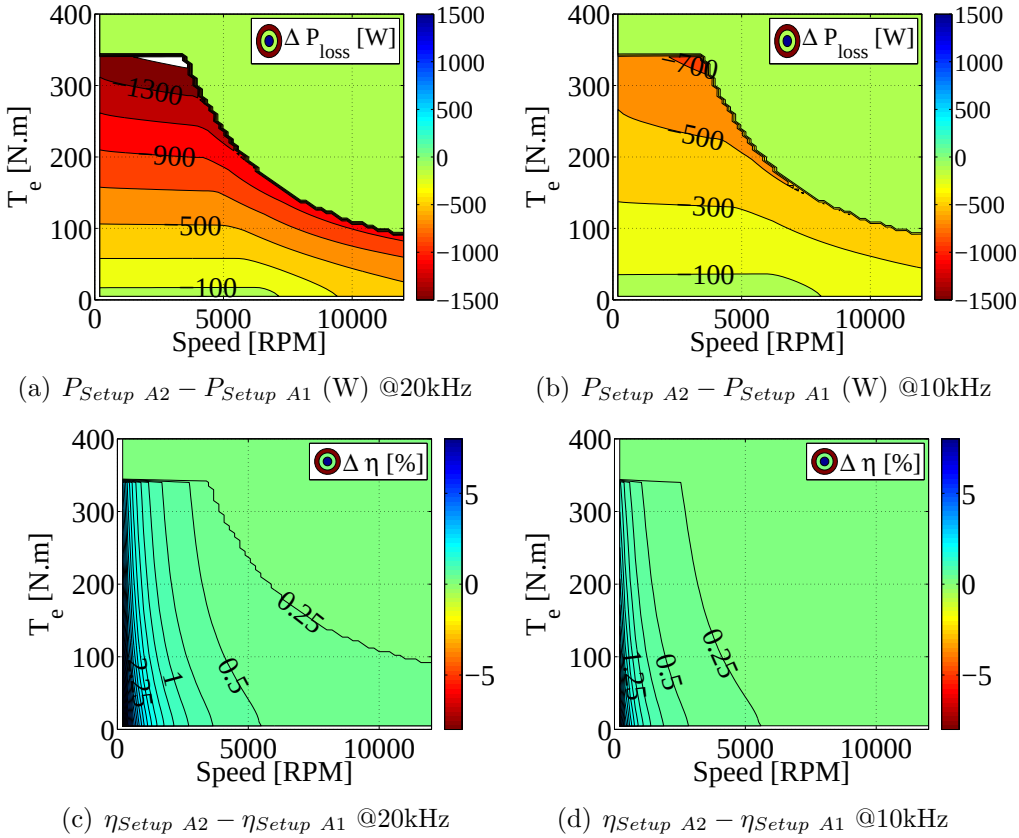

(a) $P_{Setup\ A2} - P_{Setup\ A1}$ (W) @20kHz

(b) $P_{Setup\ A2} - P_{Setup\ A1}$ (W) @10kHz

(c) $\eta_{Setup\ A2} - \eta_{Setup\ A1}$ @20kHz

(d) $\eta_{Setup\ A2} - \eta_{Setup\ A1}$ @10kHz

Figure 5.5: Total power loss of an inverter using a PT IGBT with a SiC Schottky diode module as freewheeling diode minus the total power loss of an inverter using the same IGBT with a pn freewheeling diode for two different switching frequencies.

Similarly, the switching and conduction losses for an NPT IGBT (Setup A3) are calculated and illustrated in Fig. 5.6. As expected, the NPT IGBT shows a lower conduction loss and higher switching loss at higher loads compared to the PT IGBT which is shown in Fig. 5.3.

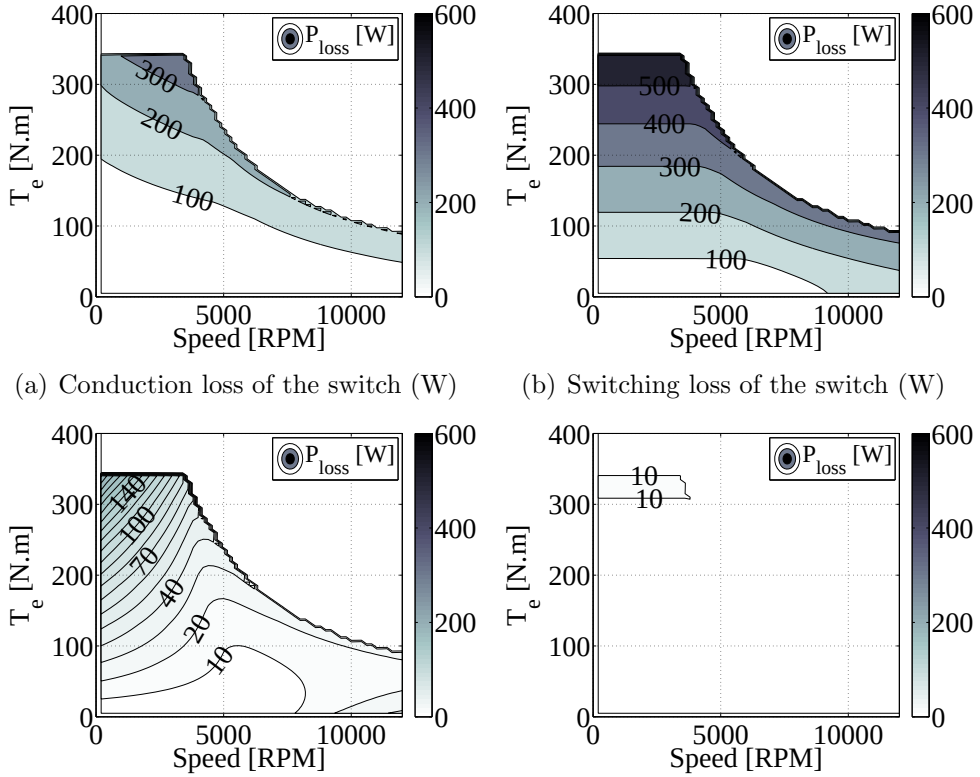

(a) Conduction loss of the switch (W)

(b) Switching loss of the switch (W)

(c) Conduction loss of the freewheeling (W)

(d) Switching loss of the freewheeling diode (W)

Figure 5.6: The conduction and the switching loss maps for an NPT IGBT module with a pn silicon freewheeling diode module (Setup A3).

By replacing the pn freewheeling diode in the NPT IGBT module (Setup A3) with a Schottky SiC diode, Setup A4 is created. That would decrease the switching losses of the switch and diode which are illustrated in Fig. 5.7.

The conduction and the switching losses for each setup are now added, making up the total power loss of the inverter. The total power loss and the corresponding efficiency losses for each setup (Setup A4 and A3) are subtracted from each other and the result is shown in Fig. 5.8.

As it is illustrated in Figs. 5.5 and 5.8, the total power loss is reduced for the setups with a SiC freewheeling diode in the entire operating region of the inverter with an efficiency increase of between 0.25 to 3 %. However, the energy efficiency improvement using this inverter in an electrified vehicle could also be of interest. Therefore, the energy efficiency of the inverter in various drive cycles and switching frequencies are also calculated.

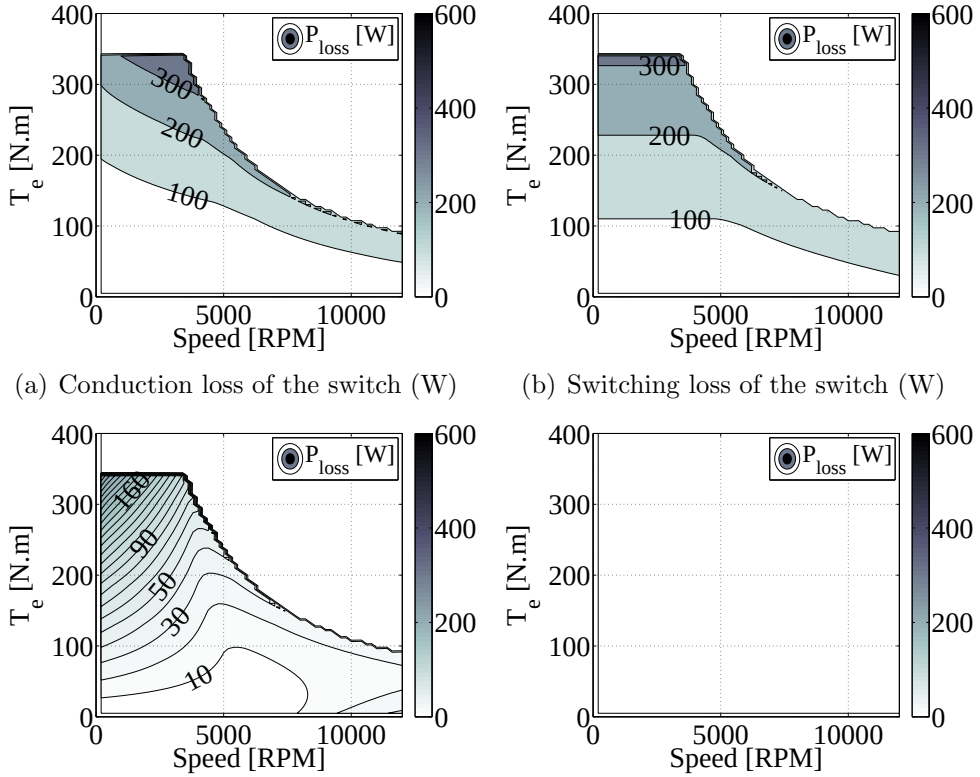

(a) Conduction loss of the switch (W)

(b) Switching loss of the switch (W)

(c) Conduction loss of the freewheeling (W)

(d) Switching loss of the freewheeling diode (W)

Figure 5.7: Conduction and switching loss maps for an NPT IGBT with a SiC freewheeling diode (Setup A4).

In Fig. 5.9, the converter efficiency for NEDC using the various setups explained earlier are compared with each other. As it can be seen, the higher the frequency the higher the impact of using the SiC freewheeling diode. However, at a low switching frequency of 5 kHz, the change of IGBT type from PT to NPT has the same effect as replacing the pn freewheeling diode to a SiC one.

Similarly, the energy efficiency is evaluated for other drive cycles and switching frequencies in Fig. 5.10 in order to see how the results are affected. The numerical results of the drive cycle efficiencies for the switching frequency of 20 kHz are presented in Table 5.4. It can be seen that an inverter with a pn freewheeling (Setup A1 and A3), can have an average of up to two percent improvement in the drive cycle efficiency by having a SiC freewheeling diode instead (Setup A2 and A4). The improvement is highest in the urban drive cycles such as "Chalmers-Sahlgrenska" and "Artemis Urban".

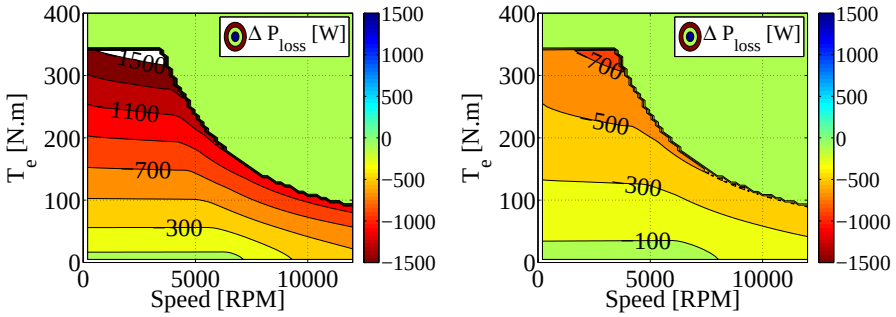

(a) $P_{Setup\ A4} - P_{Setup\ A3}$ (W) @20kHz (b) $P_{Setup\ A4} - P_{Setup\ A3}$ (W) @10kHz

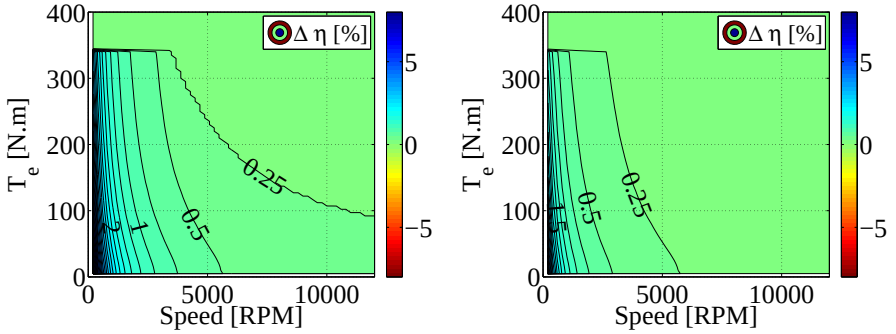

(c) $\eta_{Setup\ A4} - \eta_{Setup\ A3}$ @20kHz (d) $\eta_{Setup\ A4} - \eta_{Setup\ A3}$ @10kHz

Figure 5.8: Total power loss of an inverter using an NPT IGBT with a SiC Schottky diode module as freewheeling diode minus the total power loss of an inverter using the same IGBT with a pn freewheeling diode for two different switching frequencies.

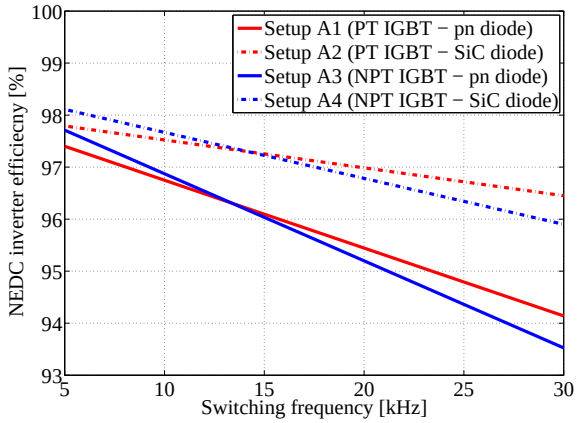

Figure 5.9: The converter efficiency for a NEDC drive cycle using the various semiconductor setups

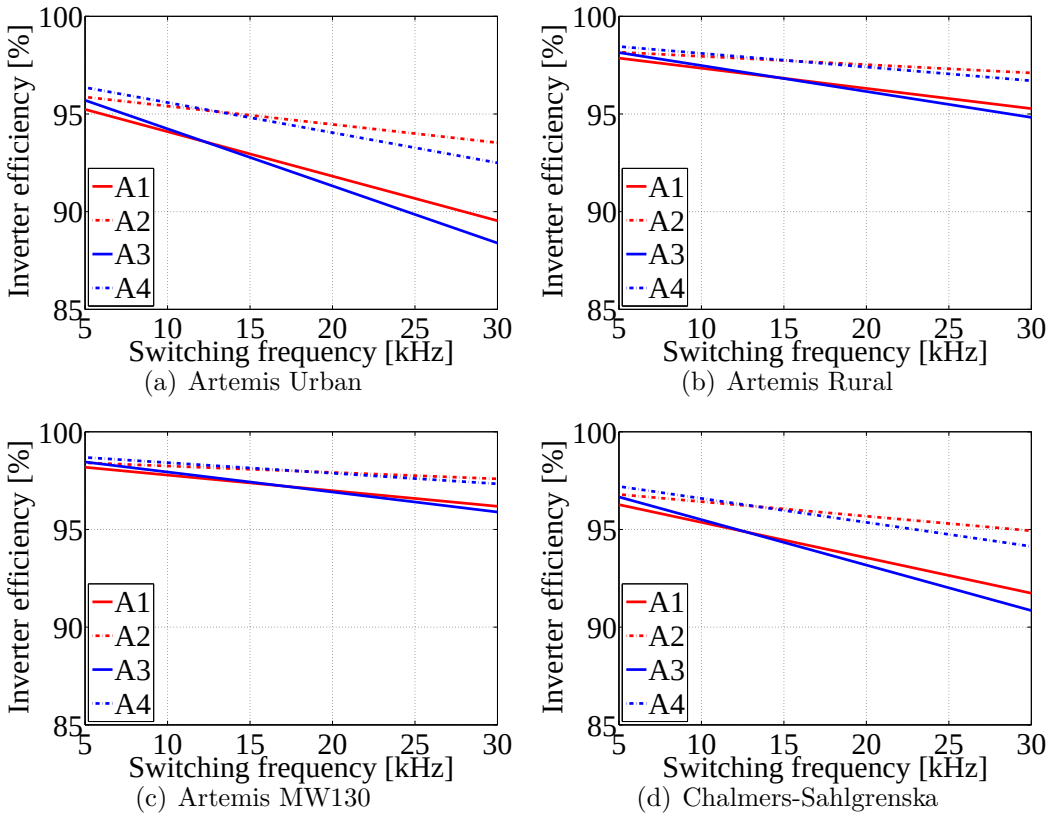

(a) Artemis Urban (b) Artemis Rural

(c) Artemis MW130 (d) Chalmers-Sahlgrenska

Figure 5.10: Drive cycle efficiency (energy losses of the inverter divided by the input power) for various inverter setups (Setups A1, A2, A3 and A4).

Table 5.4: Drive cycle efficiency (energy losses of the inverter divided by the input power) for various inverter setups and switching frequency of 20 kHz.

Drive cycle	Setup A1(%)	Setup A2 (%)	Setup A3 (%)	Setup A4 (%)
NEDC	95.4	97.0	95.2	96.8
Artemis Urban	91.8	94.5	91.3	94.0
Artemis Rural	96.3	97.5	96.1	97.4
Artemis MW130	97.0	97.9	96.9	97.9
Chalmers-Sahlgrenska	93.6	95.7	93.2	95.4

5.3 Change of the dc-link voltage level from 400 V to 800 V

In this section the effect of choosing a higher dc-link voltage on the propulsion inverter is investigated. Therefore, the components with the breakdown voltage of 650 V in a 400 V dc-link system in Section 5.2, are replaced with the components having a breakdown voltage of 1200 V which are suitable for a 800 V dc-link system.

The following two setups are selected to be compared with the similar two setups in Section 5.3.

- Setup B1: A 1200 V PT IGBT module (IXGK82N120A3) with a pn diode module (DHG60I1200HA) in a 800 V dc-link system

- Setup B2: A 1200 V PT IGBT module (IXGK82N120A3) with a SiC Schottky diode module (C4D30120D) in a 800 V dc-link system

First, Setup B1 and Setup A1 are selected to be compared. The conduction losses of the switch and the freewheeling diode for both setups are shown in Fig. 5.11. Similarly, the switching losses are shown in Fig. 5.12.

As it can be seen in Fig. 5.11, the conduction losses for both the switch and the freewheeling diode have decreased by an increase in the system voltage level from 400 V (Setup A1) to 800 V (Setup B1).

In contrast to the conduction losses, the switching losses which are shown in Fig. 5.12, are increased by an increase in the system voltage level.

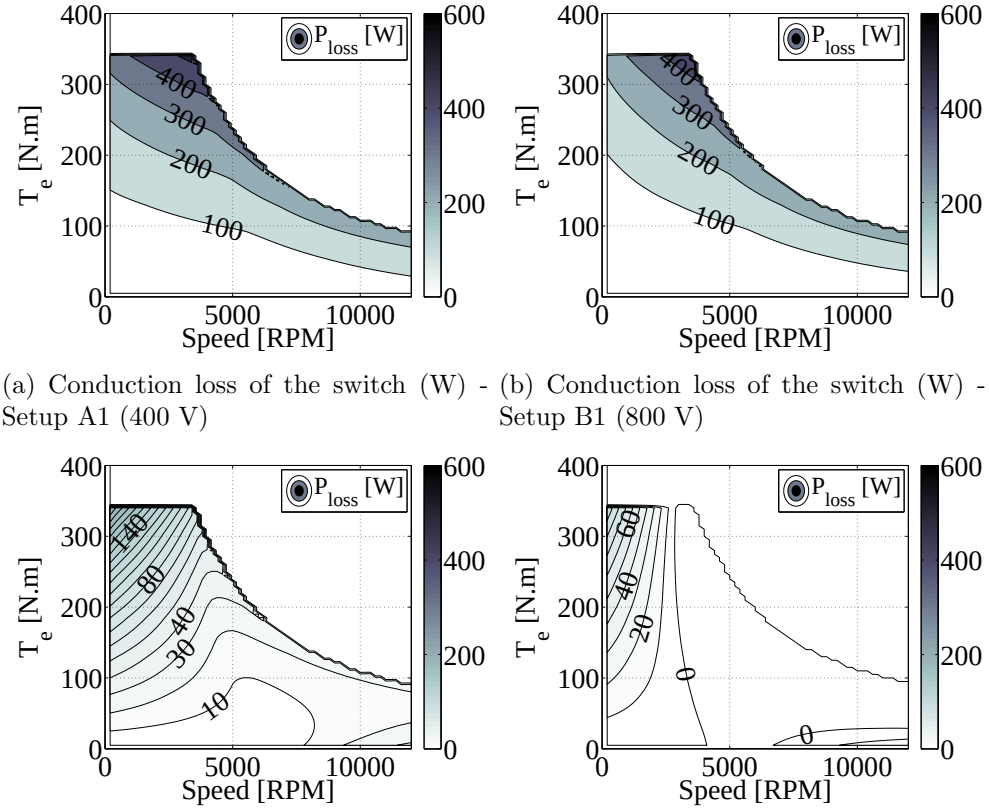

(a) Conduction loss of the switch (W) - Setup A1 (400 V)

(b) Conduction loss of the switch (W) - Setup B1 (800 V)

(c) Conduction loss of the freewheeling diode (W) - Setup A1 (400 V)

(d) Conduction loss of the freewheeling diode (W) - Setup B1 (800 V)

Figure 5.11: The conduction loss maps for a PT IGBT module with a pn freewheeling diode module (Setup A1) in the 400 V dc-link system and a similar module in the 800 V dc-link (Setup B1).

Since the conduction loss is decreased while the switching loss has decreased, the total power loss of the inverters needs to be compared to judge the impact of the system voltage level. In Fig. 5.13, it can be seen that the total power loss and the efficiency is generally unchanged by changing the system voltage level from 400 V to 800 V. The total power loss may be slightly reduced at very high loads by changing the voltage from 400 V to 800 V, however, the power loss slightly increases for the rest of the operating region.

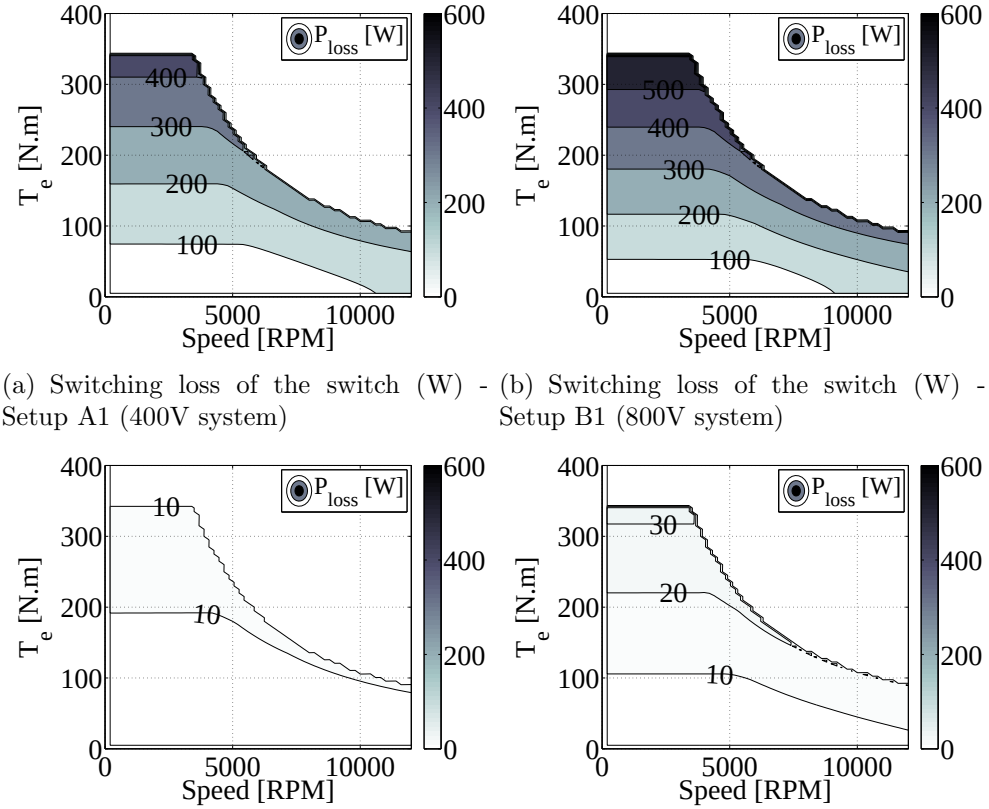

(a) Switching loss of the switch (W) - Setup A1 (400V system)

(b) Switching loss of the switch (W) - Setup B1 (800V system)

(c) Switching loss of the freewheeling diode (W) - Setup A1 (400V system)

(d) Switching loss of the freewheeling diode (W) - Setup B1 (800V system)

Figure 5.12: The switching loss maps for a PT IGBT module with a pn freewheeling diode (Setup A1) in the 400 V dc-link system and a similar module in the 800 V dc-link system (Setup B1).

Similar experiment is performed for Setup B2 which has the SiC freewheeling diode instead of the pn diode. In this case, two IGBT-based inverters with SiC freewheeling diodes, one in a 400 V system (Setup A2) and one in a 800 V (Setup B2) are compared with each other. As it can be seen in Fig. 5.14, increasing the voltage level has decreased the total losses. This is the opposite of results for the setup with a pn diode which is shown in 5.13. Therefore, it can be concluded that increasing the system voltage system which may worsen the IGBT-based inverters with the pn diodes, can actually improve the efficiency when the SiC freewheeling diodes are used.

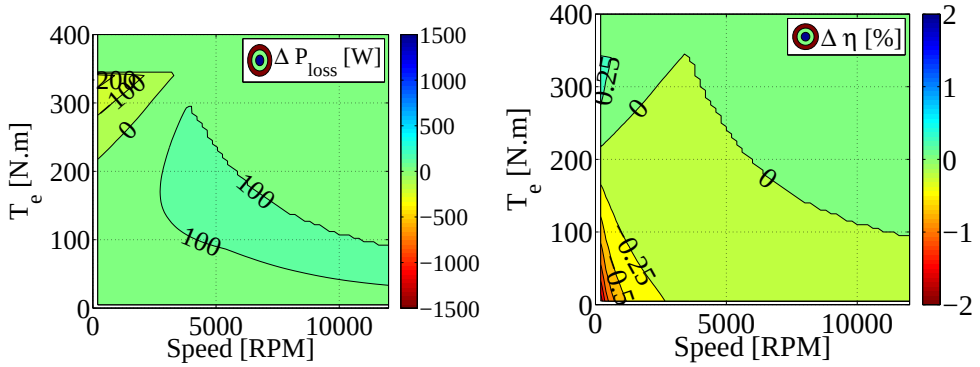

(a) $P_{Setup\ B1} - P_{Setup\ A1}$ (W) @20kHz (b) $\eta_{Setup\ B1} - \eta_{Setup\ A1}$ @20kHz

Figure 5.13: Total power loss and efficiency maps for the PT IGBT-based inverter with the pn freewheeling diode (Setup A1) in the 400V dc-link system and Setup B1 in the 800V dc-link.

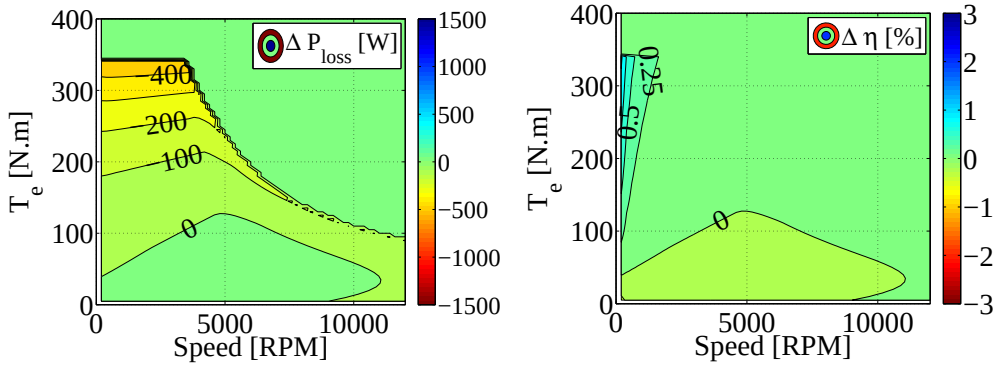

(a) $P_{Setup\ B2} - P_{Setup\ A2}$ (W) @20kHz (b) $\eta_{Setup\ B2} - \eta_{Setup\ A2}$ @20kHz

Figure 5.14: Total power loss and efficiency maps for the PT IGBT- based inverter with the SiC Schottky freewheeling diode module (Setup A2) in the 400 V dc-link system and Setup B2 in the 800 V dc-link system.

In Fig. 5.15 the converter efficiency for a NEDC drive cycle using the various setups explained in this section are compared with each other at various switching frequencies. As it can be seen in Fig. 5.15, increasing the voltage level (dotted lines) has mostly decreased the drive cycle efficiency for any switching frequency of 17 kHz and above.

Similarly, the energy efficiency of the other drive cycles are also calculated in various frequencies and shown in Fig. 5.16. The results for the switching frequency of 20 kHz is also written in Table 5.5.

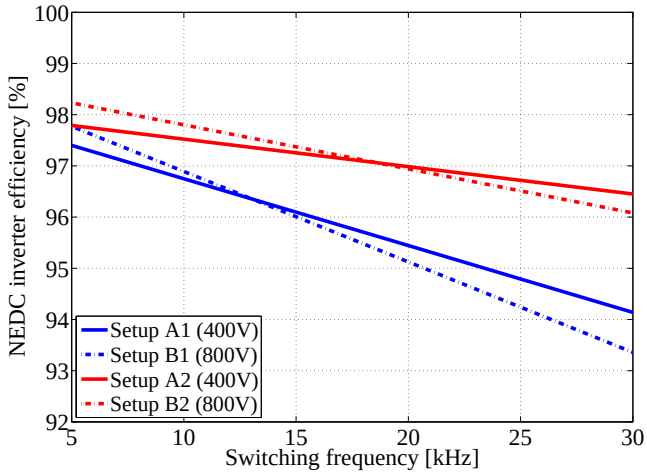

Figure 5.15: The converter efficiency for a NEDC drive cycle using the various semiconductor setups in systems levels of 400 V and 800 V.

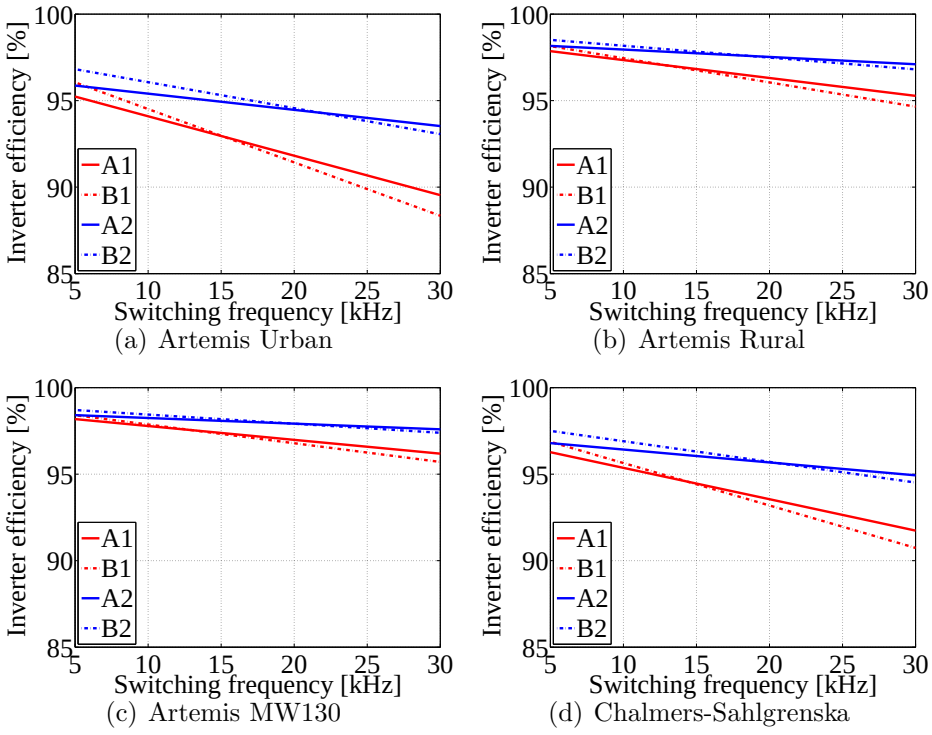

(a) Artemis Urban (b) Artemis Rural

(c) Artemis MW130 (d) Chalmers-Sahlgrenska

Figure 5.16: Drive cycle efficiency (energy losses of the inverter divided by the input power) for various inverter setups at 800 V with dotted lines (Setups B1 and B2) and 400 V with straight lines (Setups A1 and A2).

As it can be seen in Figs. 5.15 and 5.16, by increasing the voltage level, the drive cycle efficiency increases when the switching frequency is below 10 kHz. In contrast, the efficiency starts to decrease for the switching frequency of 20 kHz and above.

Table 5.5: Drive cycle efficiency (energy losses of the inverter divided by the input power) for various inverter setups and switching frequency of 20 kHz.

Drive cycle	Setup B1(%)	Setup B2 (%)
NEDC	95.1	96.9
Artemis Urban	91.4	94.6
Artemis Rural	96.0	97.5
Artemis MW130	96.8	97.9
Chalmers-Sahlgrenska	93.2	95.7

5.4 Use of a Silicon Carbide MOSFET as the main switching device

In this section the energy efficiency consequence of choosing a SiC MOSFET instead of an ordinary Silicon IGBT in a propulsion inverter is evaluated. The following setups are selected.

- Setup C1: A 650V SiC MOSFET module (SCT2120AF) with Schottky freewheeling diodes (C5D50065D)

- Setup C2: A 1200V SiC MOSFET module (SCT2080KE) with SiC Schottky freewheeling diodes (C4D30120D)

First, setup C1 is chosen and the conduction and the switching losses for the SiC MOSFET and the SiC Schottky diode modules used in this setup are shown in Fig. 5.17.

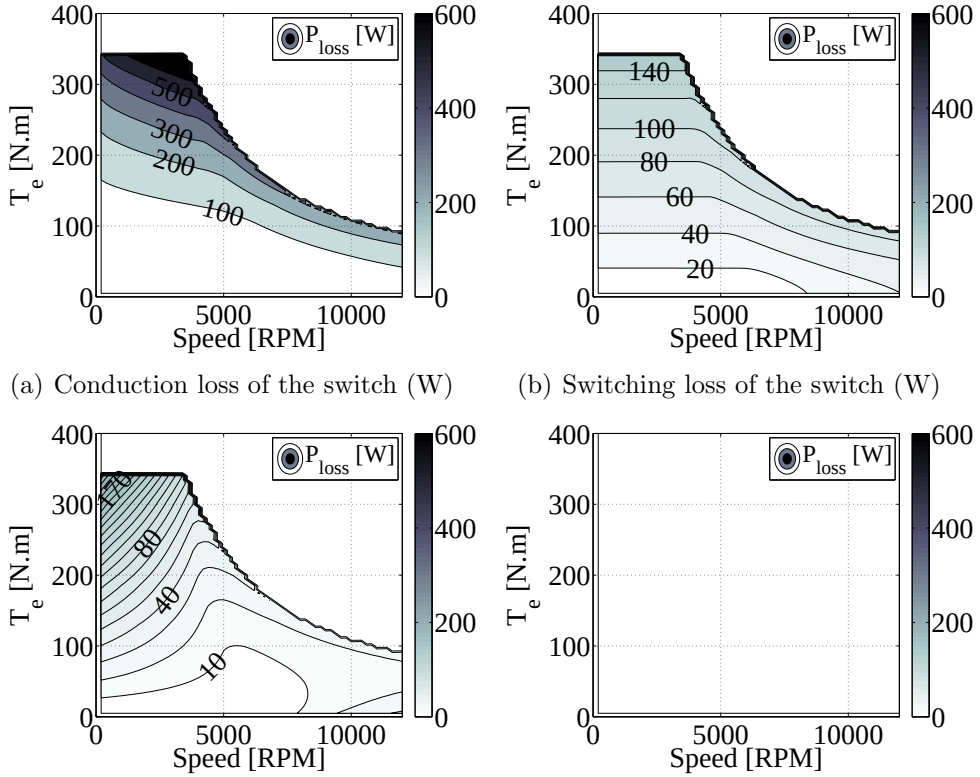

(a) Conduction loss of the switch (W)

(b) Switching loss of the switch (W)

(c) Conduction loss of the freewheeling diode (W)

(d) Switching loss of the freewheeling diode (W)

Figure 5.17: The conduction and the switching loss maps for a SiC MOSFET module with a SiC freewheeling diode (Setup C1) in the 400 V dc-link system.

The total inverter losses using this setup is compared with all IGBT setups with a breakdown voltage of 650 V (Setup A1, A2, A3 and A4 which are explained in Section 5.2) in Fig. 5.18 to understand the impact of using the SiC MOSFET instead of the IGBTs at this voltage level.

It can be seen that the power loss is always decreased when SiC MOSFETs are used instead of the IGBTs with a pn diode (Setup A1, A3), regardless of being a PT or an NPT IGBT. However, when the SiC freewheeling diode is used as freewheeling diode for the IGBTs (Setup A2, A4), the use of a SiC MOSFET is shown to be less beneficial. It can even increase the power losses at very high loads.

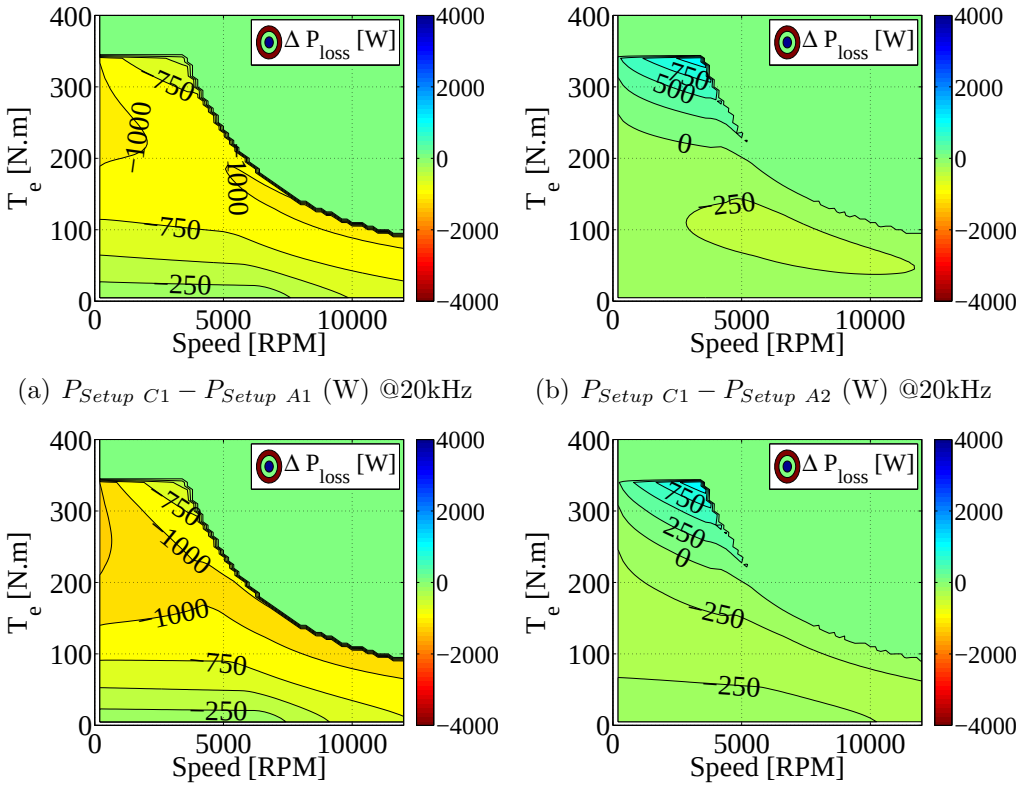

(a) $P_{Setup\ C1} - P_{Setup\ A1}$ (W) @20kHz

(b) $P_{Setup\ C1} - P_{Setup\ A2}$ (W) @20kHz

(c) $P_{Setup\ C1} - P_{Setup\ A3}$ (W) @20kHz

(d) $P_{Setup\ C1} - P_{Setup\ A4}$ (W) @20kHz

Figure 5.18: Total power loss of an inverter using the SiC MOSFET with the SiC Schottky diode as freewheeling diode (Setup C1) minus the total power loss of an inverter using the IGBTs (Setup A1) in the 400 V dc-link system.

A similar comparison is made for the components with a breakdown voltage of 1200 V. The SiC MOSFET with the breakdown voltage of 1200 V (Setup C2) is compared with the setups with IGBTs with a similar breakdown voltage (Setup B1, B2, B3 and B4). The result is shown in Fig. 5.19.

As it can be seen in Fig. 5.19, the use of the SiC MOSFET decreases the inverter power losses for the entire operating region. It can also be seen that the use of the SiC MOSFET at the 800 V system level, causes a greater power loss decrease compared with the case of a 400 V system.

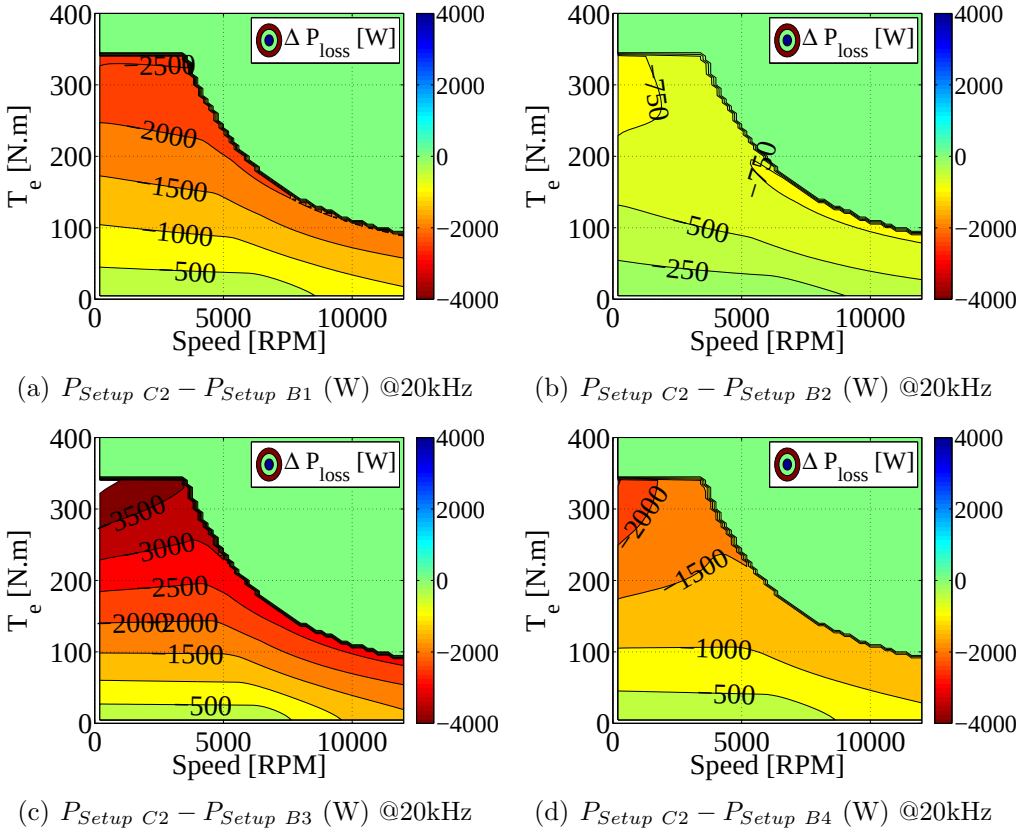

(a) $P_{Setup\ C2} - P_{Setup\ B1}$ (W) @20kHz (b) $P_{Setup\ C2} - P_{Setup\ B2}$ (W) @20kHz

(c) $P_{Setup\ C2} - P_{Setup\ B3}$ (W) @20kHz (d) $P_{Setup\ C2} - P_{Setup\ B4}$ (W) @20kHz

Figure 5.19: Total power loss of an inverter using the SiC MOSFET with the SiC Schottky diode as freewheeling diode (Setup C1) minus the total power loss of an inverter using the IGBTs (Setup A1) in the 400 V dc-link system.

In Fig. 5.20 the drive cycle efficiency of the inverter for the NEDC drive cycle using the SiC MOSFET is compared with other setups using IGBTs for various switching frequencies.

As it can be seen in Fig. 5.20, the SiC MOSFET provided a higher efficiency for the entire switching frequency range. At higher switching frequencies, the differences between the SiC MOSFET and the IGBT setups are more significant. Furthermore, by comparing Figs. 5.20 (a) and (b), it can be seen that the SiC MOSFET setup has a greater improvement at the higher system voltage level of 800 V compared to the 400 V system.

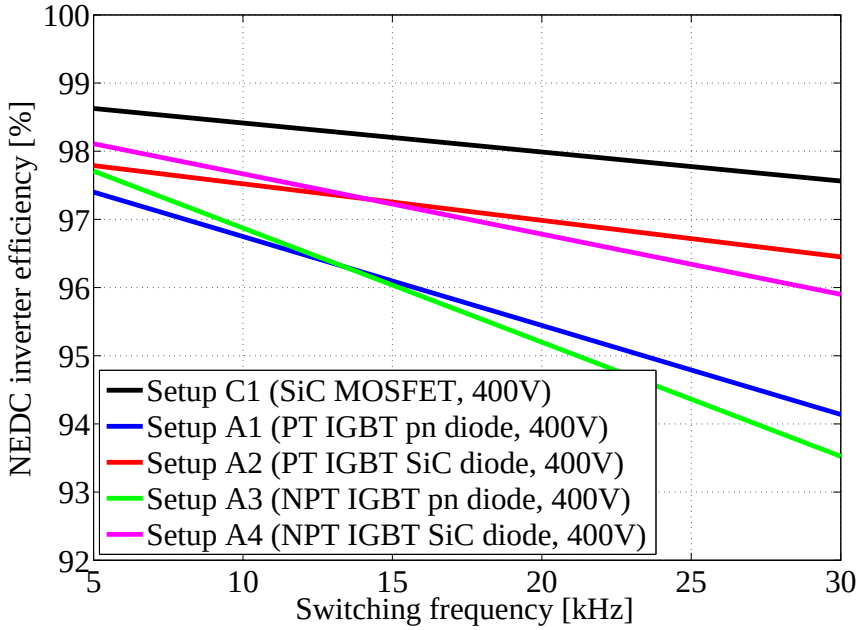

(a) 400 V system

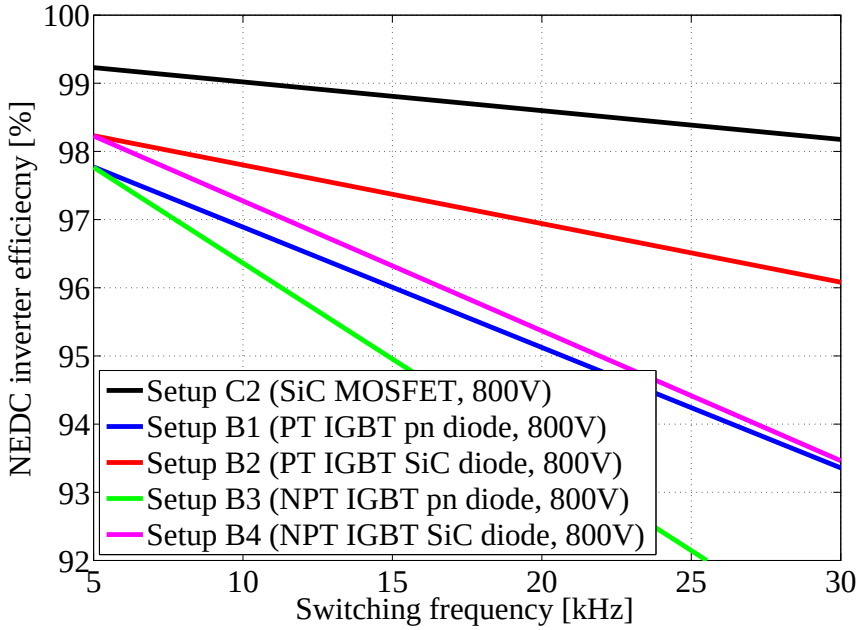

(b) 800 V system

Figure 5.20: The converter efficiency for a NEDC drive cycle using the SiC MOSFET instead of the IGBTs in systems levels of 400 V and 800 V.

Similarly, other drive cycles are used for the evaluation of the inverter efficiency using the SiC MOSFET instead of the IGBT setups and the results are shown in Fig. 5.21 and in Table 5.6. For each drive cycle, the energy efficiency improvement of using the SiC MOSFET instead of the IGBTs for the same voltage level is obtained by subtracting the drive cycle efficiency of these setups which are found in Table 5.4 and 5.5.

It can be seen that the use of a SiC MOSFET can increase the drive cycle efficiency from 0.4 % - 4.2 % for the 400 V system and 1 % - 8.4 % for the 800 V system depending on the drive cycle with a switching frequency of 20 kHz. It can also be seen that the impact of using the SiC MOSFET is higher at more urban driving drive cycles.

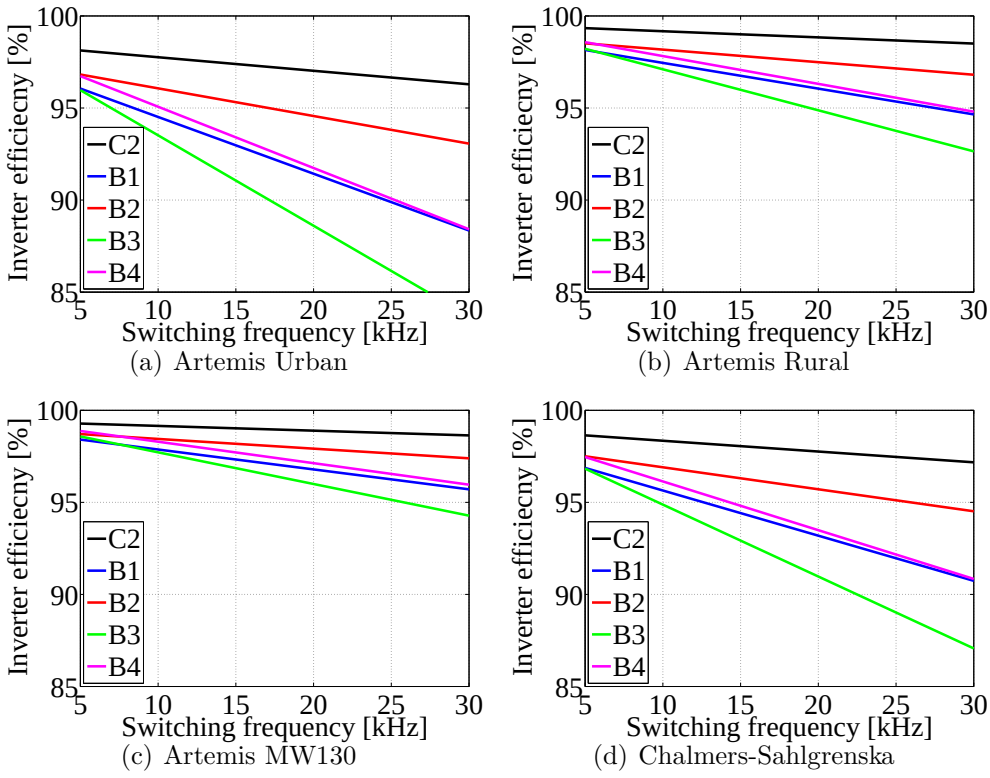

Figure 5.21: Drive cycle efficiency (energy losses of the inverter divided by the input power) for various inverter setups including the SiC MOSFET (Setup C2) at 800 V system.

Table 5.6: Drive cycle efficiency (energy losses of the inverter divided by the input power) for various inverter setups and switching frequency of 20 kHz.

Drive cycle	Setup C1 (%)	Improvement (%)	Setup C2 (%)	Improvement (%)
NEDC	97.9	2-2.7	98.6	1.7-5.1
Artemis Urban	95.5	1.4-4.2	97.0	2.4-8.4
Artemis Rural	98.3	0.9-2.2	98.8	1.3-3.9
Artemis MW130	98.3	0.4-1.4	98.9	1-2.9
Chalmers-Sahlgrenska	96.6	1.1-3.4	97.8	2.1-7.8

It should also be noted that a change from a silicon IGBT to a SiC MOSFET would require a significant change in the inverter design from the gate driver to the issues arising the higher voltage and current overshoots such as EMI problems.

5.5 Overdimensioning of the components in the inverter

Overdimensioning of the inverter components in this section, refers to the use of switching components with higher current ratings. In practice, this can be achieved by either choosing a higher rated components or putting several components in parallel. The aim is to reduce the on-state resistance of the components which reduces the conduction loss and eventually the total losses of the inverter. The best outcome would be to reduce the total losses so much that the need for a liquid cooling of the inverter is eliminated.

In Section 5.1.3, all ratings were selected based on the recommended component ratings for the case temperature of 110 °C. In this section, the previously used components are chosen to be overdimensioned by doubling the total current rating of inverter while the keeping the load (electric machine) unchanged. The aim is to evaluate the potential of increasing the inverter efficiency with the existing switching components.

First, the potential of IGBT- based inverters is evaluated. Therefore, the total power loss and the efficiency difference between the original setup and the new overdimensioned ones are illustrated in Figs. 5.22 and 5.23 for the components with breakdown voltages of 650 V and 1200 V respectively. It can be seen that the inverter efficiency is slightly improved between 0.25 % to 1 % regardless of the breakdown voltage level.

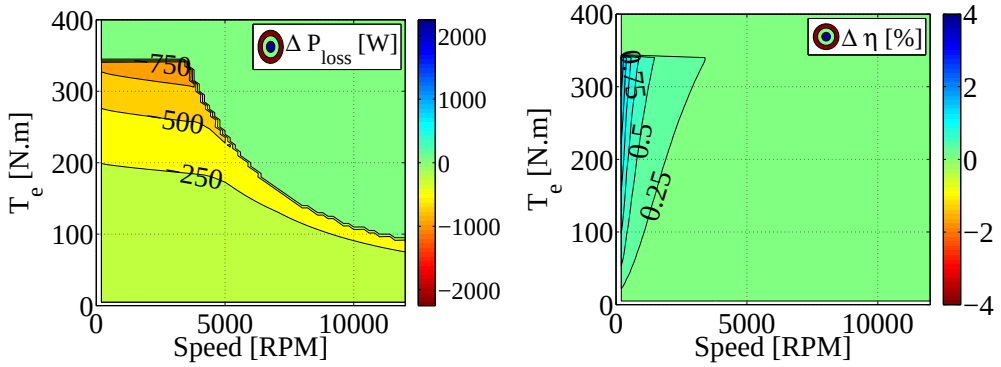

(a) $P_{Setup\ A1\ Overdimensioned} - P_{Setup\ A1}$ (W) @20kHz (b) $\eta_{Setup\ A1\ Overdimensioned} - \eta_{Setup\ A1}$ (W) @20kHz

Figure 5.22: Total power loss and the efficiency map of an inverter using the overdimensioned IGBTs in the 400 V system.

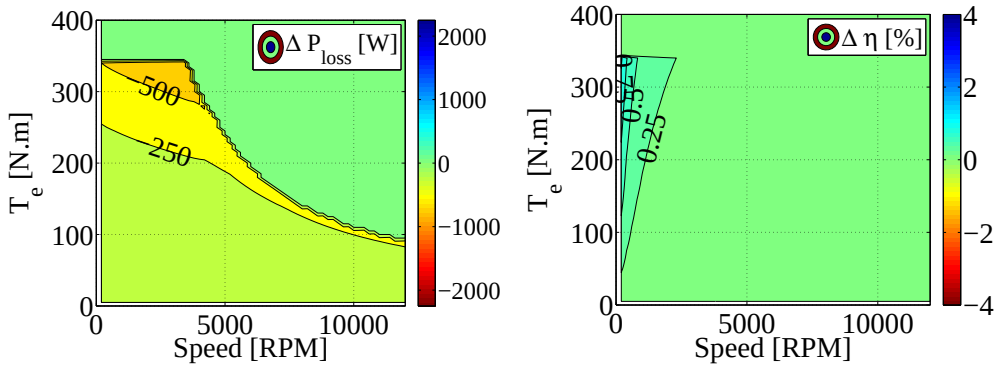

(a) $P_{Setup\ B1\ Overdimensioned} - P_{Setup\ B1}$ (W) @20kHz (b) $\eta_{Setup\ B1\ Overdimensioned} - \eta_{Setup\ B1}$ (W) @20kHz

Figure 5.23: Total power loss and the efficiency map of an inverter using the overdimensioned IGBTs in the 400 V system.

Similar experiment is performed for the inverters using the SiC MOSFETs (Setup C1 and C2). The current ratings of the SiC MOSFET inverters have been doubled and the power losses and the inverter efficiencies are compared with the original setups. As it can be seen in Figs. 5.24 and 5.25, the overdimensioned SiC MOSFET-based inverters have an efficiency improvement of up to 4%.

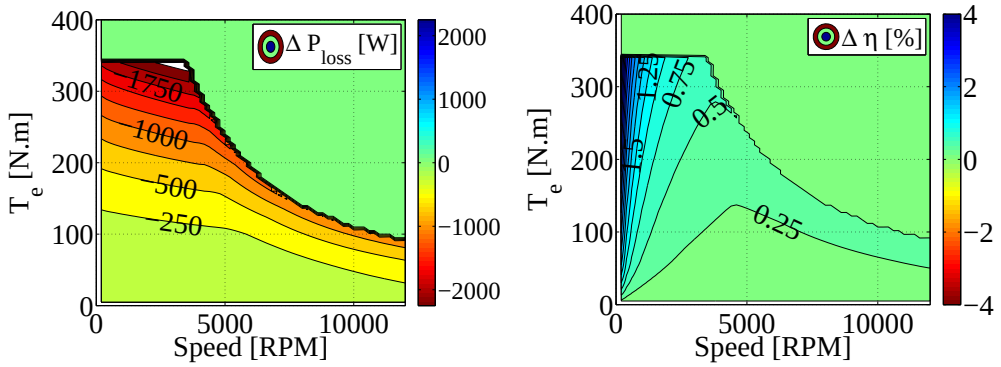

(a) $P_{Setup\ C1\ Overdimensioned} - P_{Setup\ C1}$ (W) @20kHz (b) $\eta_{Setup\ C1\ Overdimensioned} - \eta_{Setup\ C1}$ (W) @20kHz

Figure 5.24: Total power loss and the efficiency map of an inverter using the overdimensioned SiC MOSFETs in the 400 V system.

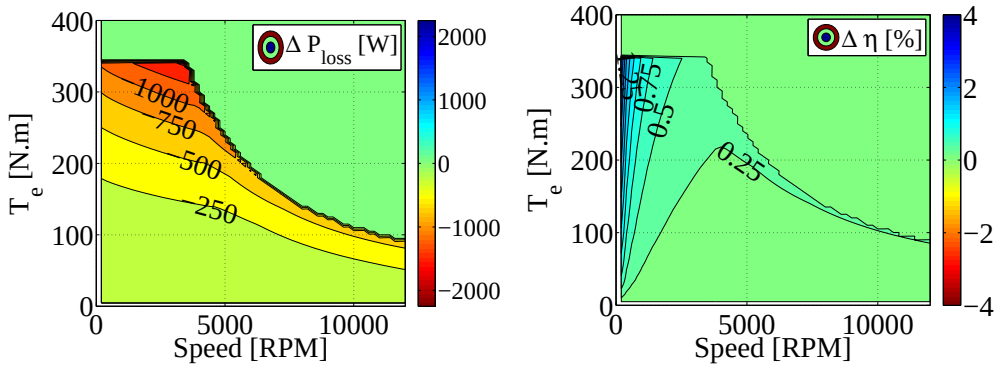

(a) $P_{Setup\ C2\ Overdimensioned} - P_{Setup\ C2}$ (W) @20kHz (b) $\eta_{Setup\ C2\ Overdimensioned} - \eta_{Setup\ C2}$ (W) @20kHz

Figure 5.25: Total power loss and the efficiency map of an inverter using the overdimensioned SiC MOSFETs in the 800 V system.

The main impact of overdimensioning, however, should be evaluated through the drive cycle efficiencies. Therefore, the drive cycle efficiency for the overdimensioned IGBTs and MOSFETs in various switching frequencies are shown in Fig. 5.26 for the NEDC drive cycle. As it can be seen in Fig. 5.26, the IGBT-based inverters have shown very little improvement in the drive cycle efficiency (around 0.1 %) whereas the SiC MOSFET-based inverters have experienced a slightly bigger impact (around 0.3 %).

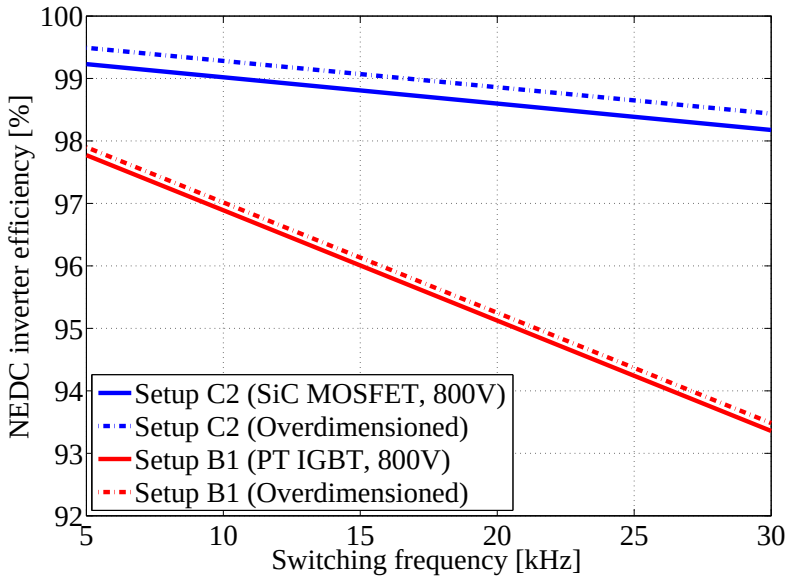

Figure 5.26: The converter efficiency for a NEDC drive cycle using the inverter with the overdimensioned SiC MOSFETs (Setup C2) and the overdimentioned IGBTs (Setup B1).

The energy efficiency for other drive cycles are also shown in Fig. 5.27 for various switching frequencies and numerically in Table. 5.7 for the switching frequency of 20 kHz. The drive cycle efficiency is improved in more demanding drive cycles such as Urban Artemis, however, the efficiency improvement remained below 0.6 %.

Table 5.7: Drive cycle efficiency (energy losses of the inverter divided by the input power) for a 800 V inverter system using the SiC MOSFET (Setup C2) or IGBT(Setup B1) versus a system with the overdimensioned component ratings (switching frequency of 20 kHz).

Drive cycle	Setup C2(%)	Over-dimensioned(%)	Setup B1(%)	Over-dimensioned(%)
NEDC	98.6	98.9	95.1	95.2
Artemis Urban	97.0	97.6	91.4	91.7
Artemis Rural	98.8	99.1	96.0	96.2
Artemis MW130	98.9	99.2	96.8	97.0
Chalmers-Sahlgrenska	97.8	98.2	93.2	93.4

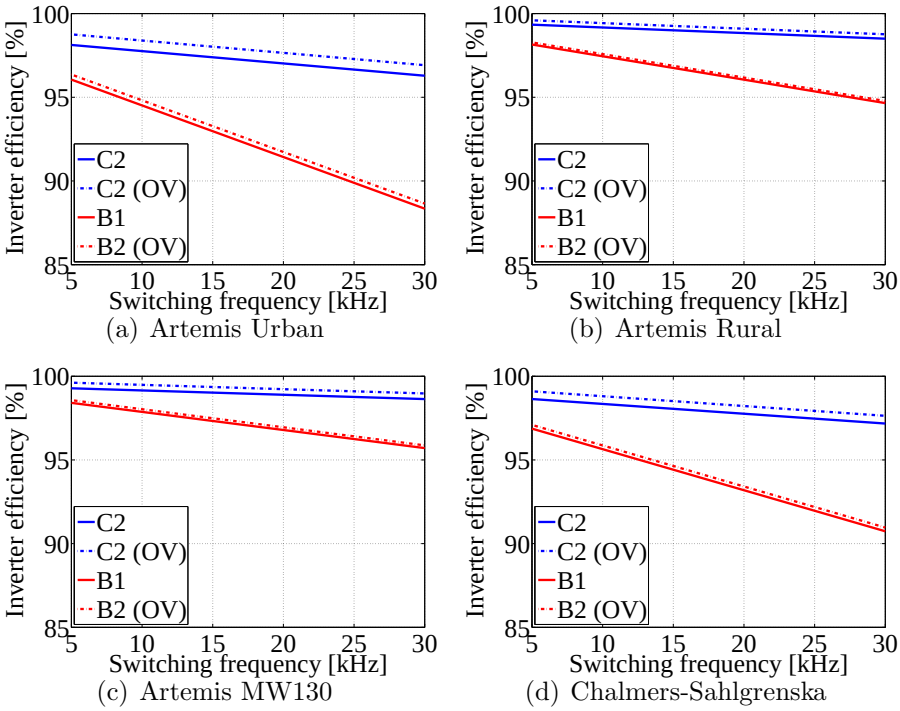

(a) Artemis Urban (b) Artemis Rural

(c) Artemis MW130 (d) Chalmers-Sahlgrenska

Figure 5.27: Drive cycle efficiency (energy losses of the inverter divided by the input power) for various inverter setups with the ordinary component sizing and the overdimensioned ones (OV).

5.6 System level efficiency analysis in a propulsion inverter with a controllable dc-link voltage

In the previous sections the dc-link voltage of the inverter was strictly constant and was chosen in accordance with the maximum allowed blocking voltage of the components at either 400 V or 800 V for components with breakdown voltage of 650 V and 1200 V respectively.

In an electric vehicle, the inverter is fed by a battery and the battery has naturally a variable output voltage. This would lead to a different loss model for the inverter which is investigated in previous sections.

A variable dc-link voltage can also be forced in the electric drive-train of the vehicle. This can be achieved by adding a DC-DC converter between the battery and inverter so that the dc-link of the inverter can be decreased or

increased according to the needs. The dc-link inverter might be increased to increase the voltage input of the electric machine. This results in an increase in the output power of the machine for a limited time. The dc-link inverter might be decreased to reduce the voltage dependently losses in the inverter.

In this section, first the naturally varying dc-link voltage caused by the battery is presented. Thereafter, the possibility of minimizing the total motor and inverter loss by having a controllable variable dc-link voltage is also explored.

5.6.1 A drive-train system with an uncontrolled and naturally varying dc-link voltage

The naturally varying dc-link voltage caused by the battery, change the inverter efficiency which thus impact the drive cycle efficiency. In this section, the inverter losses and also the battery and electric machine losses are evaluated. The efficiency results would be a reference point to compare with the efficiency of a drive-train where the dc-link voltage is controlled through a DC-DC converter.

Since the impact of the voltage variation could be different between the MOSFET- and IGBT-based inverters, two inverter setups are chosen. Setup C2 with the SiC MOSFET in Section 5.4 and Setup B1 in Section 5.3 for the IGBT-based inverter.

In order to simulate the variations in the battery voltage, the NEDC drive cycle is run for 5 times so the battery is discharged from a 90% initial value, to a 30% value. The current and voltage of the battery as well as the SOC are shown in Fig. 5.28. The resulting instantaneous efficiency of the components for one drive cycle is shown in Fig. 5.29.

All operating points during the entire drive cycle can be found in the full loss map shown in Fig. 5.30. As it can be seen, all operating points of the drive cycles are located between the layers of 800 V and 700 V where the battery voltage fluctuates.

5.6.2 A drive-train system with a controlled and variable dc-link voltage

In this section the dc-link voltage is assumed to be controlled regardless of the battery voltage. In each drive cycle and each operating point of the vehicle, the dc-link voltage which minimizes the total inverter and machine loss is chosen.

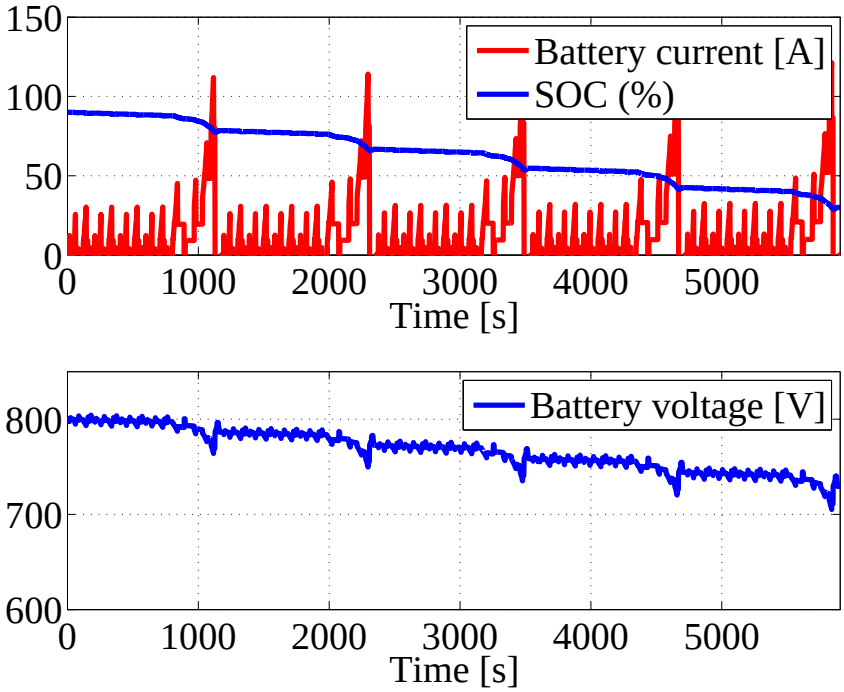

Figure 5.28: The battery current and voltage, and SOC during 5 consequent NEDC drive cycles.

The resulting instantaneous efficiency of the components for one drive cycle is shown in Fig. 5.31.

All operating points during the entire drive cycle can be found in the full loss map shown in Fig. 5.32. As it can be seen, all operating points of the drive cycles are located between the layers of 100 V and 800 V.

The drive cycle efficiency of all components using the controlled dc-link voltage and the naturally varying dc-link are compared with each other in Table 5.8 for the NEDC and an IGBT-based (Setup B1) and MOSFET-based (Setup C2) inverters.

As it can be see in Table 5.8 and 5.9, having a controllable variable dc-link voltage can improve the total efficiency of the electric drive system. This can be achieved by having a DC/DC converter between the battery and the propulsion inverter. In the SiC MOSFET-based inverter the drive cycle efficiency is improved up to 1 percent whereas in the IGBT-based inverter, the efficiency is improved up to 4 percent. This indicates that this controllable variable dc-link method has a more pronounced impact on the silicon IGBT based inverters. This is mainly due to the fact that a variable dc-link would

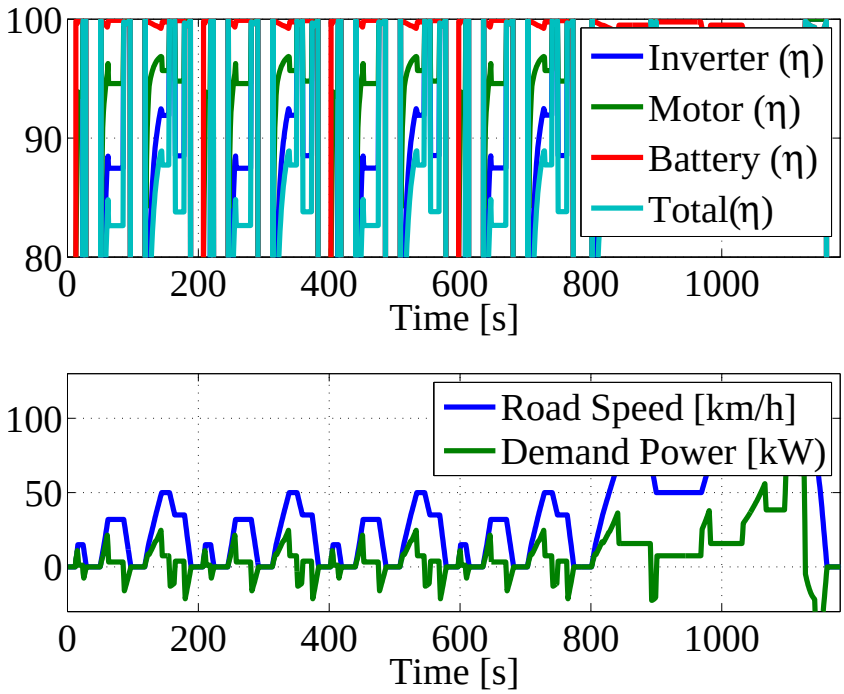

Figure 5.29: The instantaneous efficiency of different components in the drive-train in one NEDC drive cycle.

benefit by decreasing the switching losses. On the other hand a DC/DC converter itself has some losses so the efficiency improvement should be at least as much as the loss introduced by the DC/DC converter. As a result, a SiC based inverter with a controllable dc-link system cannot improve the total system efficiency. However, for an IGBT based inverter, if the efficiency of the additional DC/DC converter is high enough, this controllable dc-link system can improve the total electric system efficiency.

A benefit with this type of system is that the maximum power level of the machine can be maintained high by increasing the dc-link voltage when when the battery voltage drops.

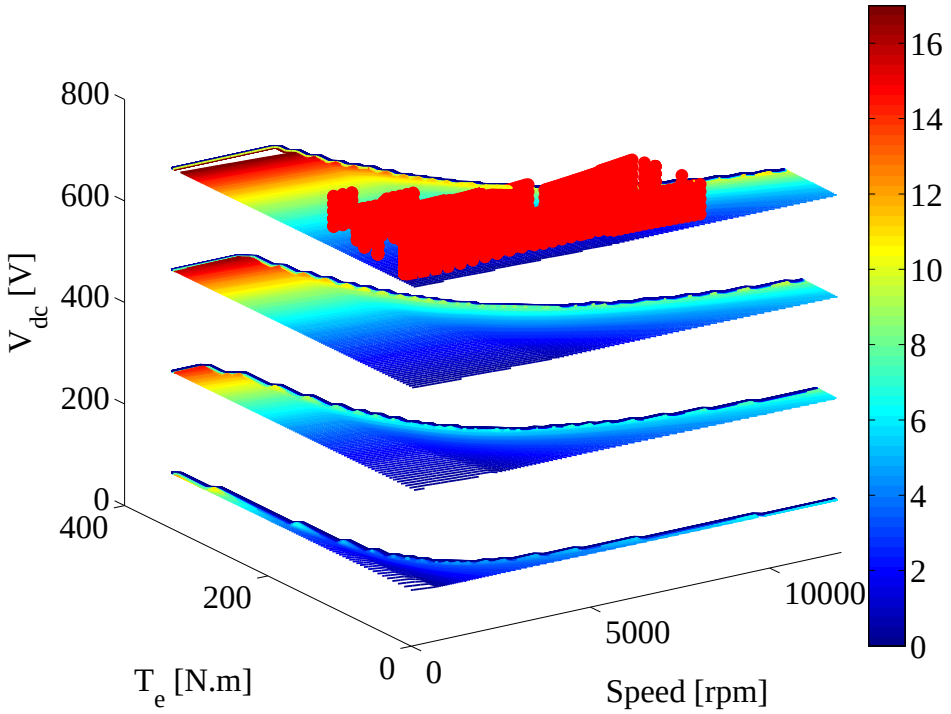

Figure 5.30: Total power loss of the electric machines in Torque - Speed - V_{dc} 3D map together with the battery voltage trajectories for 5 consequent NEDC drive cycles.

Table 5.8: Drive-train efficiency for NEDC drive cycle using the controlled dc-link voltage for two selected IGBT-based and SiC MOSFET-based inverters.

Drive cycle	Total efficiency(%)	Inverter(%)	Motor(%)	Battery(%)
EUDC(6x)	89.26	96.17	94.53	99.30
IGBT Uncontrolled	86.61	91.87	96.06	98.67
IGBT Controlled	89.33	94.48	96.16	98.68
MOSFET Uncontrolled	92.49	97.72	96.06	98.70
MOSFET Controlled	93.29	89.40	96.17	98.71

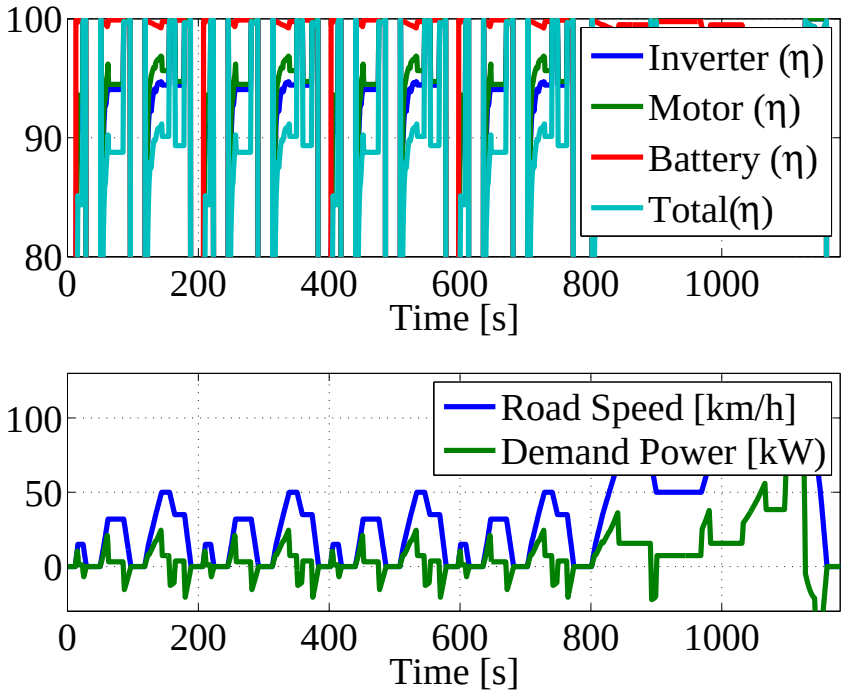

Figure 5.31: Instantaneous efficiency of different components for one NEDC drive cycle with the controlled dc-link voltage.

Table 5.9: Drive-train efficiency for Chalmers-Sahgrenska drive cycle using the controlled dc-link voltage for two selected IGBT-based and SiC MOSFET-based inverters.

Drive cycle	Total efficiency(%)	Inverter(%)	Motor(%)	Battery(%)
IGBT Uncontrolled	82.47	88.86	95.07	98.54
IGBT Controlled	87.18	93.57	95.00	98.60
MOSFET Uncontrolled	90.34	96.67	95.07	98.60
MOSFET Controlled	91.51	97.83	95.05	98.62

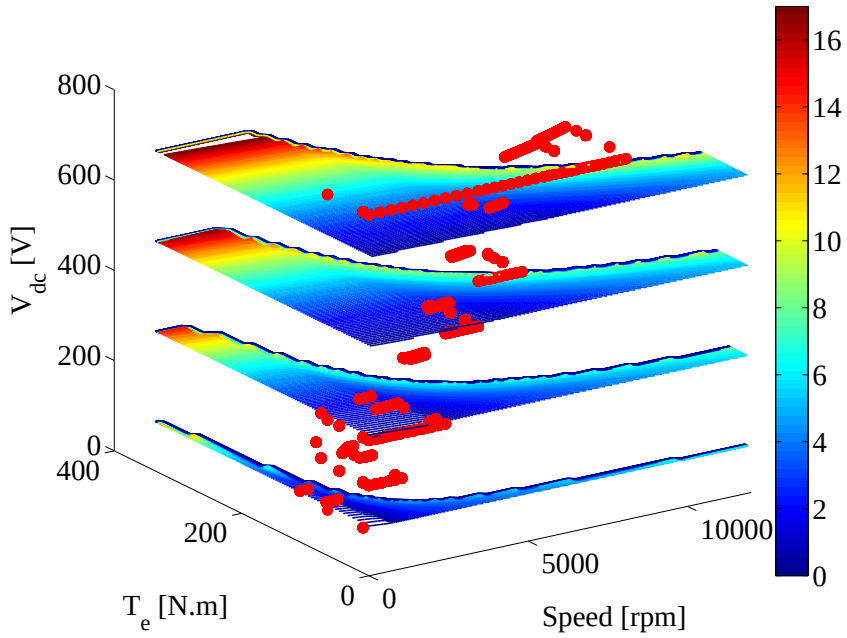

Figure 5.32: Total power loss of the electric machines in Torque - Speed - V_{dc} together with the voltage trajectories chosen for 5 consequent NEDC drive cycles to minimize the total losses.

Chapter 6

Conclusions and Future Work

6.1 Conclusions

By improving the control strategy in a selected PMSM, the low-speed and standstill torque characteristics of a PMSM could be improved by 7 % when using a proposed MTPA instead of an ordinary MTPA algorithm where the machine parameters (L_d, L_q and Ψ_m) are updated online outside the optimization algorithm. Furthermore, the efficiency can also be improved up to 5 % at low speed and high torques. However, the overall energy efficiency improvement for a certain drive cycle is not substantial, and can only reach 0.2 %.

Switching losses in the inverters can be reduced by decreasing the gate resistance. However, this leads to a higher turn-off overvoltage. Therefore, the requirement for the allowed overvoltage should be set before any attempt to decrease the switching losses is done.

An inverter with a pn freewheeling diode can have an average of up to 1.5 % improvement in NEDC efficiency by having a SiC freewheeling diode instead. The improvement is higher in urban drive cycles such as "Chalmers-Sahlgrenska" and "Artemis Urban" and is up to 2 %. At a low switching frequency of 5 kHz, a change of IGBT type from PT to NPT has the same effect as replacing the pn freewheeling diode to a SiC diode.

The use of SiC MOSFETs in the propulsion inverters instead of IGBTs can increase the efficiencies between two to five percent in NEDC. The efficiency improvement is maximized when it is compared to an IGBT-based inverter with pn diode in a more urban driving cycles and when the system voltage level is 800 V rather than 400 V. The least benefit is gained when it is used instead of IGBT-based inverters with a SiC diode at 400 V system in highway

driving cycles.

Increasing the dc-link voltage level from 400 V to 800 V, generally decreases the total conduction losses of the IGBT-based inverters. However, the switching loss of the components increase which leads to a lower drive cycle energy efficiency when the switching frequency of the inverter is chosen to be 7 kHz or higher.

Overdimensioning the components in the inverter in order to achieve a higher efficiency depends on the switching component. This might lead to an improvement of up to 4 % for a 100 % overdimentioned SiC MOSFET-based inverter at certain operating points, however, the drive cycle efficiency improvement is below 0.6 %.

By controlling the dc-link voltage of the inverter, which can be achieved by using an extra DC-DC converter in between the battery and the propulsion inverter, the switching loss and therefore the inverter losses can be decreased. For an IGBT-based inverter this can improve the drive cycle efficiency for the entire electric drive-train from the battery to the electric machine up to 4 %, however, the corresponding improvement is only 1 % for a SiC MOSFET-based inverter where the switching losses are relatively lower.

6.2 Future Work

The following items are a few examples for continuation of this work, either as a complementary solution or in addition to the issues raised in this thesis.

- A complementary Life Cycle Assessment for all efficiency evaluations provides a better picture of whether a solution can be commercialized.
- Since cooling is one of the major challenges of electric drives, study of the thermal consequence of different solutions is definitely of great interest. Any solution that improves the efficiency to a level where a cooling system can be simplified or eliminated, can be very valuable from system perspective.
- The proposed control strategy can be tested for other electric machine topologies and the usefulness of the method can be studied.
- The iron loss behaviour which is provided from FEA in this work can be verified by an actual measurement setup. Furthermore, the proposed control strategy can be tested for a real electric machine setup which is built based on the FEA design to quantify the accuracy of the FEA.
- Other wide band gap materials such as GaN can also be studied through the measurement setups and the consequences on the electric drive-line efficiency can be evaluated.
- Other propulsion inverter topologies such as multilevel inverters can also be studied.

Bibliography

[1] Y. Inoue, S. Morimoto, and M. Sanada, "A novel control scheme for maximum power operation of synchronous reluctance motors including maximum torque per flux control," *Industry Applications, IEEE Transactions on*, vol. 47, no. 1, pp. 115–121, 2011.

[2] F. Fernandez-Bernal, A. Garcia-Cerrada, and R. Faure, "Model-based loss minimization for dc and ac vector-controlled motors including core saturation," *Industry Applications, IEEE Transactions on*, vol. 36, no. 3, pp. 755–763, May 2000.

[3] C. Cavallaro, A. Di Tommaso, R. Miceli, A. Raciti, G. Galluzzo, and M. Trapanese, "Efficiency enhancement of permanent-magnet synchronous motor drives by online loss minimization approaches," *Industrial Electronics, IEEE Transactions on*, vol. 52, no. 4, pp. 1153–1160, 2005.

[4] F. Bernal, A. Garefa-Cerrada, and R. Faure, "Loss-minimization control of synchronous machines with constant excitation," in *Power Electronics Specialists Conference, 1998. PESC 98 Record. 29th Annual IEEE*, vol. 1, May 1998, pp. 132–138 vol.1.

[5] F. Fernandez-Bernal, A. Garcia-Cerrada, and R. Faure, "Model-based loss minimization for dc and ac vector-controlled motors including core saturation," *Industry Applications, IEEE Transactions on*, vol. 36, no. 3, pp. 755–763, 2000.

[6] A. Rabiei, T. Thiringer, and J. Lindberg, "Maximizing the energy efficiency of a pmsm for vehicular applications using an iron loss accounting optimization based on nonlinear programming," in *Electrical Machines (ICEM), 2012 XXth International Conference on*, 2012, pp. 1001–1007.

[7] B. Stumberger, G. Stumberger, D. Dolinar, A. Hamler, and M. Trlep, "Evaluation of saturation and cross-magnetization effects in inte-

rior permanent-magnet synchronous motor," *Industry Applications, IEEE Transactions on*, vol. 39, no. 5, pp. 1264–1271, Sept 2003.

[8] H. Kim, J. Hartwig, and R. Lorenz, "Using on-line parameter estimation to improve efficiency of ipm machine drives," in *Power Electronics Specialists Conference, 2002. pesc 02. 2002 IEEE 33rd Annual*, vol. 2, 2002, pp. 815–820 vol.2.

[9] S. Morimoto, M. Sanada, and Y. Takeda, "Effects and compensation of magnetic saturation in flux-weakening controlled permanent magnet synchronous motor drives," *Industry Applications, IEEE Transactions on*, vol. 30, no. 6, pp. 1632–, Nov 1994.

[10] A. Consoli, G. Scarcella, G. Scelba, and A. Testa, "Steady-state and transient operation of ipmsms under maximum-torque-per-ampere control," *Industry Applications, IEEE Transactions on*, vol. 46, no. 1, pp. 121–129, Jan 2010.

[11] R. Nalepa and T. Orlowska-Kowalska, "Optimum trajectory control of the current vector of a nonsalient-pole pmsm in the field-weakening region," *Industrial Electronics, IEEE Transactions on*, vol. 59, no. 7, pp. 2867–2876, July 2012.

[12] G. Rang, J. Lim, K. Nam, H.-B. Ihm, and H.-G. Kim, "A mtpa control scheme for an ipm synchronous motor considering magnet flux variation caused by temperature," in *Applied Power Electronics Conference and Exposition, 2004. APEC '04. Nineteenth Annual IEEE*, vol. 3, 2004, pp. 1617–1621 Vol.3.

[13] A. Consoli, G. Scarcella, G. Scelba, and S. Sindoni, "Modeling control of ipm synchronous motors," in *Power and Energy Society General Meeting - Conversion and Delivery of Electrical Energy in the 21st Century, 2008 IEEE*, July 2008, pp. 1–6.

[14] S.-Y. Jung, J. Hong, and K. Nam, "Current minimizing torque control of the ipmsm using ferrari's method," *Power Electronics, IEEE Transactions on*, vol. 28, no. 12, pp. 5603–5617, Dec 2013.

[15] I. Jeong, B.-G. Gu, J. Kim, K. Nam, and Y. Kim, "Inductance estimation of electrically excited synchronous motor via polynomial approximations by least square method," *Industry Applications, IEEE Transactions on*, vol. 51, no. 2, pp. 1526–1537, March 2015.

[16] F. Fernandez-Bernal, A. Garcia-Cerrada, and R. Faure, "Determination of parameters in interior permanent-magnet synchronous motors with iron losses without torque measurement," *Industry Applications, IEEE Transactions on*, vol. 37, no. 5, pp. 1265–1272, Sep 2001.

[17] J. Gallagher and D. Seals, "Design considerations for the power electronics of an electric vehicle propulsion inverter," in *WESCON/94. Idea/Microelectronics. Conference Record*, 1994, pp. 34–40.

[18] H. Zhang, L. Tolbert, and B. Ozpineci, "Impact of sic devices on hybrid electric and plug-in hybrid electric vehicles," *Industry Applications, IEEE Transactions on*, vol. 47, no. 2, pp. 912–921, 2011.

[19] B. Ozpineci, L. Tolbert, and S. Islam, "Silicon carbide power device characterization for hevs," in *Power Electronics in Transportation, 2002*, 2002, pp. 93–97.

[20] B. Ozpineci and L. Tolbert, "Characterization of sic schottky diodes at different temperatures," *Power Electronics Letters, IEEE*, vol. 1, no. 2, pp. 54–57, 2003.

[21] Y. Cui, M. Chinthavali, F. Xu, and L. Tolbert, "Characterization and modeling of silicon carbide power devices and paralleling operation," in *Industrial Electronics (ISIE), 2012 IEEE International Symposium on*, 2012, pp. 228–233.

[22] B. Ozpineci, L. Tolbert, S. Islam, and M. Hasanuzzaman, "Effects of silicon carbide (sic) power devices on hev pwm inverter losses," in *Industrial Electronics Society, 2001. IECON '01. The 27th Annual Conference of the IEEE*, vol. 2, 2001, pp. 1061–1066 vol.2.

[23] H. Zhang, L. Tolbert, B. Ozpineci, and M. Chinthavali, "Power losses and thermal modeling of a 4h-sic vjfet inverter," in *Industry Applications Conference, 2005. Fourtieth IAS Annual Meeting. Conference Record of the 2005*, vol. 4, 2005, pp. 2630–2634 Vol. 4.

[24] B. Ozpineci, M. Chinthavali, L. Tolbert, A. Kashyap, and H. Mantooth, "A 55 kw three-phase inverter with si igbts and sic schottky diodes," in *Applied Power Electronics Conference and Exposition, 2006. APEC '06. Twenty-First Annual IEEE*, 2006, pp. 7 pp.–.

[25] J. Liu, K. L. Wong, S. Allen, and J. Mookken, "Performance evaluations of hard-switching interleaved dc/dc boost converter with new generation silicon carbide mosfets," *Cree Inc, SiC App. Engineering*.

[26] N. Oswald, P. Anthony, N. McNeill, and B. Stark, "An experimental investigation of the tradeoff between switching losses and emi generation with hard-switched all-si, si-sic, and all-sic device combinations," *Power Electronics, IEEE Transactions on*, vol. 29, no. 5, pp. 2393–2407, May 2014.

[27] G. Wang, J. Mookken, J. Rice, and M. Schupbach, "Dynamic and static behavior of packaged silicon carbide mosfets in paralleled applications," in *Applied Power Electronics Conference and Exposition (APEC), 2014 Twenty-Ninth Annual IEEE*, March 2014, pp. 1478–1483.

[28] H. Li, S. Munk-Nielsen, X. Wang, R. Maheshwari, S. Beczkowski, C. Uhrenfeldt, and W. Franke, "Influences of device and circuit mismatches on paralleling silicon carbide mosfets," *Power Electronics, IEEE Transactions on*, vol. PP, no. 99, pp. 1–1, 2015.

[29] D.-P. Sadik, J. Colmenares, D. Peftitsis, J.-K. Lim, J. Rabkowski, and H.-P. Nee, "Experimental investigations of static and transient current sharing of parallel-connected silicon carbide mosfets," in *Power Electronics and Applications (EPE), 2013 15th European Conference on*, Sept 2013, pp. 1–10.

[30] Y. Cui, M. Chinthavali, F. Xu, and L. Tolbert, "Characterization and modeling of silicon carbide power devices and paralleling operation," in *Industrial Electronics (ISIE), 2012 IEEE International Symposium on*, May 2012, pp. 228–233.

[31] M. Rahimo, F. Canales, R. Minamisawa, C. Papadopoulos, U. Vemulapati, A. Mihaila, S. Kicin, and U. Drofenik, "Characterization of a silicon igbt and silicon carbide mosfet cross-switch hybrid," *Power Electronics, IEEE Transactions on*, vol. 30, no. 9, pp. 4638–4642, Sept 2015.

[32] H. Zhang and L. Tolbert, "Efficiency of sic jfet-based inverters," in *Industrial Electronics and Applications, 2009. ICIEA 2009. 4th IEEE Conference on*, 2009, pp. 2056–2059.

[33] O. Hegazy, R. Barrero, J. Van Mierlo, P. Lataire, N. Omar, and T. Coosemans, "An advanced power electronics interface for electric vehicles ap-

plications," *Power Electronics, IEEE Transactions on*, vol. 28, no. 12, pp. 5508–5521, 2013.

[34] K. Acharya, S. Mazumder, and P. Jedraszczak, "Efficient, high-temperature bidirectional dc/dc converter for plug-in-hybrid electric vehicle (phev) using sic devices," in *Applied Power Electronics Conference and Exposition, 2009. APEC 2009. Twenty-Fourth Annual IEEE*, 2009, pp. 642–648.

[35] O. Hegazy, J. Van Mierlo, and P. Lataire, "Analysis, modeling, and implementation of a multidevice interleaved dc/dc converter for fuel cell hybrid electric vehicles," *Power Electronics, IEEE Transactions on*, vol. 27, no. 11, pp. 4445–4458, 2012.

[36] M. Pahlevaninezhad, P. Das, J. Drobnik, P. Jain, and A. Bakhshai, "A novel zvzcs full-bridge dc/dc converter used for electric vehicles," *Power Electronics, IEEE Transactions on*, vol. 27, no. 6, pp. 2752–2769, 2012.

[37] R. H. Staunton, C. W. Ayers, L. D. Marlino, J. N. Chiasson, and T. A. Burress, "Evaluation of 2004 toyota prius hybrid electric drive system," Oak Ridge, TN, ORNL, Tech. Rep. TM-2006/423, May 2006.

[38] J. S. Hsu, , C. W. Ayers, and C. L. Coomer, "Report on toyota/prius motor design and manufacturing assessment," Oak Ridge, TN, ORNL, Tech. Rep. TM-2004/137, August 2004.

[39] L. Harnefors and H.-P. Nee, "Control of variable-speed drives," *Course compendium, Malardalen University, Sweden*, 2002.

[40] P. Pillay and R. Krishnan, "Modeling of permanent magnet motor drives," *Industrial Electronics, IEEE Transactions on*, vol. 35, no. 4, pp. 537–541, Nov 1988.

[41] T.-C. Jeong, W.-H. Kim, M.-J. Kim, K.-D. Lee, J.-J. Lee, J.-H. Han, T.-H. Sung, H.-J. Kim, and J. Lee, "Current harmonics loss analysis of 150-kw traction interior permanent magnet synchronous motor through co-analysis of d-q axis current control and finite element method," *Magnetics, IEEE Transactions on*, vol. 49, no. 5, pp. 2343–2346, May 2013.

[42] F. Deng, "An improved iron loss estimation for permanent magnet brushless machines," *Energy Conversion, IEEE Transactions on*, vol. 14, no. 4, pp. 1391–1395, 1999.

[43] S. Morimoto, Y. Tong, Y. Takeda, and T. Hirasa, "Loss minimization control of permanent magnet synchronous motor drives," *Industrial Electronics, IEEE Transactions on*, vol. 41, no. 5, pp. 511–517, Oct 1994.

[44] C. Cavallaro, A. Di Tommaso, R. Miceli, A. Raciti, G. Galluzzo, and M. Trapanese, "Efficiency enhancement of permanent-magnet synchronous motor drives by online loss minimization approaches," *Industrial Electronics, IEEE Transactions on*, vol. 52, no. 4, pp. 1153–1160, Aug 2005.

[45] L. Mestha and P. Evans, "Analysis of on-state losses in pwm inverters," *Electric Power Applications, IEE Proceedings B*, vol. 136, no. 4, pp. 189–195, 1989.

[46] *Datasheet MOSFET SCT2080KE*, Rohm Semiconductor, 2014.01 Rev. D.

[47] J. Jose, G. Goyal, and M. Aware, "Improved inverter utilisation using third harmonic injection," in *Power Electronics, Drives and Energy Systems (PEDES) 2010 Power India, 2010 Joint International Conference on*, Dec 2010, pp. 1–6.

[48] J. Kolar, H. Ertl, and F. C. Zach, "Influence of the modulation method on the conduction and switching losses of a pwm converter system," in *Industry Applications Society Annual Meeting, 1990., Conference Record of the 1990 IEEE*, Oct 1990, pp. 502–512 vol.1.

[49] D. Holmes, "The significance of zero space vector placement for carrier-based pwm schemes," *Industry Applications, IEEE Transactions on*, vol. 32, no. 5, pp. 1122–1129, Sep 1996.

[50] N. Mohan, T. M. Undeland, and W. P. Robbins, *Power Electronics: Converters, Applications, and Design, 3rd Edition.* John Wiley & Sons, 2002.

[51] Z. Zhang, W. Eberle, Z. Yang, Y.-F. Liu, and P. Sen, "Optimal design of resonant gate driver for buck converter based on a new analytical loss model," *Power Electronics, IEEE Transactions on*, vol. 23, no. 2, pp. 653–666, 2008.

[52] *Datasheet MOSFET CMF20120*, Cree, Inc., 2012 Rev. D.

[53] *Datasheet Diode C4D30120D*, Cree, Inc., 2012 Rev. C.

[54] T. Sebastiangordon and G. Slemon, "Operating limits of inverter-driven permanent magnet motor drives," *Industry Applications, IEEE Transactions on*, vol. IA-23, no. 2, pp. 327–333, March 1987.

[55] S.-Y. Jung, J. Hong, and K. Nam, "Current minimizing torque control of the ipmsm using ferrari 2019's method," *Power Electronics, IEEE Transactions on*, vol. 28, no. 12, pp. 5603–5617, Dec 2013.

[56] M. Andre, "The artemis european driving cycles for measuring car pollutant emissions," *Science of The Total Environment*, vol. 334335, pp. 73 – 84, 2004, highway and Urban Pollution. [Online]. Available: http://www.sciencedirect.com/science/article/pii/S0048969704003584

[57] L. Guzzella and A. Sciarretta, *Vehicle Propulsion Systems*, 3rd ed. Springer Berlin Heidelberg, 2013.

[58] *Datasheet IGBT IXYK100N65C3D1*, IXYS, 2014.

[59] *Datasheet IGBT IXYN100N65A3*, IXYS, 2014.

[60] *Datasheet Diode IXYX100N65C3D1*, IXYS, 2014.

[61] *Datasheet MOSFET SCT2120AF*, Rohm Semiconductor, 2014.01 Rev. B.

[62] *Datasheet Diode C5D50065D*, Cree, Inc., 2012 Rev. -.

[63] *Datasheet IGBT IXGK82N120A3*, IXYS, 2009.

[64] *Datasheet IGBT IXYH82N120C3*, IXYS, 2012.

[65] *Datasheet Diode DHG60I1200HA*, IXYS, 2011.